

**DOKUZ EYLÜL UNIVERSITY
GRADUATE SCHOOL OF NATURAL AND APPLIED
SCIENCES**

**DETERMINATION OF THE MECHANICAL
PROPERTIES AND FATIGUE CRACK
PROPAGATION OF THE LASER WELDED NEW
GENERATION ALUMINUM ALLOYS**

**by
Murat PAKDİL**

**September, 2005
İZMİR**

**DETERMINATION OF THE MECHANICAL
PROPERTIES AND FATIGUE CRACK
PROPAGATION OF THE LASER WELDED NEW
GENERATION ALUMINUM ALLOYS**

**A Thesis Submitted to the
Graduate School of Natural and Applied Sciences of Dokuz Eylül University
In Partial Fulfilment of the Requirements for the Degree of Doctor of Philosophy in
Mechanical Engineering, Mechanics Program**

**by
Murat PAKDİL**

**September, 2005
İZMİR**

Ph.D. THESIS EXAMINATION RESULT FORM

We have read the thesis entitled “**DETERMINATION OF THE MECHANICAL PROPERTIES AND FATIGUE CRACK PROPAGATION OF THE LASER WELDED NEW GENERATION ALUMINUM ALLOYS**” completed by **Murat PAKDİL** under supervisions of **Prof. Dr. Seçil ERİM** and **Prof. Dr. Gürel ÇAM** we certify that in our opinion it is fully adequate, in scope and in quality, as a thesis for the degree of Doctor of Philosophy.

Prof. Dr. Seçil ERİM
Supervisor

Prof. Dr. Onur SAYMAN
Committee Member

Assist. Prof. Dr. Mustafa TOPARLI
Committee Member

.....
Jury Member

.....
Jury Member

Prof.Dr. Cahit HELVACI
Director
Graduate School of Natural and Applied Sciences

ACKNOWLEDGMENTS

I would like to express my thanks towards my supervisors, Prof. Dr. Seil ERİM and Prof. Dr. Gürel AM, whose guidance and encouragement helped me greatly throughout my research and writing. My thanks go out to my research committee members, Dr. Mustafa TOPARLI and Prof. Dr .Onur SAYMAN for their valuable discussion on my research.

I would especially like to thank Dr. Mustafa KOAK and also Dr. Vaidya, Mr. Horstmann and Mr. Tek for their valuable comments and help on my experimental studies during this dissertation and other GKSS Research Center staff. My special thanks go to Dr. Emine ınar YENİ devoting her time, support and guidance in helping me complete this thesis document.

I am also grateful to my family who has supported me throughout my education. My sincere thanks are for my wife, Nazlı PAKDİL, for her encouragement and support in every step of our life together.

Murat PAKDİL-İzmir, 2005

**DETERMINATION OF THE MECHANICAL PROPERTIES AND FATIGUE
CRACK PROPAGATION OF THE LASER WELDED NEW GENERATION
ALUMINUM ALLOYS**

ABSTRACT

Aluminum alloys have become the materials of choice in many industrial applications such as aircraft structures due to their many favorable properties like high strength to weight ratio, ease of forming and high thermal and electrical conductivity. Recent advances in high powered laser beam technology have made it possible to consider welded airframe primary structures in commercial aircrafts. Therefore, laser beam welding is considered as a suitable joining process for high speed, low distortion, high quality fabrication of aircraft structures manufactured from aluminum alloys.

Although the potential of laser beam welding as an appropriate joining method for aluminum alloys is recognized, 6xxx series aluminum alloys may exhibit a tendency to solidification cracking, and porosity may be a major problem unless appropriate welding parameters and filler metal addition are employed.

In this study, CO₂ laser beam welded new generation aluminum alloys, developed especially for aircraft structures are examined in detail in terms of their mechanical properties and fatigue crack propagation. In the first part of the thesis, basic knowledge and existing literature on high powered beam welding, fatigue, aluminum alloys and their welded applications are summarized. Based on this information, room temperature mechanical properties of a new generation 6xxx series aluminum alloy, joined with a CO₂ laser using AlSi12 filler wire were determined experimentally and discussed in the second part of the thesis. Macro- and micro-tensile specimens were used for the determination of general and local mechanical properties of the welded joints. Extensive hardness measurements were conducted. The weld region was examined in detail by Scanning Electron Microscope (SEM) and optical microscope. Fatigue crack propagation tests in various stress ratios ($0.1 \leq R \leq 0.7$) were carried out to determine the crack

propagation mechanisms under dynamic loading. The effects of mechanical property variation and microstructural variations on the fatigue crack propagation in laser beam welded joints have been investigated. The relation between stress ratio and porosity size, as well as the effects of grain boundary liquation on crack propagation have been established.

It has been concluded that, in light of the existing research, laser beam welding is a suitable joining process for high speed, low distortion and high quality fabrication of lightweight airframe structures made from aluminum alloys provided that appropriate welding parameters and alloy composition are employed.

Keywords : Aluminum alloys, Fatigue, Laser Beam Welding, FCP

**LAZER KAYNAKLI YENİ NESİL ALÜMİNYUM ALAŞIMLARININ
MEKANİK ÖZELLİKLERİNİN VE YORULMA
MEKANİZMALARININ BELİRLENMESİ**

ÖZ

Alüminyum alaşımları, yüksek mukavemet/ağırlık oranı sağlaması, kolay şekil alabilmesi ve yüksek termal ve elektrik iletkenliği gibi özelliklerinden dolayı uçak endüstrisi dahil birçok endüstriyel uygulamalarda yaygın bir kullanım alanı bulmaktadır. Yüksek kapasiteli lazer teknolojisindeki son gelişmeler, ticari hava taşıtlarında kaynaklı bağlantıların kullanılmasını olanaklı hale getirmiştir. Bundan dolayı lazer kaynağı, alüminyum alaşımlarından imal edilmiş olan hava taşıtları parçalarının yüksek hızda az miktarda deformasyon ve yüksek kaliteli üretimi için uygun bir birleştirme yöntemi olarak kabul edilmektedir.

Lazer kaynağı, alüminyum alaşımları için uygun bir birleştirme yöntemi olarak tanınmasına rağmen, uygun kaynaklama parametreleri kullanılmaz ve doğru dolgu metali ilavesi yapılmazsa 6xxx serisi alüminyum alaşımları katılaşma kırılması eğilimi gösterebilir ve bu tür kaynaklarda porozite büyük bir problem yaratabilir.

Bu çalışmada CO₂ lazer kaynağı ile kaynaklanmış yeni nesil alüminyum alaşımları (özellikle hava taşıtları için) mekanik özellikleri ve yorulma çatlak ilerlemeleri açısından detaylı şekilde incelenmiştir. Tezin ilk kısmında yüksek kapasiteli lazer teknolojisi, yorulma, alüminyum alaşımları ve onların kaynaklı uygulamaları üzerine mevcut literatür ve temel bilgiler özetlenmiştir. Bu bilgilere dayanarak, tezin ikinci kısmında, AlSi12 dolgu teli ile CO₂ lazer kaynağı kullanılarak kaynaklanmış yeni nesil 6xxx serisi alüminyum alaşımlarının oda sıcaklığı mekanik özelliklerinin tespitine yönelik gerçekleştirilen deney sonuçları tartışılmıştır. Makro ve mikro-çekme örnekleri, kaynaklanmış parçaların genel ve lokal mekanik özelliklerinin belirlenmesi için kullanılmıştır. Kapsamlı sertlik ölçümleri yapılmıştır. Kaynak bölgesi detaylı olarak SEM (Taramalı Elektron Mikroskobu) ve optik mikroskop altında incelenmiştir.

Dinamik ykleme altında atlak ilerlemesi mekanizmalarını belirleyebilmek zere eřitli gerilme oranlarında ($0.1 \leq R \leq 0.7$) yorulma atlak ilerlemesi testleri yapılmıřtır. Lazer kaynađı yapılmıř paralarda yorulma atlađı ilerlemesi zerinde mikro yapısal deđiřimlerin ve mekanik deđiřimin etkileri arařtırılmıřtır. Stres oranı ve porozite boyutu arasındaki iliřkiye ilave olarak atlak ilerlemesi zerinde tane sınırı sınıvılařmasının etkileri de incelenmiřtir.

Sonuç olarak mevcut arařtırmaların ıřıđında, lazer kaynađının uygun kaynaklama parametreleri ve alařım kompozisyonu kullanıldıđında, alminyum alařımlarından retilmiř dřk ađırlıktaki uak paralarının birleřtirilmesi iin uygun bir kaynak yntemi olduđu grlmektedir.

Anahtar szckler : Alminyum Alařımları, Yorulma, Lazer Kaynađı, FCP

CONTENTS

	Page
THESIS EXAMINATION RESULT FORM	<i>ii</i>
ACKNOWLEDGEMENTS.....	<i>iii</i>
ABSTRACT.....	<i>iv</i>
ÖZ.....	<i>vi</i>
CHAPTER ONE – INTRODUCTION.....	1
CHAPTER TWO – BACKGROUND.....	7
2.1 Power Beam Welding Processes.....	7
2.1.1 Electron Beam Welding	7
2.1.2 Laser Beam Welding	10
2.1.2.1 Carbon Dioxide Laser Welding	13
2.1.2.1.1 Sealed Tube CO ₂ Lasers.....	13
2.1.2.1.2 Wave-guide CO ₂ Lasers.....	14
2.1.2.1.3 TEA CO ₂ Lasers.....	15
2.1.2.2 Carbon Monoxide Laser Welding.....	16
2.1.2.3 Nd:YAG Laser Welding.....	17
2.1.2.4 Comparison of Laser Welding Methods.....	19
2.1.2.5 New Trends in Laser Welding	21
2.1.2.6 Advantages of Laser Welding	28
2.2 Aluminum Alloys and the Welding of Aluminum Alloys.....	30
2.2.1 Aluminum Alloys.....	30
2.2.1.1 Characteristics of Aluminum Alloys.....	36
2.2.2 The Welding of Aluminum Alloys.....	39
2.2.2.1 Why Joining Al-Alloys	39
2.2.2.2 Difficulties in Welding of Aluminum Alloys	42

2.2.2.2.1 Weld Cracking.....	42
2.2.2.2.2 Weld Porosity.....	43
2.2.2.2.3 Loss of Strength.....	45
2.2.2.3 Laser Welding Issues with Aluminum Alloys.....	47
2.3 Fatigue	51
2.3.1 The Three Modes of Loading	58
2.3.3 Micro Mechanisms of Fatigue.....	59
2.3.4 Crack Tip Plastic Zone Size.....	63
2.3.5 Fatigue Design Criteria	68
2.3.5.1 Infinite- Life Design	68
2.3.5.2 Safe-Life Design.....	68
2.3.5.3 Fail Safe Design	69
2.3.5.4 Damage Tolerant Design.....	69
2.3.5.5 Life Prediction for Crack Propagation.....	70
CHAPTER THREE - EXPERIMENTAL PROCEDURE.....	77
3.1 Material	77
3.2 Microstructure.....	79
3.3 Microhardness	80
3.4 Tensile Tests	80
3.4.1 Microtensile Test	80
3.4.2 Transverse Tensile Test	82
3.5 Fatigue Crack Propagation (FCP) Test	83
3.5.1 Measurement of Fatigue Crack Propagation	88
CHAPTER FOUR - RESULTS AND DISCUSSION.....	90
4.1 Microstructural Aspects and Weld Quality	90
4.2 Microhardness Profile	95
4.3 Tensile Test.....	102
4.4 FCP Results.....	104

CHAPTER FIVE - CONCLUSIONS AND RECOMMENDATIONS 130

REFERENCES..... 132

CHAPTER ONE

INTRODUCTION

In recent years, application areas of aluminum alloys have experienced a great increase, this in turn stimulated intensive research activities on new generation aluminum alloys. Aluminum possessing high strength, low weight and resistance to corrosion, offers several advantages compared to other commercial materials including steels.

Parallel to the increase on research on the weldability aspects of aluminum alloys, applications of welded aluminum structures are also increasing. In cases where it is not possible to manufacture an integral component by other production methods, one alternative solution can be the weldability of that material, provided that the welding process is feasible and economically acceptable by the manufacturer. Therefore, weldability is an important factor for wide-spread application of a material.

Aluminum alloys are widely joined by laser beam welding providing a narrow HAZ or friction stir welding without the need to melt the material. Friction stir welding, being a solid state joining technique, offers the advantage of less strength decrease in the weld area compared to fusion welds, however, has the disadvantages of slow welding speed, difficulty in applying to various configurations (e.g. T-joints) and applicability to limited thickness (Vaidya, Kocak, Seib, Assler & Hackius,2004).

Laser beam welding of specified aluminum alloys has been approved for a number of applications. These are mainly in the automotive, aerospace, construction, and electronics industries. Selected examples are described below. There is a considerable potential for growth in other industry sectors, notably shipbuilding, packaging, and domestic appliances (Ion, 2000).

Automotive: Legislation concerning reduced emissions, among other factors, has compelled the automotive industry to examine the use of lighter materials and new manufacturing designs to reduce fuel consumption. The Audi A8 car is built around an

aluminum space-frame, but is currently welded using the MIG process. However, the aluminum panels and extrusions in the Audi A2 compact car are welded using Nd-YAG laser beams. Welding of aluminum bonnets for the Volvo 960 using Nd-YAG laser beams has also been investigated (Ion, 2000).

Construction: An early industrial application involved laser beam welding of the longitudinal seam of roll formed window spacers used to separate the panes of double glazing units. Welds were made using an incident beam power of 1 kW at speeds up to 100 m/min. Laser beam welding increased the stiffness of the spacer, enabling the material thickness to be reduced substantially (Ion, 2000).

Electronics: Packages have been produced with laser beam welds between 4000 series lids and 6000 series machined boxes for microwave and radar applications. There is potential for considerable use of laser beam welding in such fields (Ion, 2000).

Moreover, the potential for reduced manufacturing costs, increased payloads, and reduced fuel consumption is the main reason for the interest of the aerospace industry in laser beam welding of aluminum alloys. Laser beam welding is being considered as an alternative to mechanical fastening and adhesive bonding in certain applications. As well as improvements in product quality and properties, cost and weight savings can be achieved through a simplification of the existing manufacturing process and the elimination of additional joining elements such as rivets and sealants.

The recent commercial availability of high powered lasers has made it possible to consider welding as a practical alternative to riveting in the assembly of commercial aircraft structures. In compression dominated areas, such as the lower fuselage, the welded structure may be on the order of 10% lighter due to the more efficient use of stringer material, the favorable yield strength of candidate weldable alloys and the reduction of the amount of sealant and the number of fasteners. The inherent corrosion resistance of these weldable alloys and the elimination of moisture traps between faying surfaces will result in reduced maintenance and repair costs. Laser welded joints are produced at rates up to 10 m/min, on the order of 100 times

faster than automatic riveting machines. This will result in significant reductions in manufacturing costs (Lenczowski, 2002).

The 6000 series aluminum alloys exhibit a tendency to solidification cracking unless the weld metal composition includes appropriate filler metal additions. Intergranular cracking in partially melted base metal adjacent to the weld fusion boundary (liquation cracking) is also a known problem in 6000 series arc welds (Leigh, Poon & Ferguson, 2002).

The peak temperature in the heat affected zone (HAZ) will cause varying amounts of grain coarsening and solution of the precipitates responsible for strengthening 6000 series alloys. Moreover, local as-welded microstructural features can be expected that may reduce intergranular corrosion resistance. However, it is believed that a partial recovery of weldment strength and corrosion resistance can be achieved by welding in the naturally aged condition, followed by an artificial aging heat treatment of the welded assembly.

Excessive porosity in aluminum welds can result unless effective measures are taken prior to and during welding to keep sources of hydrogen, such as moisture or organic compounds, away from the weld zone (Leigh et al., 2002).

As mentioned above, new generation aluminum alloys have been developed to avoid these problems. The Al-Mg-Si-Cu alloys 6013 (Alcoa) and 6056 (Pechiney) have been selected for investigation because of their strength, formability and weldability. These alloys are used in some applications by EADS (Airbus) and have been successfully used by Bombardier Aerospace in other structural applications (Vaidya et al., 2004).

The success of laser beam welding when applied to aluminum alloys is strongly dependent on alloy composition, material preparation techniques and processing parameters. In comparison with steels, the development of welding procedures is more challenging, but welds have been produced in most alloy series that meet the

most stringent requirements of current workmanship standards. The process has recently been approved for use in non-critical joints in the aerospace and automotive industries, using both CO₂ and Nd-YAG laser beams, and has been used for some time in other industries such as construction and electronics. The large amount of work currently being undertaken to develop new, weldable, damage tolerant aluminum alloys is an indication of the current interest and potential (Rhenalu, 2001).

The main imperfections observed are porosity, solidification cracking, a poor weld bead geometry, and susceptibility to stress corrosion cracking in certain alloys. Porosity can be minimised by eliminating sources of hydrogen, through chemical cleaning of the workpiece, and via the use of appropriate process gases. Mixtures of helium and argon have been found to give good penetration, while maintaining a smooth weld bead profile. Solidification cracking can be eliminated using an appropriate filler wire. Guidance is available from existing standards related to arc fusion welding processes. The filler material is selected to minimise the solidification temperature interval, Al-Cu and Al-Si wires being popular choices for 2000 and 6000 series alloys, respectively. Over-alloyed filler wires can also be used to compensate for the loss of alloying additions through vaporisation, a frequently encountered problem when welding 5000 series alloys. The weld bead geometry can be improved through the use of filler material and the appropriate selection of process gas parameters. The deterioration in mechanical and corrosion properties caused by welding can be counteracted in many alloys through post-weld heat treatment when possible, although the properties of certain alloys, notably 7020, can be improved by natural aging (Ion, 2000).

Currently, the majority of the sheets used for fuselage skin applications in civil aircrafts are made of standard AA2024 (or AA2090) aluminum alloy (See figure 1.1). This alloy displays very good mechanical characteristics (static tensile properties, toughness, etc.) in the stretched and naturally-aged temper condition (i.e. T351) (Dif, 2002a).

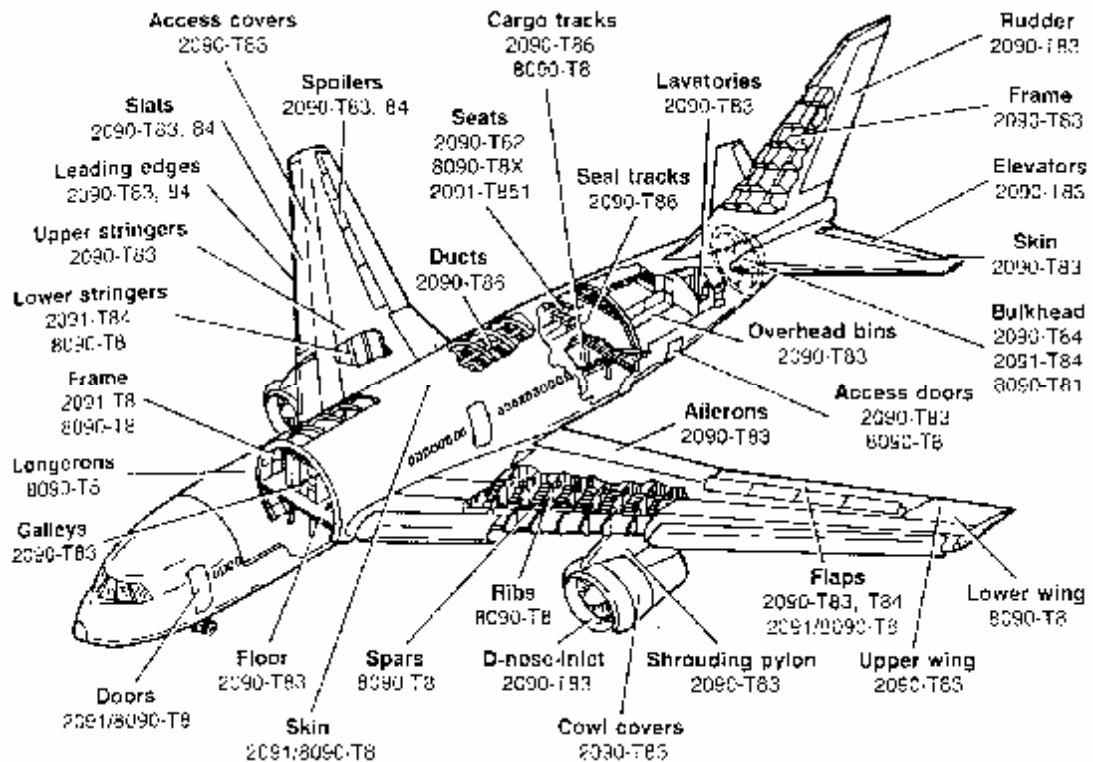


Figure 1.1 Use of Aluminum alloys in aerospace applications (Anonymous, 2004)

However, the use of the 2024 alloy has two drawbacks. Firstly, bare 2024 can be sensitive to intergranular corrosion (IGC) in the T351 temper as a function of quench rate (product thickness). For this reason, alloy 2024 is mostly used in the form of clad sheet. The cladding is usually made of 1050 which is resistant to corrosion and anodic corrosion to 2024. However, the cathodic protection of 2024 by the cladding is only effective on the outer side of the panels since the inner side is machined in typical fuselage applications. The cladding also entails a loss of static tensile properties (5 to 10%) and may foster crevice corrosion when two clad sheets are joined together. Secondly, 2024 cannot be welded. This might be a drawback if the airframe industry in the future wishes to promote the use of welded fuselage structures made of this alloy for cost and mass-saving reasons (Dif, 2002a).

Alloy 6056 in the T4 temper has been proved to exhibit outstanding stretch forming characteristics, thus offering a cost-efficient alternative for parts normally requiring one or more heat treating/stretching sequences. Thanks to its lower density, alloy 6056 offers also a 2,5% weight advantage over 2024 alloy (Rhenalu, 2001).

Alloy 6056 is available in the form of bare or clad sheet and thin plate, in the thickness range 0,8 to 12 mm (0,03 to 0,5 in). It is also available in the form of thin extrusions (Rhenalu, 2001).

Answering the demand of the aerospace industry for a weldable fuselage skin alloy with equivalent static and dynamic properties, but with an improved resistance to intergranular corrosion, Pechiney Rhenalu proposed the AA6056 alloy. A new IGC-resistant temper for 6056 has been proposed (Dif, 2002b).

In this study, mechanical and microstructural properties and fatigue crack propagation behavior of laser beam welded new generation aluminum alloy 6056 were examined and analysed in detail. Grain boundary liquation and porosity were determined in the weld regions of new generation aluminum alloys which were laser beam welded using AlSi12 weld wire. The effects of these common problems (grain boundary liquation and porosity) on fatigue crack propagation were investigated. Moreover, the relationship between R (stress ratio) and porosity has been determined.

CHAPTER TWO

BACKGROUND

2.1 Power Beam Welding Processes

Laser welding and electron beam welding are ‘power beam’ processes, which work in a fundamentally different way to most arc fusion processes. These processes have been explained below.

2.1.1 Electron Beam Welding

Electron Beam Welding (EBW) is a fusion process for joining metals which uses a highly focused beam of electrons as a heat source. Usually, the electrons are extracted from a hot cathode, accelerated by a high potential - typically 30.000-200.000 volts, and magnetically focused into a spot with a power density of the order of 30.000 W/mm². This causes almost instantaneous local melting and vaporization of the workpiece material (Anonymous, 2000). Figure 2.1 illustrates the main elements of the electron beam welding head. Currently, three distinct modes of EBW are employed:

High-vacuum (EBW-HV), where the workpiece is in an ambient pressure ranging from 0,13 to 0,30 MPa

Medium-vacuum (EBW-MV), where the workpiece may be in a “soft” or “partial” vacuum ranging from 0,13 to 3300 Pa

No vacuum (EBW-NV), which is also referred to as atmospheric EBW, where the workpiece is at pressure in air or protective gas. In all EBW applications, the electron-beam gun regions is maintained at a pressure of 13 MPa or lower (Olson, Siewert, Liu, & Edwards, 1993).

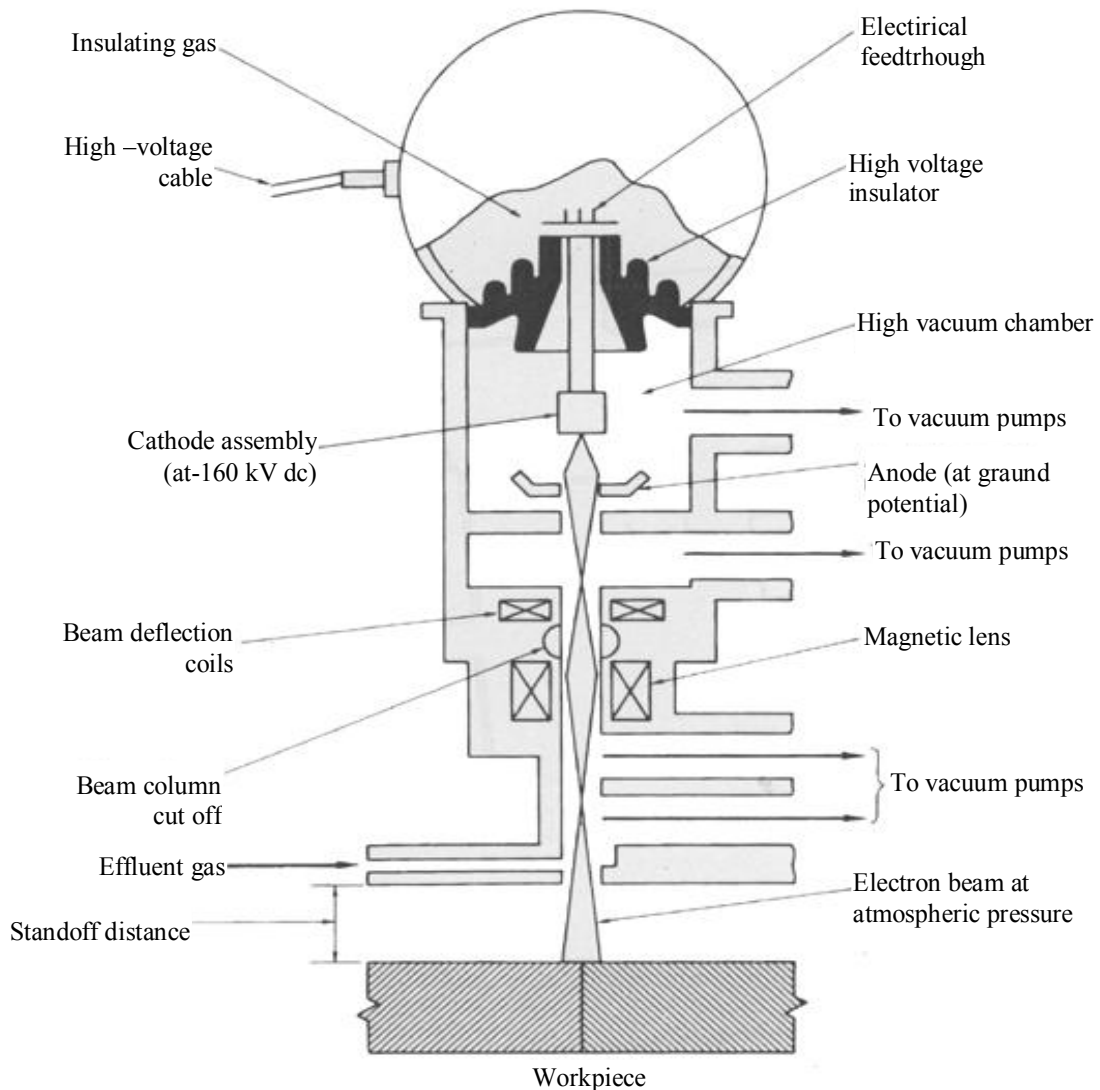


Figure 2.1 Schematic showing primary components of an electron-beam welding head (Olson, 1993)

The electron beam is thus able to establish a 'keyhole', delivering heat deep into the material being welded. This produces a characteristically narrow, near parallel, fusion zone allowing plain abutting edges to be welded in a single pass for material thicknesses ranging from less than 0,1 mm to greater than 200 mm (Anonymous, 2000). For example: A beam power of around 70 kW and welding speed of 200 mm/min gave a wide (8 mm) round-bottomed weld profile, Figure 2.2, ideal for avoiding root defects (Nightingale, 2004).

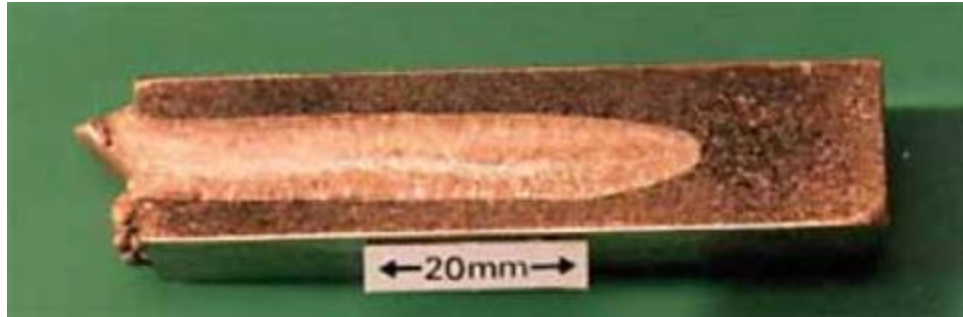


Figure 2.2 Reduced pressure EBW in copper showing round-bottomed weld profile (Nightingale, 2004)

Electron beams for welding are normally generated in a relatively high vacuum (about 5×10^{-5} mbar) but the workpiece can be housed in a chamber maintained at a coarser vacuum level, e.g. 5×10^{-3} to 10 mbar. It is also possible to project high power electron beams into the atmosphere and produce (single pass) welds in steel in thicknesses of more than 40 mm, Figure 2.3, but the weld width is typically greater than welds made in vacuum (Nightingale, 2004).

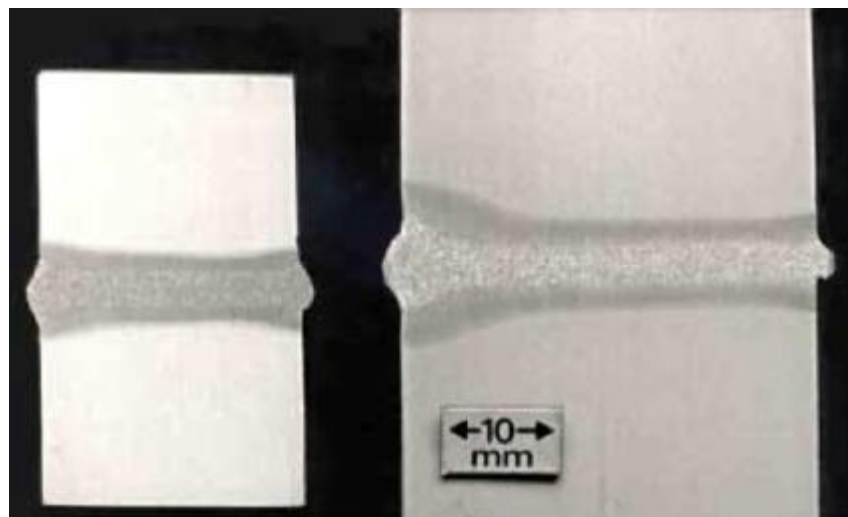


Figure 2.3 Transverse weld sections with 25 mm thickness (left) and 41 mm thickness (right) carbon manganese steel pipe (Nightingale, 2004)

Currently, reduced pressure EBW is in the process of being adopted for two major applications; namely, nuclear waste encapsulation and J-lay pipe girth weld. J-lay system which is constituted by Saipem SpA.-Italy is pipe line project which can be used in 2000 m or more depth in water (Nightingale, 2004).

2.1.2 Laser Beam Welding

Laser Beam Welding (LBW) uses a moving high-density (10^5 to 10^7 W/cm²) coherent optical energy source called laser as the source of heat. “Laser” is an acronym for “light amplification by stimulated emission of radiation”. The coherent nature of the laser beam allows it to be focused to a small spot, leading to high energy densities (Olson et al., 1993).

The laser beam was invented in 1960 and since then has come to be utilized successfully in optical communications, laser processing, and optical discs. The range of its applications has been greatly expanded, particularly in the past decades. The range of laser applications covers a multitude of fields including material processing, surface reformation and the creation of new materials. They are also used for chemical reaction control, biotechnology, medical treatment, measurement, analysis, data processing, information transmission, welding and much more. It is expected that the laser will bring about new technological developments in many fields (Fakatsu, 1997).

Lasers have been promoted as potentially useful welding tools for a variety of applications. Until 1970s, however, the laser welding had been restricted to relatively thin materials and low speeds because of limited continuous power available. By 1965, a variety of laser systems had been developed for making micro welds in electronic circuit boards, in side vacuum tubes, and in other specialized applications where conventional technology was unable to provide reliable joining (Olson et al., 1993).

Table 2.1 Energy consumption and efficiency of LBW relative to other selected welding process (Olson et al., 1993)

Welding process	Intensity of energy source (W/cm²)	Joining efficiency (mm²/kJ)	Fusion zone profile
Oxyacetylene (OAW)	10 ² -10 ³	0,2-0,5	Shallow for single pass
Arc welding	5x10 ² -10 ⁴	0,8-2(a) 2-3(b) 4-10(c)	Shallow for single pass
Plasma arc (PAW)	10 ³ -10 ⁶	5-10	Shallow at low-energy end Deep penetration at high-energy end
Laser beam	10 ⁵ -10 ⁷	15-25	Shallow at low-energy density range Deep penetration at high-energy density range
Electron beam	10 ⁵ -10 ⁸	20-30	Deep penetration

(a) Gas-tungsten arc welding (GTAW),

(b) Gas-metal arc welding (GMAW),

(c) Submerged arc welding (SAW).

The ability of the laser to generate a power density greater than 10⁶ W/cm² is a primary factor in establishing its potential for welding (Table 2.1). Numerous experiments have shown that the laser permits precision (that is, high quality) weld joints rivaled only by those made with an electron beam (Olson et al., 1993).

Laser beam welding is easier than electron beam welding, because it does not need a vacuum chamber. This process also has potential for full automation and precise process control due to greater optical flexibility and ease of beam delivery.

There are laser oscillators ranging from the long wave infrared to the short wave ultraviolet zone. There are several different laser oscillators available, namely CO₂ laser, CO laser, Iodine laser, YAG laser oscillators, etc. These laser oscillators are commonly used in the present day.

The CO₂ laser oscillator has a 5,5 kW power rating. Its computerized numerical control processing machine is capable of processing various kinds of materials. It is used especially in welding and surface treatment, developments of new applications are expected in these fields.

The CO laser oscillator has a 5 kW power rating, with emission at 5 μm wavelength. The computerized numerical control processing machine that is connected to the laser oscillator is capable of cutting thick materials effectively, because of its highly concentrated beam and the high absorption of metals at this wavelength.

The iodine laser oscillator has a 1 kW of power, emitting at 1,3 μm wavelength. Iodine laser beams are of high quality and are useful in high level processing.

The YAG laser oscillator emits 400 W of power at 1 μm wavelength. The beam is transmitted to a computerized numerical control processing machine which enables microprocessing to be performed. A wider scope of functions can be realized with the Q-Switch device that is connected. A synchronized twin excimer Laser pumps a dye laser system. This is capable of emitting any wavelength between 200 and 970 μm using various dye sources. This is superb in roles such as photochemical composition and ultra-microprocessing. A YAG laser pumped dye laser system is capable of emitting any beam between about 200 and 900 μm and is suited to high sensitivity analysts. A ring dye and ring titanium sapphire laser system is pumped by an argon ion laser. This system is capable of emitting radiation covering a wide range of wavelengths, thus enabling to use the system in spectral analysis and laser applied measurement. The Laser is a pioneering tool in the development of future technology (Fakatsu, 1997).

Three main types of laser beam welding are commonly used. These are Carbon Monoxide Laser Welding, Carbon Dioxide Laser Welding, and Nd:YAG Laser Welding.

2.1.2.1 Carbon Dioxide Laser Welding

The carbon dioxide (CO₂) gas laser, is one of the most versatile for materials processing applications, and emits infra red radiation with a wavelength between 9 and 11 μm, although emission at 10,6 μm is the most widely used. Of the several types of CO₂ laser that are available, the waveguide, the low power sealed tube and the transversely excited atmospheric (TEA) lasers are used for small scale materials processing applications. The fast axial flow CO₂ laser and the less widely used slow flow laser, are used for thick section cutting 1-15 mm and deep penetration welding. While these lasers share the same active medium, they have important functional characteristics, which contribute to the wide range of CW (continuous wave) powers, and pulse powers (Hilton, 2004a).

The active medium in a CO₂ laser is a mixture of carbon dioxide, nitrogen and (generally) helium. It is the carbon dioxide which produces the laser light, while the nitrogen molecules help excite the CO₂ molecules and increase the efficiency of the light generation process. The helium plays a dual role in assisting heat transfer from the gas caused by the electric discharge used to excite the gas, and it also helps the CO₂ molecules to return to the ground state (Hilton, 2004a).

2.1.2.1.1 Sealed Tube CO₂ Lasers. These lasers are operated as conventional gas discharge lasers in the form of long narrow glass tubes, filled with the lasing gas mixture. Electrodes at either end of the tube provide the discharge current. A totally reflecting and partially transmitting mirror, usually made from polished metal and coated zinc selenide, respectively, form the resonant cavity. The tube is sealed using Brewster angled windows. Figure 2.4 shows a schematic drawing of a sealed tube CO₂

laser. As the electric discharge in the tube breaks down the CO_2 molecules, an ordinary gas mixture would stop working very quickly and so methods are provided to cause the CO_2 to regenerate, either by addition of hydrogen or water or by the use of catalytic action. Several thousand hours of operation are possible with sealed tube CO_2 lasers before the tube has to be cleaned and re-filled or replaced. DC and sometimes RF discharges are used with these lasers. CW power up to about 200 W is available from these lasers with good beam quality. Pulsed power supplies can produce laser pulses lasting 0,1-1 msec with peak powers of 5-10 times the CW power level (Hilton, 2004a).

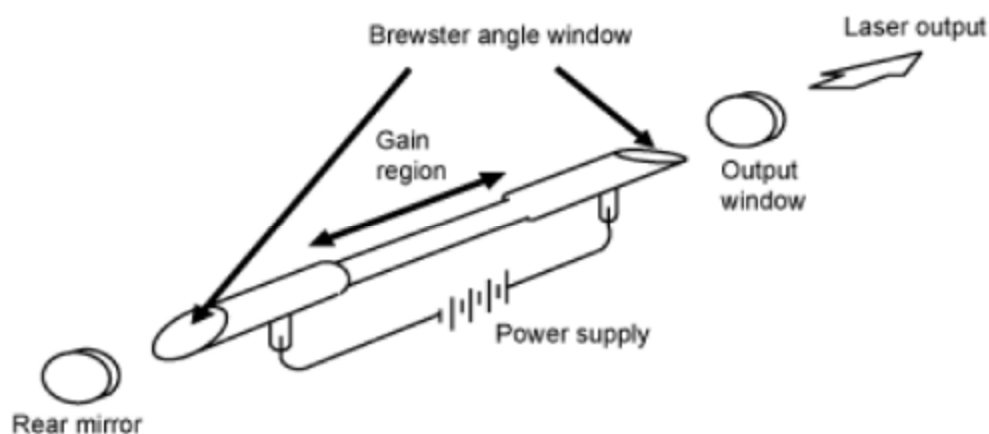


Figure 2.4 Sealed tube CO_2 laser schematic (Hilton, 2004a)

2.1.2.1.2 Waveguide CO_2 Lasers. The waveguide laser is an efficient way to produce a compact CO_2 laser. It consists of (see Figure 2.5) two transverse RF electrodes separated by insulating sections that form a bore region. The lateral dimensions of the bore are a few millimeters, which propagates the beam in “waveguide mode”. The tube is normally sealed with a gas reservoir separate from the tube itself. The small bore allows high pressure operation and provides rapid heat removal; both of which lead to high gain and high power output from a compact unit (Hilton, 2004a).

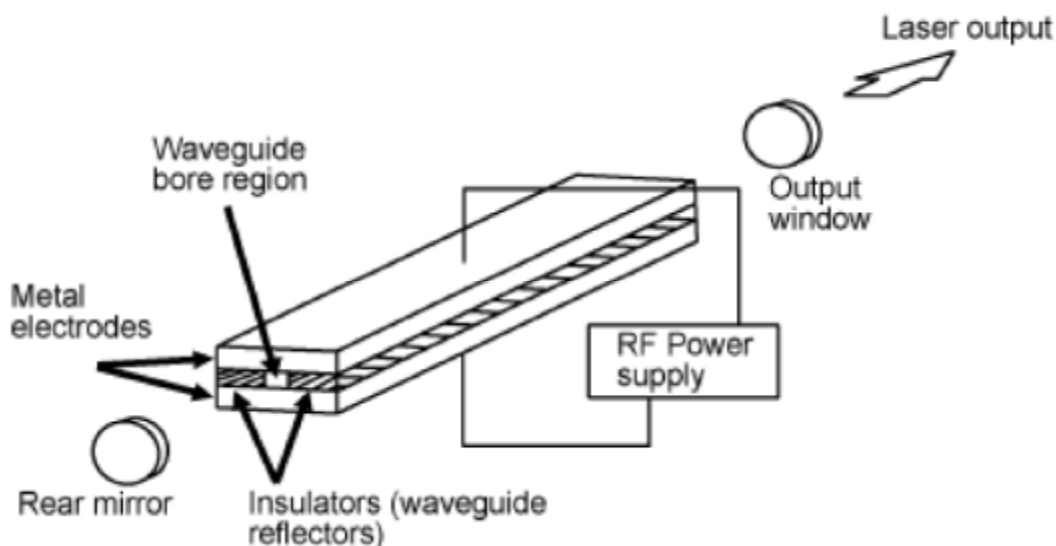


Figure 2.5 Waveguide CO₂ laser schematic (Hilton, 2004a)

2.1.2.1.3 TEA CO₂ Lasers. Discharge instabilities prevent operation of CW CO₂ lasers at pressures above about 100 mbar. Pulses in the nanosecond to microsecond duration range can be produced by passing a pulsed current transversely through the lasing gas. Such TEA (transversely excited atmospheric) lasers operate at gas pressures of one atmosphere and above, in order to obtain high energy output per unit volume of gas. A transverse discharge from two long electrodes is employed (see Figure 2.6). Prior to application of the pulsed discharge, a form of pre-ionization is used to ionize the space between the electrodes uniformly, thus allowing the discharge to proceed in a uniform fashion over the entire electrode assembly. The prime attractions of TEA lasers are their ability to generate short intense pulses and the extraction of high power per unit volume of laser gas. Pulse duration as low as a few tens of nanoseconds up to a few microseconds are possible. Pulse energies range from the millijoule region to 500 Joules at pulse repetition rates from about 300 Hz down to a single shot (Hilton, 2004a).

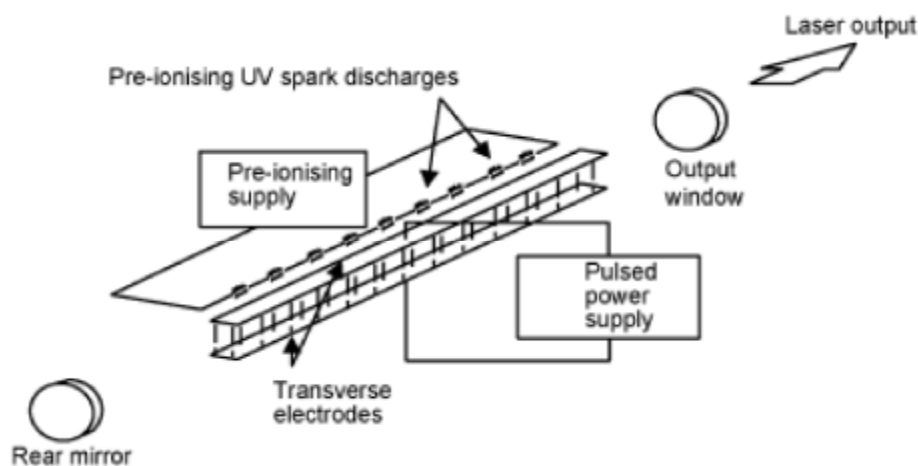


Figure 2.6 TEA CO₂ laser schematic (Hilton, 2004a).

2.1.2.2 Carbon Monoxide Laser Welding

In recent years, there has been considerable interest in the electric-discharge laser based on the vibrational–rotational transitions from the ground state of carbon monoxide (CO). These lasers have higher quantum conversion efficiency, shorter wavelength and higher transmission through the optical fiber, which is suitable for industrial processes compared to the CO₂ laser. This is a consequence of the shorter 5 to 5,6 μm wavelength of the carbon monoxide laser welding leading to reduced beam-plasma interaction. (Schellhorn & Eichhorn, 1996)

Schematic diagram of the apparatus is shown in Figure 2.7 1. Helium, nitrogen, and carbon monoxide enter the system through gas sources 1, 2, and, 3 passing through the mixing bottle 7 and pre-cooler 8. It enters the heat exchanger 9 and the temperature of the gas mixture is decreased to 100 K, from here, the cooled gas mixture goes through the divider 10 and two polytetrafluoroethylene tubes. It enters into two buffers 12, where the cooled gas mixture is injected into two polytetrafluoroethylene tubes (each 2,5 cm in diameter, 50 cm in length) via two ring gaps in the buffers. Here, the temperature of the gas mixture is degraded further and the gas mixture flows to the ends of the discharge

tubes. The gas mixture is discharged to a confluent container 16, the discharged gas mixture is exhausted from the container by a pumping system at the rate of 300 liter/s. The cupric heat exchanger, divider, confluent container and discharge tubes are situated in liquid nitrogen (Li & Fontana, 2003).

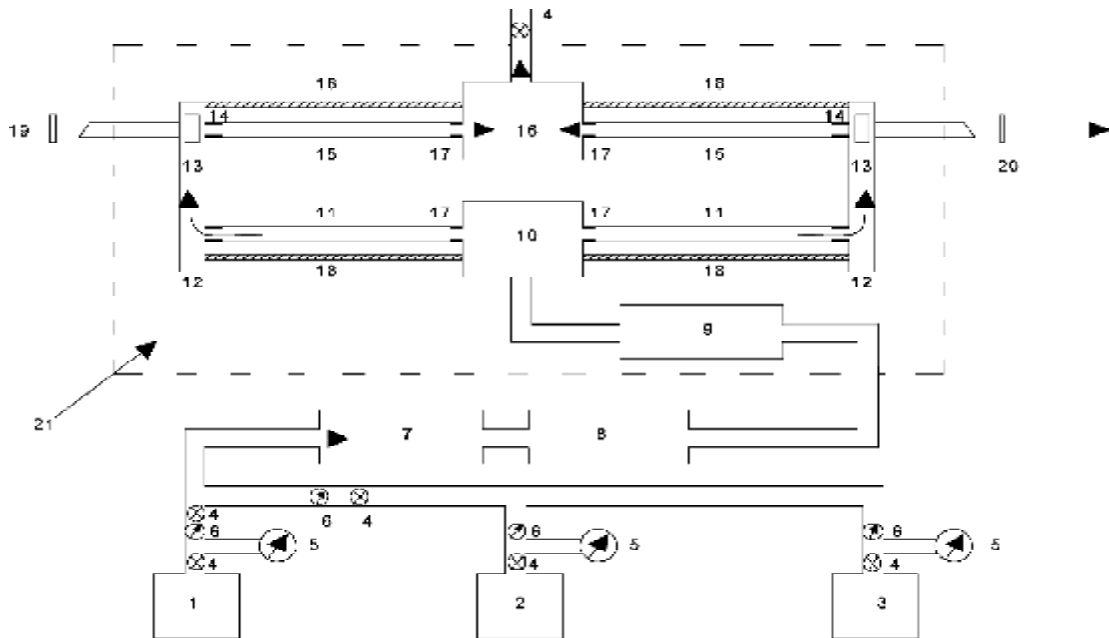


Figure 2.7 1. Schematic diagram of the CO laser. (1. He, 2. N₂, 3. CO, 4. Switch, 5. Pressure meter, 6. Flow meter, 7. Mix bottle, 8. Pre-cooler, 9. Cupric heat exchanger, 10. Divider, 11. Polytetrafluoroethylene tube, 12. Buffer, 13. Adjustable ring-gap (0.1<0.7 mm), 14. Anode, 15. Polytetrafluoroethylene discharge tube, 16. Confluent container and cathode, 17. Corrugated pipe, 18. Insulation support, 19. Total reflective mirror, 20. Ge plate, 21. Liquid nitrogen cell.) (Li & Fontana, 2003)

2.1.2.3 Nd:YAG Laser Welding

The Nd:YAG (Neodymium-doped Yttrium Aluminum Garnet) laser is one of the most versatile laser sources used in materials processing, Figure 2.8. The relative robustness and compactness of the laser and the possibility for the 1.06 micron light it

produces to be transmitted to the workpiece via silica optical fibres, are two features which contribute to its success. Nd:YAG lasers were first commercialized operating mainly in pulsed mode, where the high peak powers which can be generated were found useful in applications such as drilling, cutting and marking. These pulsed lasers can also be utilized for welding a range of materials. More recently, high power (up to 10 kW), continuous wave (CW) Nd:YAG lasers have become available. The Nd:YAG crystals in these lasers can be pumped either using white light flashlamps or, more efficiently, using laser diodes. The latter methods are used to produce high quality beams, which can be focused to smaller spots (and therefore produce higher power densities) than the flashlamp pumped lasers. Because of the possibility of using fiber optic beam delivery, these lasers are often used in conjunction with articulated arm robots, in order to work on components of complex shape (Hilton, 2004b).

Because of the wide range of applied power and power densities available from Nd:YAG lasers, different welding methods are possible. If the laser is in pulsed mode, and if the surface temperature is below the boiling point, heat transport is predominantly by conduction and a conduction limited weld is produced. If the applied power is higher (for a given speed), boiling begins in the weld pool and a deep penetration weld can be formed. After the pulse, the material flows back into the cavity and solidifies. Both of these methods can be used to produce spot welds. A seam weld is produced by a sequence of overlapping deep penetration “spot” welds or by the formation of a continuous molten weld pool. For the former, once the energy input is sufficient to ensure that the weld does not solidify between pulses, the “keyhole” type weld normally associated with CO₂ laser welding can be formed. Pulsed laser welding is normally used at thicknesses below about 3 mm. Higher power 4-10 kW CW Nd:YAG lasers are capable of keyhole type welding in materials from 0,8 mm (car body steel) to 15 mm (ship steel) thicknesses (Hilton, 2004b).

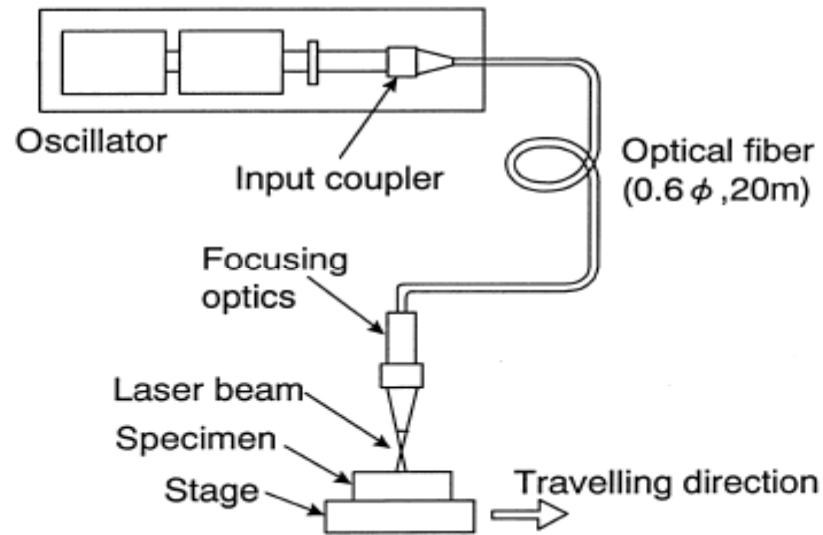


Figure 2.8 Schematic diagram of the equipment and specimen. (Kawano, 1998)

Nd:YAG laser welding is used commercially on a wide range of C-Mn steels, coated steels, stainless steels, aluminum alloys, titanium and molybdenum. The low heat input welding offered by Nd:YAG lasers is utilized in the electronics, packaging, domestic goods and automotive sectors, and significant interest has been shown more recently, particularly for the high power CW lasers, in the shipbuilding, oil and gas, aerospace and yellow goods sectors. Important R&D (Research & Development) issues involve development of high power lasers of better beam quality, use of distributed energy in the beam focus, weld quality maintenance for both thick and thin sections and weld classification (Hilton, 2004b).

2.1.2.4 Comparison of laser welding methods

Since the mid 1980s it was believed that Nd:YAG laser light (1,06 μm wavelength) could offer major advantages over CO₂ laser light (10,6 μm wavelength) for welding applications, such as enhanced coupling to reflective metals, use of an optic fiber for beam delivery (offering great flexibility in the welding process) and apparent increased

process efficiency at the same power. Only in recent years, however, have Nd:YAG lasers with more than 3 kW of power been commercially available. The use of such high-power Nd:YAG laser light for welding has presented new issues and problems when compared to high-power CO₂ laser welding (Greses & Hilton, 2004).

The spot diameter of a CO laser is similar to that for a CO₂ laser, but because of the smaller wavelength, similar but perhaps slightly greater penetration might be expected. In the case of the Nd:YAG laser, the mode structure is relatively poor that the spot size can be even bigger than it is for a CO₂ laser (See Figure 2.9 and 2.10), since its wavelength is so small compared to the keyhole radius. In that case, much greater penetration may occur with fairly random interference taking place between different reflections of the beam within the keyhole (Dowden & Kapadia, 1996).

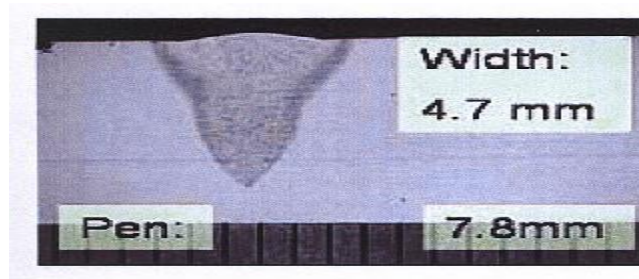


Figure 2.9. Wine-glass weld shape characteristic of CO₂ laser welding. Cross-sections at 0,75 m/min and 3,5 kW (Greses & Hilton, 2004)

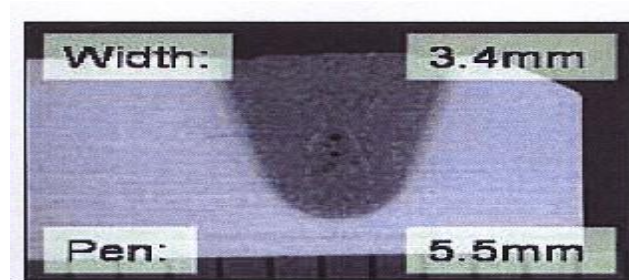


Figure 2.10 Wine-glass weld shape characteristic of Nd:YAG laser welding. Cross-sections at 0,75 m/min and 3,5 kW (Greses & Hilton, 2004)

2.1.2.5 New Trends in Laser Welding

Recently so-called hybrid welding, which is a combination of laser beam and arc welding processes, has been a target of great interest not only in the research field but also for the industrial use. Hybrid process seems to be very effective in overcoming the shortcomings of plain laser welding (Dilthey & Wieschemann, 2000). Not only for reason of filler wire addition, but also for the extra heat coming from the arc makes the process more effective by increasing the welding speed. For example, 20 mm thick austenitic stainless steel was welded using narrow gap configuration with a multi-pass technique (Figure 2.11). Two welding procedures were used: Nd:YAG laser welding with filler wire and in combination with of GMAW (the hybrid process). In the welding experiments, it was noticed that both processes are feasible for welding thicker sections with good quality and with minimal distortions (Jokinen & Kujanpää, 2003).

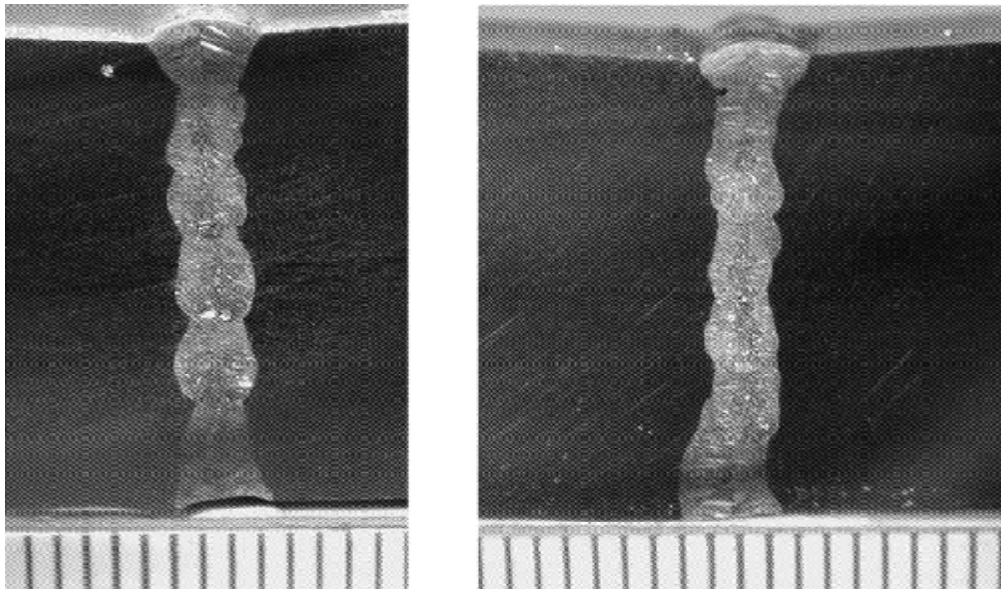


Figure 2.11 Cross-sections of the welds with plate thickness of 20 mm and five passes. Parameters: laser power, 3 kW; welding speed, 0,5 m/min; filler wire, 4,5-6,0 m/min (Jokinen & Kujanpää, 2003)

As can be seen in Figure 2.12, very thin pieces as well as thick materials can be welded, the diameter of the thermocouple being welded is 0,5 mm.

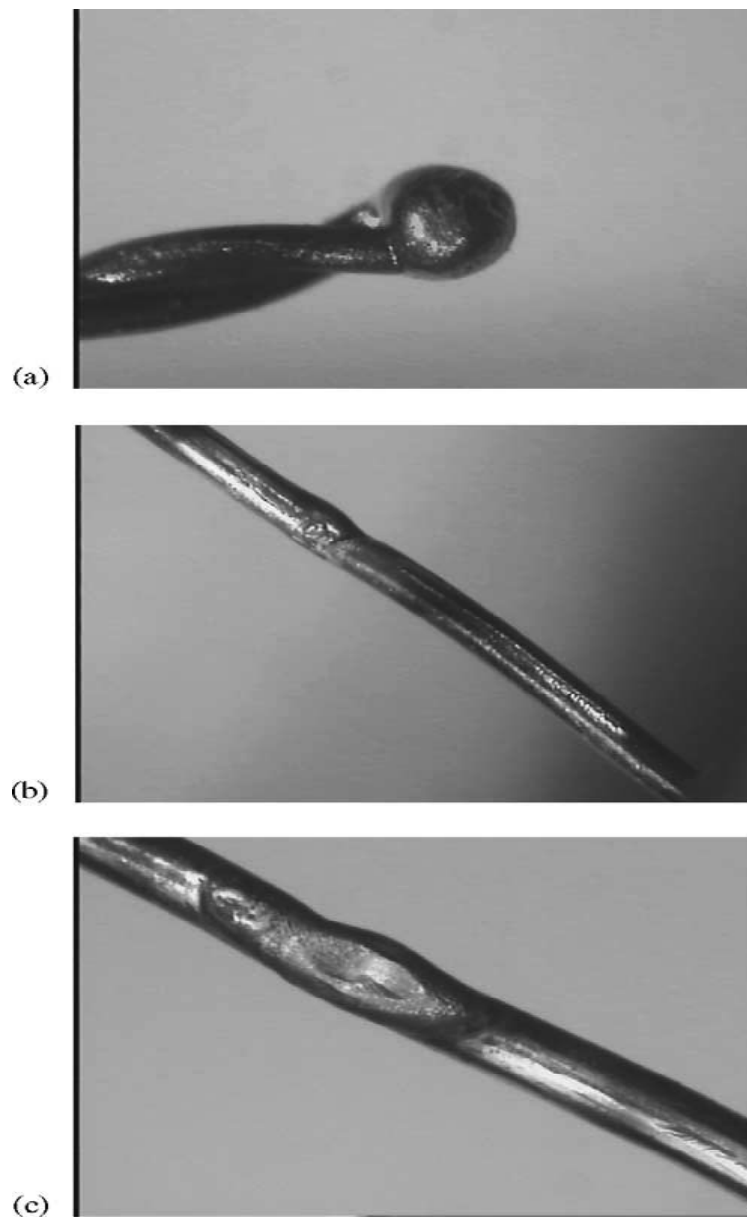


Figure 2.12 Typical weld geometry for 0.5 mm diameter thermocouples. (a) Argon arc welded, (b) diode laser welded and (c) Nd:YAG laser welded (Triantafyllidis, Schmidt & Li, 2003)

Furthermore, laser welding can be used to join different materials. An example in the laser beam welding of difficult to join material such as hard metals (K10 and K40 “containing WC”) to steel, focusing the laser beam sensitively to a specific point as shown in figure 2.13, prevents the formation of Al_2O_3 phase which is a common feature observed in the joint of these metals (Figure 2.14) (Costa, Quintino & Greitmann, 2003).

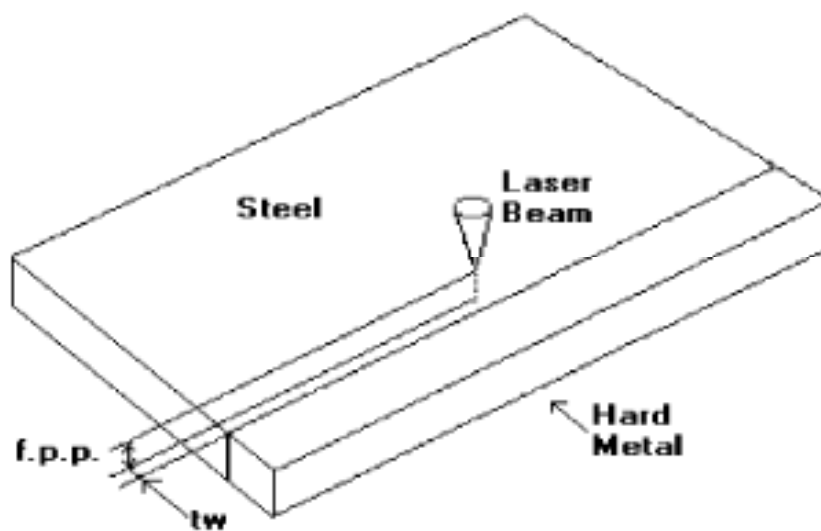


Figure 2.13 Laser beam welding hard metals to steel (Costa, Quintino & Greitmann ,2003)

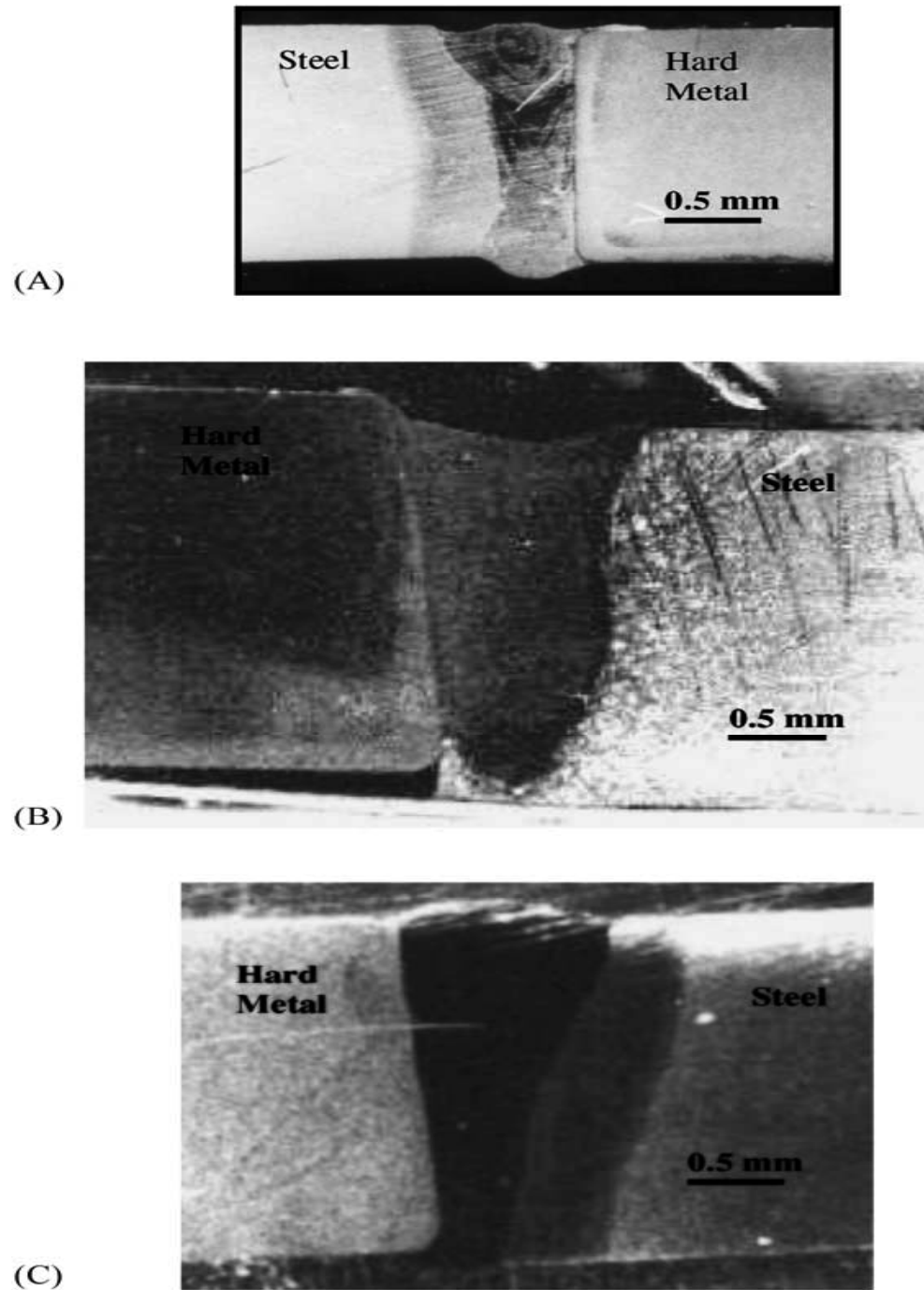


Figure 2.14 (A) K10 sample welded with (cw) Nd:YAG laser, $t_w = 0,15$ mm (macro analysis); (B) K40 sample welded with (pw) Nd:YAG laser, $t_w = 0,15$ mm (macro analysis); (C) K40 sample welded with (cw) CO₂ laser, $t_w = 0,1$ mm (macro analysis) (Costa et al., 2003)

In the joining of same series metals like AISI12L13, AISI 304L, a better penetration is supplied by focusing on a certain angle. This process is illustrated in Figure 2.15.

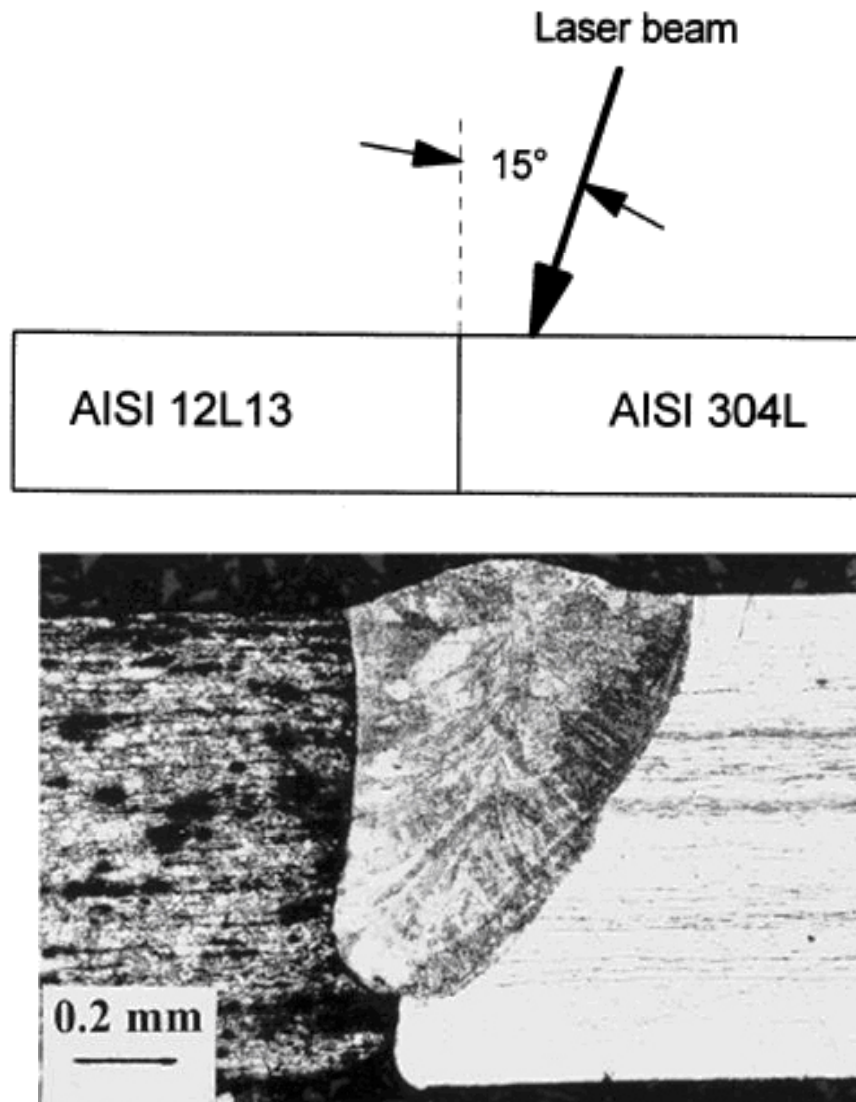


Figure 2.15 Showing that a laser beam with 0.12 mm offset towards AISI304L and tilted 15° with respect to the plane of the butt joint fit-up face used in autogenous butt welding (Li & Fontana, 1998)

Furthermore, the microstructure, penetration depth and porosity formation can be controlled by applying the laser beam as shown in Figure 2.16 and 2.17.

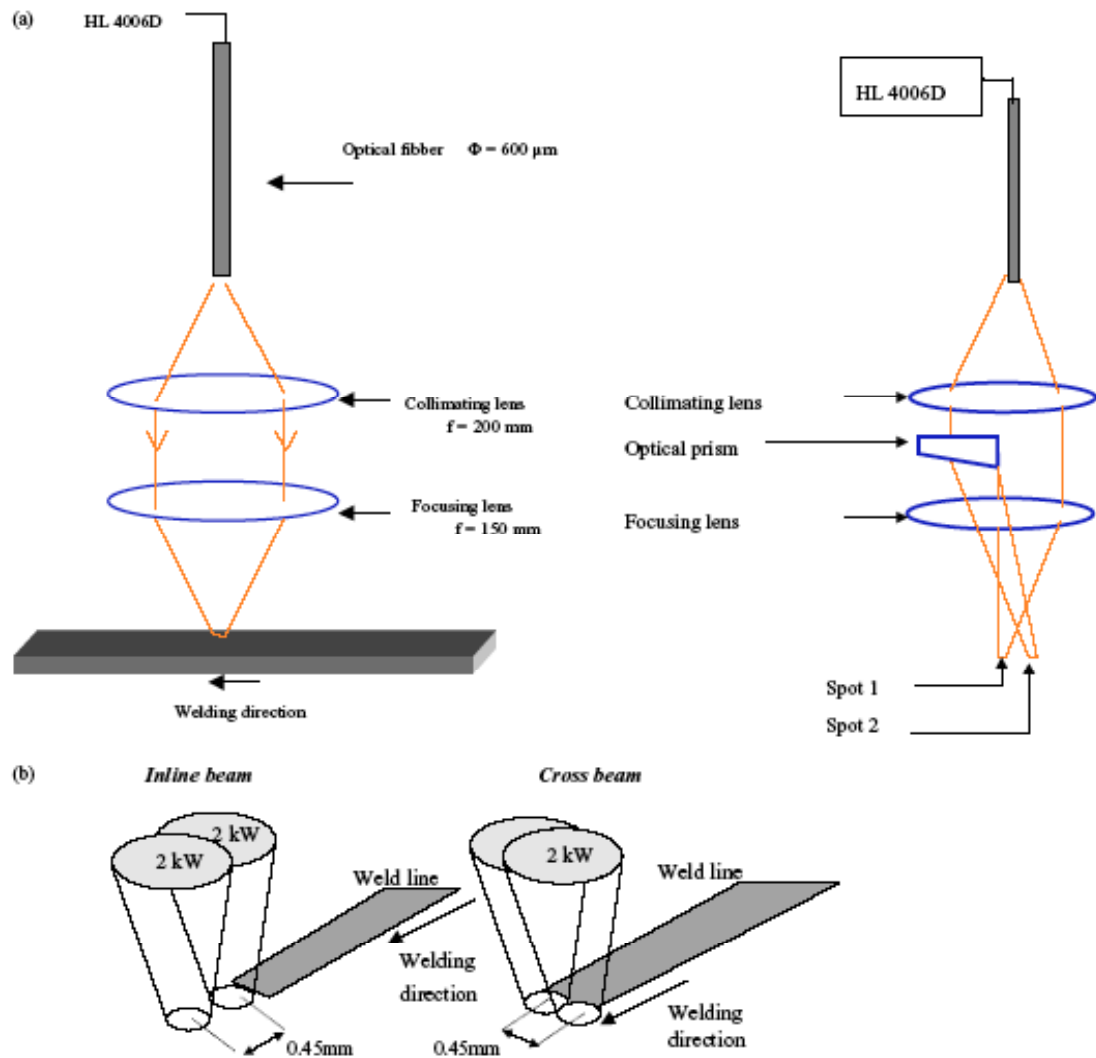


Figure 2.16 (a) Single spot and dual spot laser welding, and (b) inline beam and cross-beam configurations (Haboudou, Peyre, Vannes & Peix, 2003)

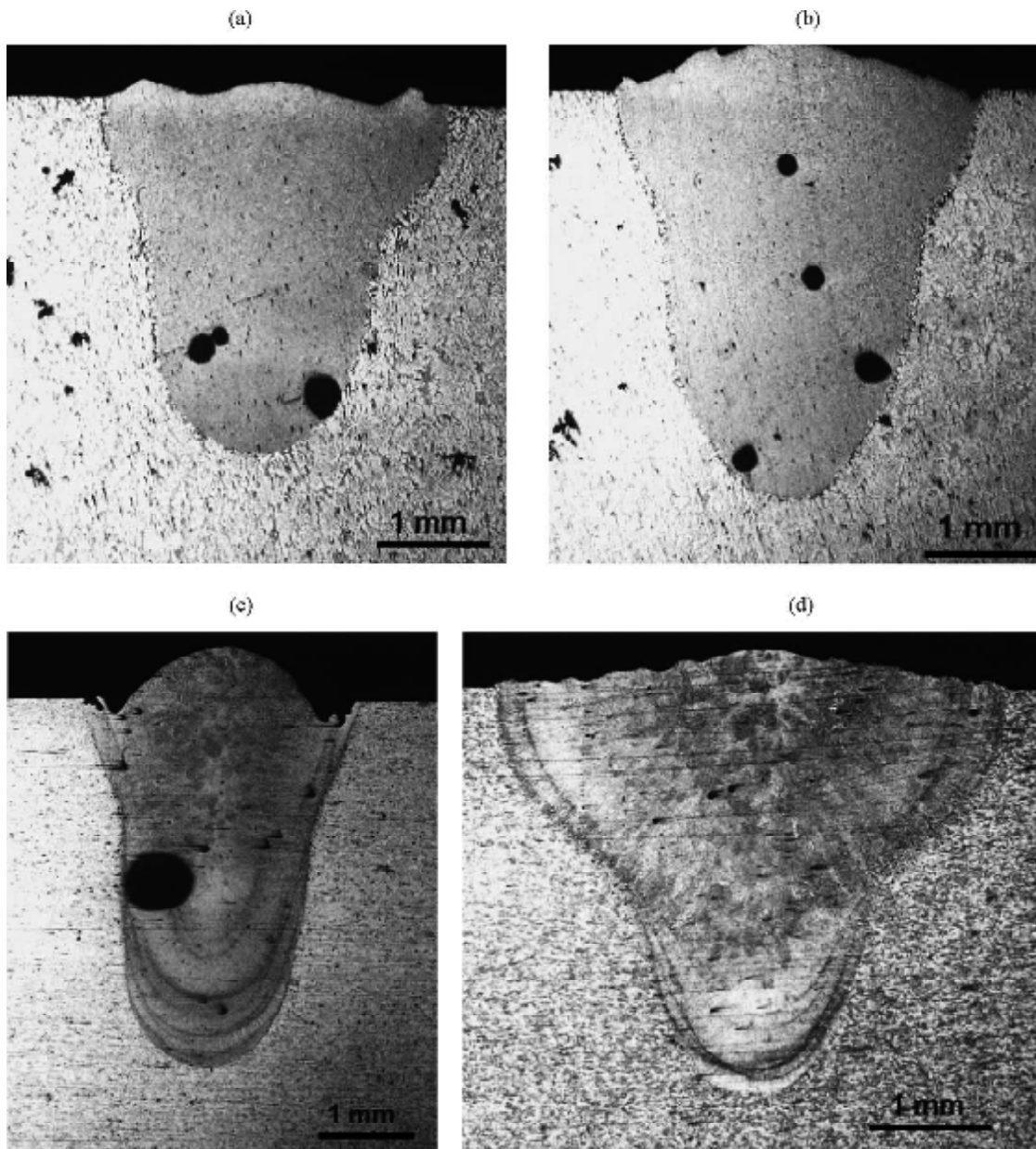


Figure 2.17 Cross-sectional macrostructure of AA5083 and A356 weld lines: (a) A356 single spot 5 m/min; (b) A356 dual spot (0.45 mm inter-distance) at 4 m/min; (c) 5083 single spot 5 m/min; (d) 5083 dual beam (0,75 mm inter-distance) at 2,5 m/min. (Haboudou et al., 2003)

2.1.2.6 Advantages of Laser Welding

Laser welding has shown many advantages over traditional welding methods in numerous applications. The advantages are mainly based on very precise and powerful heat source of laser light, which change the phenomena of welding process when compared with traditional welding methods. According to the phenomena of the laser welding, penetration is deeper and thus welding speed is higher. Because of the precise power source and high-welding speed, the heat input to the workpiece is small and distortions are reduced. Also, the shape of laser weld is less critical for distortions than traditional welds. For welding thick sections, the usability of lasers is not so practical than with thin sheets, because with power levels of present Nd:YAG lasers, depth of penetration is limited up to about 10 mm by single-pass welding. One way to overcome this limitation is to use multi-pass laser welding, in which narrow gap and filler wire is applied. By this process, thick sections can be welded with smaller heat input and then with smaller distortions and the process seems to be very effective compared to “traditional” welding methods (Jokinen & Kujanpää, 2003).

The advantages of laser welding can be summarized as follows:

As the overall heat input is low, minimal thermal stress is introduced into the material welded. This results in reduced distortion.

The Nd:YAG laser power is delivered to the workpiece via a flexible optical fibre. Coupled with robotic manipulation of the laser head, this is a very flexible technique, which can be readily adapted for complicated weld geometries. CO₂ laser power on the other hand is delivered using a less flexible system of mirrors, most often by a less flexible type of welding head manipulation, e.g. an (x,y) gantry (Allen, 2004).

Unlike electron beam welding, laser light can be transmitted through air with minimal attenuation. Operation under vacuum or reduced pressure conditions is not therefore necessary (Allen, 2004).

Using beam splitters or angled mirrors the beam can be shared or switched between different work stations, further increasing the flexibility of a manufacturing facility. Laser welding speed is of the order of meters per minute, but depends on the power available, spot size and hence power density, material type, and thickness to be welded (Allen, 2004).

It is suitable for single-sided deep penetration welding. The need for multiple passes can often therefore be eliminated (Allen, 2004).

It is possible to join different thicknesses of sheet together, e.g. for the production of tailored blanks. These are then used as the basis for pressed or formed parts for automotive bodies.

It is possible to join dissimilar alloys as the melting is localized during welding. Joining metals of very different melting points is also possible in principle. However, this can be complicated by the formation of brittle intermetallics at the joint, e.g. joining aluminum alloys to steel (Allen, 2004).

In a production line environment, laser welding can be automated to the 'push-button' level.

2.2 Aluminum Alloys and the Welding of Aluminum Alloys

2.2.1 Aluminum Alloys

Aluminum is a low density metal that can be strengthened by the addition of alloying elements and/or work hardening. Strengthening by alloying may be achieved by one of two mechanisms, solid solution strengthening or precipitation strengthening. Alloys which are work hardened are known as non-heat treatable, and those which are precipitation hardened as heat treatable. Strengthening by heat treatment is known as tempering.

Table 2.2 Density and yield strength of pure elements used to manufacture high performance alloys (Cardelli, 1999).

Metal	Density, 10⁻³ kg/m³	Yield strength, MPa	Specific strength*, Nm/kg
Magnesium	1,74	69	39,6
Beryllium	1,85	120	64,9
Aluminum	2,70	30	11,1
Titanium	4,51	140	31,0
Nickel	8,90	148	16,6
Copper	8,93	69	7,7
Tungsten	19,25	550	28,6
Molybdenum	10,22	345	33,8
Niobium	8,57	105	12,3

The specific strength is defined as:

$$* \text{ specific strength} = \frac{\text{strength}}{\text{density}} \Rightarrow \left[\frac{\text{MPa}}{\frac{\text{kg}}{\text{m}^3}} \equiv \frac{10^3 \text{ Nm}}{\text{kg}} \right] \text{ (Cardelli, 1999).}$$

Consequently, certain aluminum alloys are materials that possess high specific strength and stiffness (See Table 2.2). This makes them ideal materials for application in those areas where light weight and high strength are important. Such applications are in the aerospace sector, where weight reduction leads to reduced fuel consumption and increased payloads, or in the automotive sector, where light-weighting leads to improved performance and reduced fuel consumption and exhaust emissions.

The ease with which aluminum alloys can be fabricated in a range of finished and semi-finished products, i.e. castings, forgings, rolled plate and sheet, and extrusions, also leads to their ready application in a variety of market sectors. In addition, certain aluminum alloys have excellent corrosion resistance, ideally suiting them to marine applications, e.g. in shipbuilding and offshore structures. The high thermal and electrical conductivity of aluminum alloys also leads to their use in micro-electronics, conducting cable and capacitors, as are used in the electrical, computing and telecommunications industries.

The Aluminum Alloy Temper and Designation System - In North America, The Aluminum Association Inc. is responsible for the allocation and registration of aluminum alloys. Currently there are over 400 wrought aluminum and wrought aluminum alloys and over 200 aluminum alloys in the form of castings and ingots registered with the Aluminum Association. Aluminum alloys can be categorized into a number of groups based on the particular material's characteristics such as its ability to respond to thermal and mechanical treatment and the primary alloying element added to the aluminum alloy. When we consider the numbering / identification system used for aluminum alloys, the above characteristics are identified. The wrought and cast aluminums have different systems of identification. The wrought system is a 4-digit system and the castings having a 3-digit and 1-decimal place system (Anderson, 2004b).

Wrought Alloy Designation System - We shall first consider the 4-digit wrought aluminum alloy identification system. The first digit (Xxxx) indicates the principal

alloying element, which has been added to the aluminum alloy and is often used to describe the aluminum alloy series, i.e., 1000 series, 2000 series, 3000 series, up to 8000 series.

The second single digit (xXxx), if different from 0, indicates a modification of the specific alloy, and the third and fourth digits (xxXX) are arbitrary numbers given to identify a specific alloy in the series. Example: In alloy 5183, the number 5 indicates that it is of the magnesium alloy series, the 1 indicates that it is the 1st modification to the original alloy 5083, and the 83 identifies it in the 5xxx series.

The only exception to this alloy numbering system is with the 1xxx series aluminum alloys (pure aluminums) in which case, the last 2 digits provide the minimum aluminum percentage above 99%, i.e., Alloy 13(50) (99,50% minimum aluminum).

Cast Alloy Designation - The cast alloy designation system is based on a 3 digit-plus decimal designation xxx.x (i.e. 356.0). The first digit (Xxx.x) indicates the principal alloying element, which has been added to the aluminum alloy.

The second and third digits (xXX.x) are arbitrary numbers given to identify a specific alloy in the series. The number following the decimal point indicates whether the alloy is a casting (.0) or an ingot (.1 or .2). A capital letter prefix indicates a modification to a specific alloy.

Example: Alloy - A356.0 the capital A (Axxx.x) indicates a modification of alloy 356.0. The number 3 (A3xx.x) indicates that it is of the silicon plus copper and/or magnesium series. The 56 in (Ax56.0) identifies the alloy within the 3xx.x series, and the .0 (Axxx.0) indicates that it is a final shape casting and not an ingot.

The Aluminum Temper Designation System - If we consider the different series of aluminum alloys, we will see that there are considerable differences in their

characteristics and consequent application. The first point to recognize, after understanding the identification system, is that there are two distinctly different types of aluminum within the series mentioned above. These are the Heat Treatable Aluminum alloys (those which can gain strength through the addition of heat) and the Non-Heat Treatable Aluminum alloys. This distinction is particularly important when considering the affects of arc welding on these two types of materials.

The 1xxx, 3xxx, and 5xxx series wrought aluminum alloys are non-heat treatable and are strain hardenable only. The 2xxx, 6xxx, and 7xxx series wrought aluminum alloys are heat treatable and the 4xxx series consist of both heat treatable and non-heat treatable alloys. The 2xx.x, 3xx.x, 4xx.x and 7xx.x series cast alloys are heat treatable. Strain hardening is not generally applied to castings.

The heat treatable alloys acquire their optimum mechanical properties through a process of thermal treatment, the most common thermal treatments being solution heat treatment and artificial aging. Solution heat treatment is the process of heating the alloy to an elevated temperature (around 530 °C) in order to put the alloying elements or compounds into solution. This is followed by quenching, usually in water, to produce a supersaturated solution at room temperature. Solution heat treatment is usually followed by aging. Aging is the precipitation of a portion of the elements or compounds from a supersaturated solution in order to yield desirable properties.

The non-heat treatable alloys acquire their optimum mechanical properties through strain hardening. Strain hardening is the method of increasing strength through the application of cold working.

Temper codes of aluminum alloys and their meaning are given in Table 2.3.

Table 2.3 Temper codes of aluminum alloys and meaning (Anderson, 2004b).

Letter	Meaning
F	As fabricated, i.e. no special controls over thermal and mechanical conditions experienced during processing.
O	Annealed (at high temperature) to produce materials of the lowest possible strength for the given chemical composition. Work hardening is lost by recovery and recrystallisation, and precipitation hardening elements dissolve into solution. High formability.
H	This is a temper designation for work hardened wrought alloys, tempered through some combination of strain hardening, e.g. cold rolling, and thermal treatment to produce some subsequent reduction in strength.
W	This is an unstable temper, used as a designation for precipitation hardened alloys which naturally age at room temperature, after solution heat treatment and quenching, over a period of months or even years.
T	This is a temper designation for precipitation hardened wrought alloys, applying to those alloys which naturally age at room temperature over a period of a few weeks, or can be artificially aged at elevated temperatures, after solution heat treatment and quenching

The O, H and T tempers are the most frequently used. The work hardened H tempers in turn contain a number of sub-divisions, designated by two digits:

H1x - where x is a number between 1 and 9, indicating the extent to which a material has been work hardened, e.g. H12 - 1/4 hard, H14 - half hard, H18 - fully hard, H19 - extra hard.

H2x - where x is as above, this denotes the work hardening has been reduced by subsequent partial annealing, e.g. H22, H24.

H3x - where the x is as above, this denotes the alloy has been thermally stabilized by a low-temperature treatment, e.g. H32, H34. Without thermal stabilization, alloys in this class would age-soften at room temperature.

In turn, a third digit (from 1 to 9) is sometimes added when the temper is different from but close to those of the two digits H temper designation to which it is added. A common example would be H321, where the 1 denotes stress relieving due to additional stretching after rolling (and thermal stabilizing), resulting in a temper with properties just below those of H32. Similarly, H111 would be a temper intermediate between H11 and O temper.

The precipitation hardened T tempers also contain a number of sub-divisions, designated by one or more digits. The most common are:

T1 - Naturally aged after cooling from an elevated temperature shaping process, such as extruding.

T2 - Cold worked after cooling from an elevated temperature shaping process and then naturally aged.

T3 - Solution heat-treated, cold worked and naturally aged.

T4 - Solution heat-treated and naturally aged.

T5 - Artificially aged after cooling from an elevated temperature shaping process.

T6 - Solution heat-treated and artificially aged.

T7 - Solution heat-treated and stabilized (overaged).

T8 - Solution heat-treated, cold worked and artificially aged.

T9 - Solution heat treated, artificially aged and cold worked.

T10 - Cold worked after cooling from an elevated temperature shaping process and then artificially aged.

Additional digits indicate stress relief.

Examples:

TX51 or TXX51 – Stress relieved by stretching.

TX52 or TXX52 – Stress relieved by compressing (Anderson, 2004b).

2.2.1.1 Characteristics of Aluminum Alloys

1xxx Series Alloys – (non-heat treatable – with ultimate tensile strength of 68 to 185 MPa) this series is often referred to as the pure aluminum series because it is required to have 99,0% minimum aluminum. They are weldable. However, because of their narrow melting range, they require certain considerations in order to produce acceptable welding procedures. When considered for fabrication, these alloys are selected primarily for their superior corrosion resistance such as in specialized chemical tanks and piping or for their excellent electrical conductivity as in bus bar applications. These alloys have relatively poor mechanical properties and would seldom be considered for general structural applications. These base alloys are often welded with matching filler material or with 4xxx filler alloys dependent on application and performance requirements (Anderson, 2004b).

2xxx Series Alloys – (heat treatable– with ultimate tensile strength of 185 to 425 MPa) these are aluminum / copper alloys (copper additions ranging from 0,7 to 6,8%), and are high strength, high performance alloys that are often used for aerospace and aircraft applications. They have excellent strength over a wide range of temperatures. Some of these alloys are considered non-weldable by the arc welding processes because of their susceptibility to hot cracking and stress corrosion cracking; however, others are arc welded very successfully with the correct welding procedures. These base materials are often welded with high strength 2xxx series filler alloys designed to match their performance, but can sometimes be welded with the 4xxx series fillers containing silicon or silicon and copper, dependent on the application and service requirements (Anderson, 2004b).

3xxx Series Alloys – (non-heat treatable – with ultimate tensile strength of 110 to 280 MPa) These are the aluminum / manganese alloys (manganese additions ranging from 0,05 to 1,8%) and are of moderate strength, have good corrosion resistance, good formability and are suited for use at elevated temperatures. One of their first uses was pots and pans, and they are the major components today for heat exchangers in vehicles and power plants. Their moderate strength, however, often precludes their consideration for structural applications. These base alloys are welded with 1xxx, 4xxx and 5xxx series filler alloys, dependent on their specific chemistry and particular application and service requirements (Anderson, 2004b).

4xxx Series Alloys – (heat treatable and non-heat treatable – with ultimate tensile strength of 170 to 380 MPa). These are the aluminum / silicon alloys (silicon additions ranging from 0,6 to 21,5%) and are the only series that contain both heat treatable and non-heat treatable alloys. Silicon, when added to aluminum, reduces its melting point and improves its fluidity when molten. These characteristics are desirable for filler materials used for both fusions welding and brazing. Consequently, this series of alloys is predominantly found as filler materials. Silicon, independently in aluminum, is non-heat treatable; however, a number of these silicon alloys have been designed to have additions of magnesium or copper, which provides them with the ability to respond favorably to solution heat treatment. Typically, these heat treatable filler alloys are used only when a welded component is to be subjected to post weld thermal treatment (Anderson, 2004b).

5xxx Series Alloys – (non-heat treatable – with ultimate tensile strength of 125 to 350 MPa) These are the aluminum / magnesium alloys (magnesium additions ranging from 0,2 to 6,2%) and have the highest strength of the non-heat treatable alloys. In addition, this alloy series is readily weldable, and for these reasons they are used for a wide variety of applications such as shipbuilding, transportation, pressure vessels, bridges and buildings. The magnesium base alloys are often welded with filler alloys, which are selected after consideration of the magnesium content of the base material, and the

application and service conditions of the welded component. Alloys in this series with more than 3,0% magnesium are not recommended for elevated temperature service above 65 °C because of their potential for sensitization and subsequent susceptibility to stress corrosion cracking. Base alloys with less than approximately 2,5% magnesium are often welded successfully with the 5xxx or 4xxx series filler alloys. The base alloy 5052 is generally recognized as the maximum magnesium content base alloy that can be welded with a 4xxx series filler alloy. Because of the problems associated with eutectic melting and associated poor as-welded mechanical properties, it is not recommended to weld material in this alloy series, which contain higher amounts of magnesium with the 4xxx series fillers. The higher magnesium base materials are only welded with 5xxx filler alloys, which generally match the base alloy composition (Anderson, 2004a)..

6XXX Series Alloys – (heat treatable – with ultimate tensile strength of 125 to 400 MPa) These are the aluminum / magnesium - silicon alloys (magnesium and silicon additions of around 1,0%) and are found widely throughout the welding fabrication industry, used predominantly in the form of extrusions, and incorporated in many structural components. The addition of magnesium and silicon to aluminum produces a compound of magnesium-silicide, which provides this material its ability to become solution heat treated for improved strength. These alloys are naturally solidification crack sensitive, and for this reason, they should not be arc welded autogenously (without filler material). The addition of adequate amounts of filler material during the arc welding process is essential in order to provide dilution of the base material, thereby preventing the hot cracking problem. They are welded with both 4xxx and 5xxx filler materials, dependent on the application and service requirements (Anderson, 2004b).

7XXX Series Alloys – (heat treatable – with ultimate tensile strength of 470 to 600 MPa) These are the aluminum / zinc alloys (zinc additions ranging from 0,8 to 12,0%) and comprise some of the highest strength aluminum alloys. These alloys are often used in high performance applications such as aircraft, aerospace, and competitive sporting equipment. Like the 2xxx series of alloys, this series incorporates alloys which are

considered unsuitable candidates for arc welding, and others, which are often arc welded successfully. The commonly welded alloys in this series, such as 7005, are predominantly welded with the 5xxx series filler alloys (Anderson, 2004b).

2.2.2 The Welding of Aluminum Alloys

2.2.2.1 Why Joining Al-Alloys

A crucial factor for the application of new technologies is the costs. Especially for the substitution of metals by light-weight alloys beneath all technological properties, the economical aspects have to be considered. Knowing the costs for an existing structure with a certain material for different transport systems it is possible to estimate the cost saving S over the lifetime for the reduced fuel consumption due to the lower weight. For a typical this value S is approximately 9.4 Euro/kg, for an airplane 120 Euro/kg, and for a rocket 8000 Euro/kg (Schubert, Klassen, Zenner, Walz & Sepold, 2001).

The costs $C_{conv.}$ for typical structures in conventional design can be derived from the literature. For cars these costs are in the range between 14 Euro/kg for steel component and 55 Euro/kg for Al-structures. Typical costs for airplanes are between 42 Euro/kg (steel) and 155 Euro/kg (aluminum), whereas rockets reach “astronomic” prices between 6000 and 100000 Euro/kg.

$$\text{Using the equation: } C_{subst.} = \frac{S(1 - R) + C_{conv.}}{R}$$

with: S the cost saving over the lifetime due to reduced fuel consumption for light-weight structures; and: R weight ratio between conventional and new structure with material substitution (Schubert et al., 2001).

Depending on the preferential type of loading the structure has to withstand, typical R-values and therefore, typical allowable costs for economic material substitutions can be derived, see Table 2.4.

This clearly shows that even estimating with a very similar equation a priori considerations of allowable costs are possible and show good agreements with literature values, see e.g.

Table 2.4 Allowable costs $C_{subst.}$ for material substitution in the cars industry (Schubert et al., 2001)

R for preferential loading with	Car (saving S=9,4 Euro/kg)		
	ρ (density)	R_e (yield s.)	τ (stiffness)
Subst. St/Al _{wrought} T6	0,36	0,2	0,61
$C_{conv.}$	14	14	14
$C_{subst.}$	56	108	29
Subst. St/Mg AZ91	0,24	0,21	0,54
$C_{conv.}$	14	14	14
$C_{subst.}$	88	102	34
Subst. St/TiAl6V4	0,59	0,08	0,42
$C_{conv.}$	14	14	14
$C_{subst.}$	30	283	46
Subst. Al _{wrought} Mg T6/AZ91	0,67	1,04	0,88
$C_{conv.}$	55	42	29
$C_{subst.}$	87	-	34

As can be seen allowable costs $C_{subst.}$ for cars are in the range 29 Euro/kg (substitute steel by aluminum) and 46 Euro/kg (substitute steel by titanium). The economic window for automotive production can be very small, but using modern mass production techniques material substitute may be economical reasonable. The very high values for

aircraft and rocket structures give evidence that nearly every effort for weight reduction is economical worth-while (Schubert et al., 2001).

Weldability is an important factor affecting wide-spread application of a material. In the case that a production of a component is not possible by conventional production methods, the suitability of this material to welded construction, in other words, the readily and economically joining of this material by any welding process, may overcome this problem. This, in turn, allows a wide-spread application of materials in industrial use (Pakdil, Çam & Erim, 2004).

The use of aluminum is increasing within the welding fabrication industry. Manufacturers are often adopting this material, either through innovation, or through pressure applied by their end users. Aluminum's unique characteristics of being light weight, and having excellent corrosion resistance, high strength, high toughness, extreme temperature capability, versatility of extruding, and recycling capabilities make it one of today's favored choices of material for many engineers and designers for a variety of welding fabrication applications. Because of the increased use of aluminum as a manufacturing material, the conversion from steel to aluminum within the welding fabrication industry is becoming increasingly common (Anderson, 2004a).

Laser beam welding is predestined for joining fuselage structures thanks to low heat exposure of components, a narrow welding seam, a high process speed of 10 m/min in comparison to 0,1 m/min for riveting, and a high degree of automation potential (Leigh et al., 2002).

As a result, uses of aluminum alloys have become widespread when their high corrosion resistance, a high specific strength and cost/weight performance due to steel is taken into consideration. Therefore, there has been a large amount of research about the welding of aluminum alloys, nowadays.

2.2.2.2 Difficulties in Welding of Aluminum Alloys

The major difficulties generally encountered, during welding of aluminum alloys, are discussed in detail in the following sections.

2.2.2.2.1 Weld Cracking Cracking is classified as either solidification cracking or liquation cracking. Solidification cracking can occur in some aluminum alloys containing alloying additions of elements such as Mg, Si and Cu. Solidification cracking occurs when interdendritic liquid films are unable to support the stresses acting on them during solidification, and manifests itself as so-called ‘centre-line’ or ‘crater’ cracks originating from the middle of the fusion zone. Increasing the effective alloying content of the weld metal, and so decreasing its solidus temperature, helps to feed and heal these cracks with material that remains liquid to lower temperatures. This is usually accomplished by the addition of an appropriately alloyed filler wire, as outlined below, but solidification cracking can also be influenced by a number of other factors: Cracking will occur if the cooling rate immediately after welding is too high. This can be reduced by preheating, by decreasing welding speed or appropriate design of the welding pass sequence if multipass welding is to be used. Similarly, in laser beam welding, pulsed (as opposed to continuous) can be used to control solidification cracking, by controlling the cooling rate during solidification, as demonstrated by Matsunawa and co-workers. Appropriate joint design can minimize solidification shrinkage strains. Reducing or removing restraints on the joint also reduces the strain acting on the solidifying weld metal. Controlling the joint fit-up so as to reduce the gap over which the solidifying material has to ‘stretch’ also reduces the strain acting on the weld metal. Solidification cracking can be successfully avoided by the introduction of an appropriately alloyed filler wire, e.g. in 6xxx alloys a wire containing 5-12% of silicon (Si) can be added. Magnesium (Mg) alloyed filler wires can also reduce solidification cracking, and lead to superior weld metal strength and ductility after welding, but have been reported to lead to an increased incidence of liquation cracking in the HAZ. Factors determining the appropriate selection of filler wire to avoid solidification cracking are further detailed in.

The addition of grain refiner to the weld metal breaks up the dendritic solidification grain structure and promotes a more uniform equiaxed structure in the weld pool. This structure resists solidification cracking better. For this reason zirconium (Zr) is commonly added to 5183 filler wire. Research work has also been conducted into the effect of scandium (Sc) addition to filler wires, as Sc is a potential aluminum grain refiner. It is reported that ultrasonic can also have a similar 'break up' effect on the dendrites in the solidifying weld pool. Refinement of the weldment grain structure also increases its strength. Liquation cracking is distinct from solidification cracking in that it occurs in the HAZ immediately adjacent (within the width of a few grains) to the fusion zone. Liquation cracking can arise if the local solidus of the grain boundary phases in the parent material is below that of the solidus of the weld metal. If temperatures in this region exceed this local solidus, grain boundary melting occurs. Thus, liquation cracking is more likely to occur when using higher melting point filler, as then it is more likely that the weld metal solidus will be above that of the grain boundary phases in the parent material. Either way, on re-cooling, the thin films of liquid present on the grain boundaries will crack during solidification if these films cannot withstand the thermal stresses acting on them. Liquation cracking can be reduced by: i) reducing or removing restraints on the joint and ii) 'feeding' of the solidifying grain boundaries by molten material from the fusion zone. This requires that the melting point of the fusion zone is lowered. One example would be the use of a low melting point 4043 Al-5wt%Si or 4047 Al- 12wt%Si filler wire to weld crack-sensitive 6xxx Al-Mg-Si alloys (Allen 2004).

2.2.2.2.2 Weld Porosity Porosity is a problem common to all fusion welding processes. During the welding of aluminum alloys it arises principally from the entrapment of dissolved hydrogen (or shield) gas in the molten aluminum during welding. Hydrogen in solid aluminium has only $\sim 1/20$ th of the solubility that it has in liquid aluminum (See figure 2.18). Dissolved hydrogen comes out of solution therefore, during solidification to form porosity. Common sources of hydrogen are from the parent metal itself, from a hydrated oxide on that metal, or from hydrocarbon containing contaminants, such as grease and cutting oils, or moisture (Çam, Dos Santos & Koçak

1997). These can be present on the parent material or filler wire surfaces, or as contaminants in the shield gas(es).

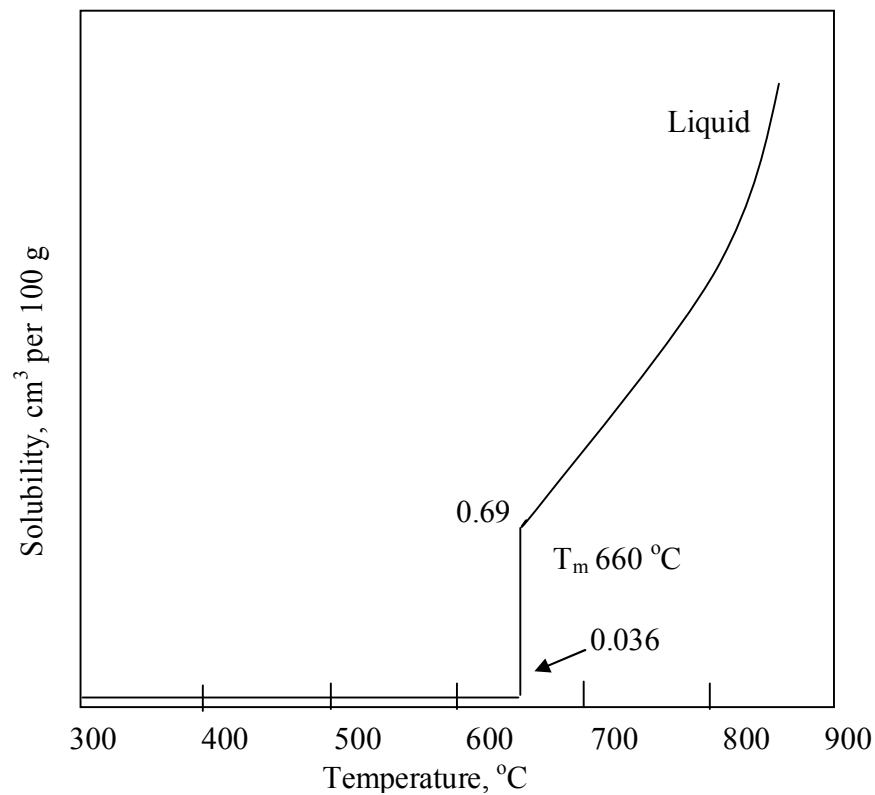


Figure 2.18 Hydrogen solubility in pure aluminum (Horn & Kent, 1967)

Porosity can therefore be reduced by:

Appropriate joint cleanliness: this can require degreasing with organic solvents, mechanical cleaning (e.g. wire brushing) to remove any adhered contaminants or (hydrated) surface oxides, or chemical cleaning using 10%NaOH solution (8) and rinsing (more suited to batch processes).

Avoidance of pick up of moisture and other contaminants from gas lines and welding equipment is also important. Purging the system prior to use is therefore recommended, as is the use of in line drying agents.

2.2.2.2.3 Loss of Strength Unlike in steels, welding acts to reduce the strength of many aluminum alloys, both work-hardened and age-hardened. For reference, Table 2.5 gives an overview of the tensile properties of a number of different aluminum alloys in the laser welded condition. Note that the data in Table 2.5 refers to laser-only butt welds, and no reference is made to any degree of solidification cracking that may have occurred in the welds. Loss of strength in work-hardened aluminum alloys occurs through recovery and recrystallisation (e.g. of 5xxx Al-Mg) leading to a loss of strength in the HAZ and the fusion zone. This is common to all fusion welding processes. Use of a high Mg filler wire can partly offset the loss in mechanical strength of the fusion zone, as the resultant solution hardening in the O tempered weld metal is then higher. Mg addition also adds some degree of natural or artificial ageing response if sufficient Si is present in the weld metal. The Mg in the filler wire also replaces that lost by vaporisation from the weld metal. The resulting strength of the Mg solution hardened and/or aged fusion zone can be higher than that of the (partially) recovered and recrystallised HAZ, explaining why in 5xxx Al-Mg welds made with Al-Mg filler, tensile failure can sometimes occur outside of the fusion zone. A finer grain size in the weld metal can also attribute some strengthening effect, and this can be promoted by increasing the solidification rate, by adding grain refiners such as Sc and Zr, or by appropriate design of the welding speed and sequence. Note that filler wire addition can do nothing to alter the mechanical properties of the HAZ, which by definition never mixes with the filler.. Strength loss in the HAZ of any aluminium alloy fusion weld can be reduced by decreasing the heat input in the weld, either through changing the weld pass sequence in multipass welding, or by increasing the welding speed. High speed laser welding is therefore advantageous (Allen 2004).

Table 2.5 Overview of as-welded strengths and ductilities for selected aluminium alloys, in selected thicknesses. All data are for laser-only butt welds. No data is provided for cracking, which can be poor in autogenous welds. (Allen 2004)

Alloy	Gauge (mm)	Joint efficiency*	Elongation**	Welding speed (m/min)	Wire	Wire feed speed (m/min)	Laser
1050	6	87	4,9	5,5	none	n/a	10kW CO ₂
1050	6	74	1,5	5	99,5AL-Ti	4	10kW CO ₂
1200	2	74	5,2	6	none	n/a	5kW CO ₂
1200	2	69	4,5	0,8	none	n/a	2kW Nd:
2219 T87	3,2	59	-	2,5	none	n/a	5kW CO ₂
2219 T87	3,2	58	-	1	2319	3	5kW CO ₂
2219	6,5	68	1,3	5,5	none	n/a	10kW CO ₂
2219	6,5	70	1,4	5	A4043	5	10kW CO ₂
5251	2	79	3	5,5	5154	2	5kW CO ₂
5251	2	79	14	1	none	n/a	2.6kW CO ₂
6023	1,5	96	-	8	A4043	3,5	3.5kW Nd:
6023	1,5	90	-	8	none	n/a	3.5kW Nd:
6061 T6	6	63	1,2	5	none	n/a	10kW CO ₂
6061 T6	6	79	1,9	5	A4043	5	10kW CO ₂
6082	2	94	-	6	A4043	3	3.5kW Nd:
6082	2	86	-	6	none	n/a	3.5kW Nd:

*=UTS (welded sample)/UTS parent. **elongation to failure. '-' indicates values not reported. Alloy temper indicated where reported.

Loss of strength in age hardened aluminum alloys arises from revolutionizing and/or overageing (coarsening) of hardening precipitates (e.g. 2xxx Al-Cu, 6xxx Al-Mg-Si and

7xxx Al-Zn-Mg), again reducing strength in the HAZ. This is common to all fusion welding processes. In age hardened aluminum alloys, strength in the HAZ, and in some cases in the weld metal, can be partially recovered by natural ageing after welding or a post-weld heat treatment. Post-weld heat treatment can be impractical for large welded structures, and can introduce large amounts of thermal distortion. (Allen 2004)

2.2.2.3 Laser Welding Issues with Aluminum Alloys

Laser welding provides an alternative to traditional joining processes (e.g. MIG welding) for the joining of aluminum alloys. For CO₂ laser keyhole welding of aluminum alloys, power densities of $4 \times 10^6 \text{W/cm}^2$ are necessary (10). This compares to a power density requirement of only $8,6 \times 10^5 \text{W/cm}^2$ for CO₂ laser welding of steel (28). The increased power density requirement is due to the higher reflectivity and thermal conductivity of aluminum alloys compared to steel (Allen 2004).

The net coupling between a Nd:YAG laser beam and aluminum is, however, better owing to its shorter wavelength. Consequently, the power density requirement for keyhole welding with a Nd:YAG laser is about half compared to a CO₂ laser (29), at around $1,5 \times 10^6 \text{W/cm}^2$ (10). For laser welding of aluminum alloys therefore, the increased flexibility and reduced power density requirements tend to offset the lower wall-plug efficiencies of Nd:YAG lasers compared to CO₂ lasers (Allen 2004).

Specific advantages relevant to the laser welding of aluminum alloys are (Allen 2004):

Keyhole welding of sections up to ~10mm in thickness.

Joining of dissimilar alloys, e.g. 5xxx to 6xxx.

The option to forego the use of filler wires (autogenous welds) in certain alloy systems, e.g. 5xxx. Thus there is no change of bulk chemistry between the fusion zone, HAZ, and parent material.

The focused nature of the laser beam leads to a narrow fusion zone and HAZ.

This improves the mechanical properties of the weld over those of other fusion welding techniques.

The rapid cooling in the fusion zone results in a finer grained, less segregated fusion zone microstructure than in arc welds.

The large depth to width ratio of the keyhole welds reduces solidification strains in the weld bead and can help to reduce solidification cracking. Aluminum alloys in the 6xxx, 2xxx and 7xxx series are particularly susceptible to solidification cracking when welded by conventional fusion techniques.

Specific disadvantages relevant to the laser welding aluminium alloys are (Allen 2004):

Unlike steels, the aluminium surface is highly reflective at the wavelengths of Nd:YAG and CO₂ lasers. The thermal conductivity of aluminium is also higher than steel. Consequently a higher power density is required for keyhole welding than for steels, e.g. (11). The surface reflectivity can, however, be reduced by anodising, or by the application of an absorptive coating, but this can lead to contamination and porosity.

With current laser power densities, laser welding is better suited to the joining of material with thicknesses <~10mm. Other techniques, such as electron beam welding or friction stir welding, are being developed to produce full thickness welds in aluminum alloys up to ~100mm thick.

Vaporization and hence de-alloying of certain constituents upon laser welding, e.g. Mg. Mg vaporization can also lead to porosity, particularly in laser welded 5xxx Al-Mg alloys. This can also occur however in arc fusion welds. Mg loss can be counteracted through use of high Mg content Al-Mg filler wires, e.g. 5356.

Macroporosity resulting from instabilities and periodic collapses of the keyhole during welding. These collapses can trap in bubbles of metal vapor which form in the root of the keyhole, or shield or atmospheric gases from above . This is particularly an issue in non-fully penetrating laser welds, when the porosity generating root of the weld pool is contained within the material, and it is more difficult for the pores to escape from the melt. Stable keyhole welding is achieved when the vapor pressure of the metal vapor/plasma is balanced by the surface tension acting at the melt/vapor or melt/plasma interface. This balance is dependant on welding and alloy parameters, the latter including liquid viscosity. Macroporosity due to keyhole instability can be reduced, however by use of a shaped pulsed laser, as demonstrated by Matsunawa and co-workers . Alternatively, twin spot or hybrid arc-laser welding can also be used to reduce macroporosity. In twin spot welding, two separate laser beams are incident on the material, but impinge on the same melt pool. In hybrid arc-laser welding, an arc and laser are separate but work in the same melt pool. Both techniques result in an elongated weld pool, which in turn aids the escape of entrapped bubbles of metal vapor, shield gas, and atmospheric gases, e.g. (Allen, 2004).

To give an overview of the current capabilities of lasers for keyhole welding of aluminum alloys, Figure 2.19 shows the CO₂ laser powers typically used and corresponding penetration depths achieved for a range of welding speeds. It summarises primarily continuous wave welding of autogenous butt joints or bead on plate runs. As Figure 2.19 shows, most work has concentrated on materials 6mm in thickness, using CO₂ laser powers up to 10kW. What should be noted is that this data covers a range of alloys, beam qualities, spot sizes and hence power densities, leading to a large scatter in

the data. Beam qualities and spot sizes are rarely reported, complicating the comparison of this data (Allen, 2004).

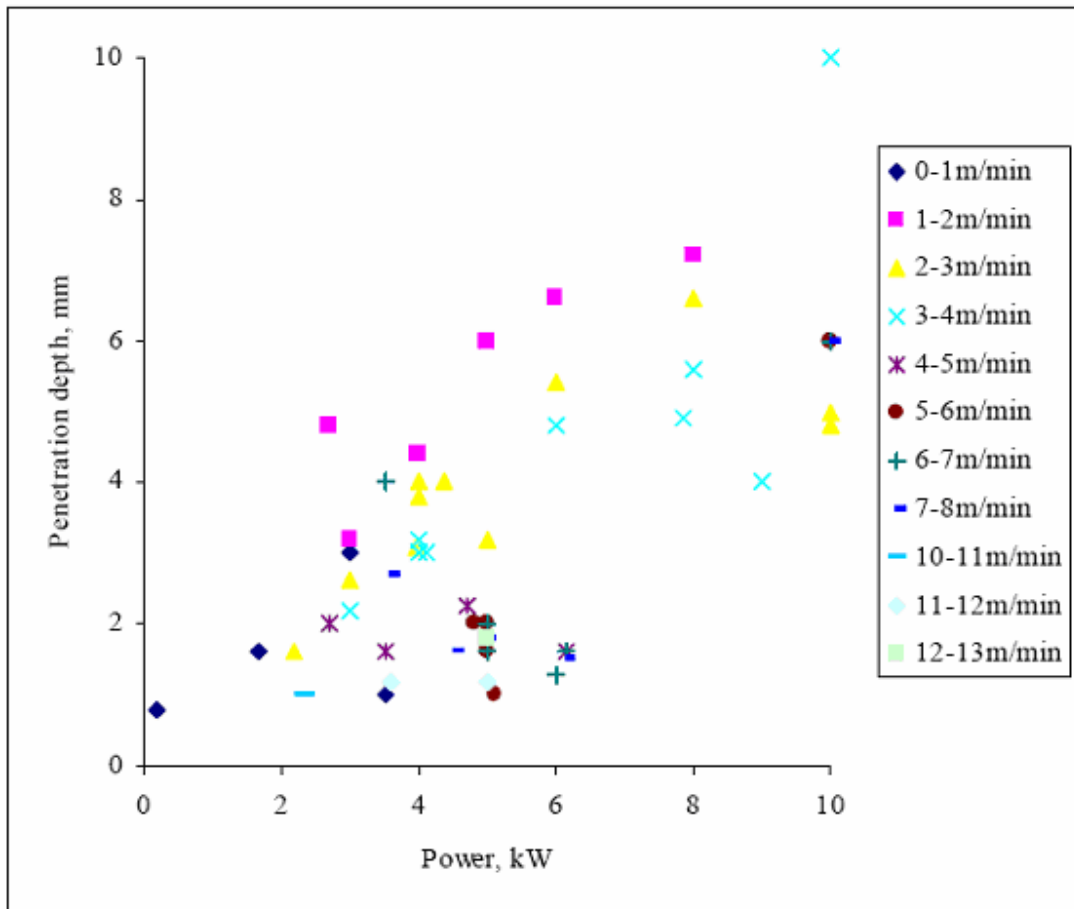


Figure 2.19 Penetration depth vs. cw CO₂ laser power for different welding speeds (Allen 2004)

Similarly, Figure 2.20 gives an indication of the Nd:YAG laser powers typically used and corresponding penetration depths achieved for a range of welding speeds. Again, it summarises primarily continuous wave welding of autogenous butt joints or bead on plate runs. Comparing Figure 2.19 to Figure 2.20 shows that far less work overall has been carried out using Nd:YAG lasers than CO₂ lasers. The Nd:YAG work done to date has concentrated on materials 4mm in thickness, using laser powers up to 6kW. Again,

this data covers a range of alloys, beam qualities, spot sizes and hence power densities, complicating the analysis (Allen 2004).

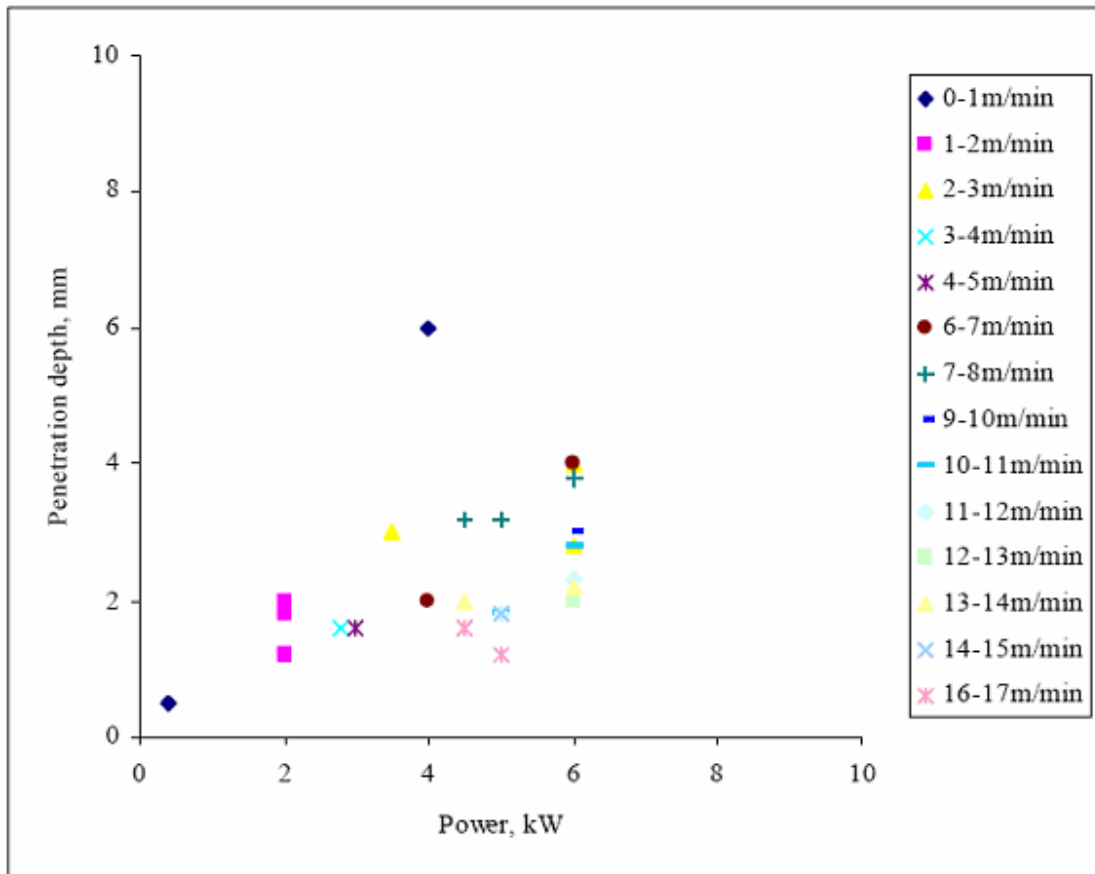


Figure 2.20 Penetration depth vs. cw Nd:YAG laser power for different welding speeds (Allen, 2004)

2.3 Fatigue

Fatigue is generally understood to be a process dominated by cyclic plastic deformation, such that fatigue damage can occur at stresses below the monotonic yield strength. The process of fatigue cracking generally begins from locations where there are discontinuities or where plastic strain accumulates preferentially in the form of slip bands. In most situations, fatigue failures initiate in regions of stress concentration such

as sharp notches, non-metallic inclusions, or at preexisting crack-like defects. Where failures occur at sharp notches or other stress raisers, cracks first initiate and then propagate to critical size, at which time sudden failure occurs. The fatigue life consists of crack initiation as well as crack propagation. On the other hand, when fatigue failures are caused by large inclusions or pre-existing crack-like defects, the entire life consists of crack propagation (Schijve, 1988).

The historical development of the present knowledge on fatigue crack initiation and fatigue crack growth is marked by a number of characteristic observations and analytical concepts.

All metals, as well as most other materials, subjected to repeated loadings are susceptible to progressive fatigue failures if the loadings are high enough. The phenomenon of repeated loadings causing the failure of metals was first noted by Albert in about 1829 and called fatigue by Poncelet in 1839. Some of the earliest fatigue tests were undertaken by Wöhler as a part of a study to eliminate the failures of railway car axles. Since then, much has been learned about the fatigue process through the study of fatigue failures and related experimentation (Anderson, 1995).

Fatigue data are customarily plotted on an S-N (Wöhler curve) diagram. Load P , stress S (σ), or strain ϵ measurement is plotted as the ordinate (vertical axis) and the life in cycles as the abscissa (horizontal axis). Two typical *S-N* curves obtained under load or stress control test conditions with smooth specimens are shown in Figure 2.21. Here S is the applied stress, usually taken as the alternating stress σ_a , and N is the number of cycles or life to failure, where failure is defined as fracture.

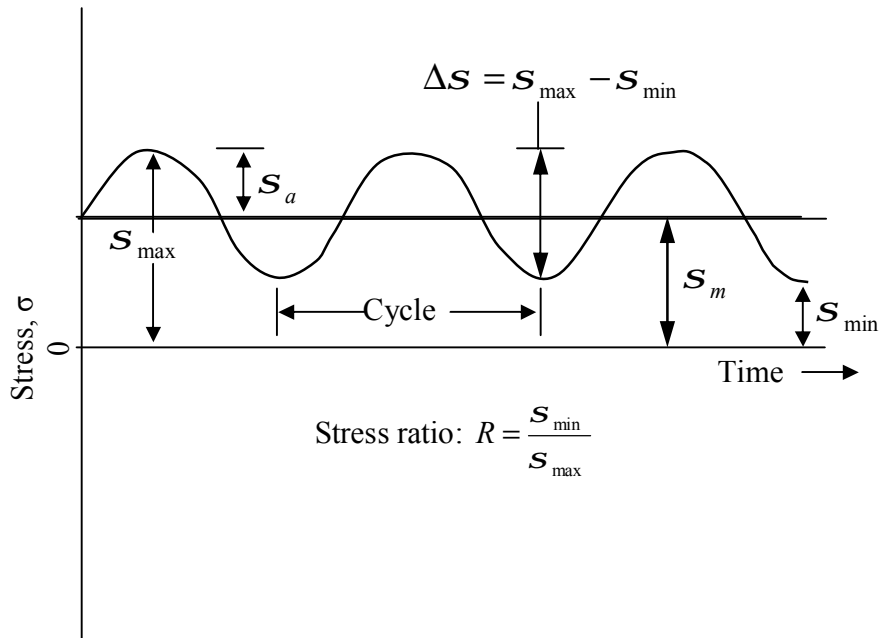


Figure 2.25 Nomenclature for constant amplitude cyclic loading (Fuchs & Stephens, 1980)

Nomenclature used in fatigue design has been superimposed on the constant amplitude stress versus time curve in Figure 2.25. Definitions of alternating, mean, maximum, minimum, and range of stress (strain or stress intensity factor) are indicated (Fuchs & Stephens, 1980). The algebraic relationships among these terms are:

$$\text{Mean stress: } s_m = \frac{s_{max} + s_{min}}{2}$$

$$\text{Stress range: } s_r = s_{max} - s_{min} \quad (2.1)$$

$$\text{Stress amplitude-(Variable component of stress): } s_a = \frac{s_r}{2} = \frac{s_{max} - s_{min}}{2}$$

The stress range is just twice the alternating stress. Tensile or compressive stresses or strains are taken algebraically as positive and negative, respectively. Alternating stress or strain is an absolute value. The two common stress ratios R and A used frequently in the fatigue literature are:

$$\text{Stress ratio: } R = \frac{S_{\min}}{S_{\max}} \quad A = \frac{S_a}{S_m} \quad (2.2)$$

Stresses in Eqs. 2.1 and 2.2 can be replaced with strain or stress intensity factors. One cycle is the smallest segment of the stress or strain versus time history which is repeated periodically, as shown in Figure 2.5. Under variable amplitude loading, the definition of one cycle is not clear and hence reversals of stress or strain are often considered. In constant amplitude loading, one cycle contains two reversals, while in variable amplitude loading a defined cycle may contain many reversals.

Constant amplitude S - N curves of this type are plotted on semilog or log-log coordinates and often contain fewer data points than shown. Figure 2.21 shows typical scatter. Figure 2.21a shows a continuous sloping curve, while Figure 2.21b shows a discontinuity or "knee" in the S - N curve. This knee has been found in only a few materials (notably the low strength steels) between 10^6 and 10^7 cycles under non-corrosive conditions. Most materials do not contain the "knee" even under carefully controlled environmental conditions. Under corrosive environments all S - N data invariably have a continuous sloping curve. When sufficient data are taken at several stress levels, S - N curves are usually drawn through median points and thus represent 50 percent expected failures. Common terms used with the S - N diagram are "fatigue life," "fatigue strength," and "fatigue limit." ASTM definitions of these terms are given below (Fuchs & Stephens, 1980).

S-N plots of constant-amplitude fatigue tests of material and joints such as those of Figure 2.21a-b often indicate the presence of an endurance limit or fatigue limit σ_y (Sharp, Nordmark & Menzemer, 1996).

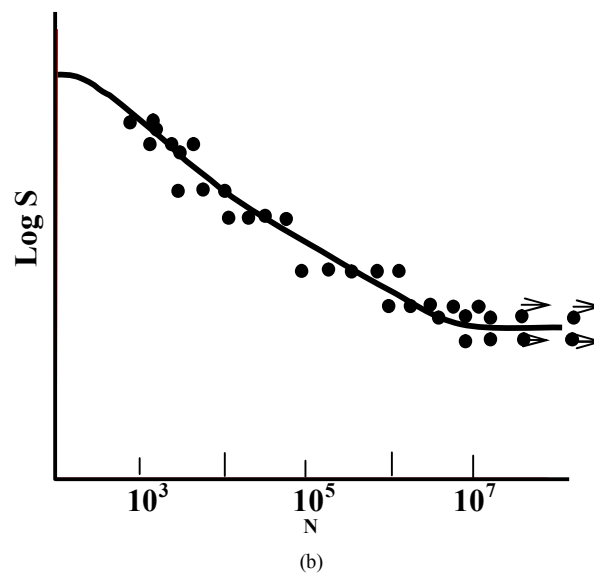
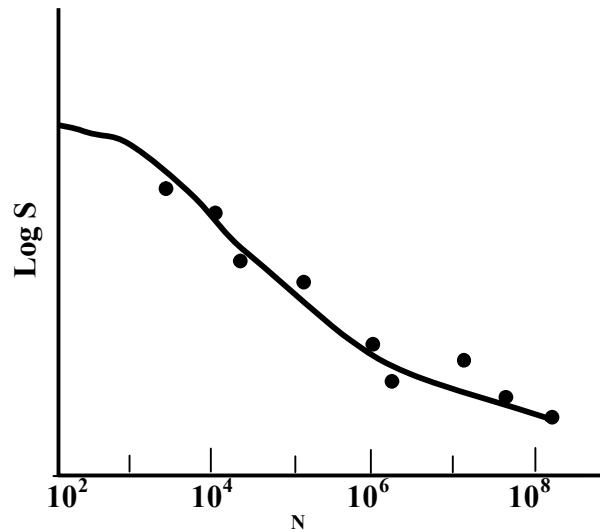


Figure 2.21 Typical S-N diagrams (a-b) (Wöhler curve) (Fuchs, 1980)

The first microscopic observations on early crack initiation were made by Ewing and Humphrey in 1903. For a long time the optical microscope was the only apparatus to

study fatigue crack growth. Later more detailed information could be obtained with the electron microscope (First TEM, now also SEM). Important fractographic studies could be made, and an outstanding feature was the discovery of striations, which indicated a cycle-by-cycle crack growth mechanism (Schijve, 1988).

Major contributions to the subject of fatigue in the 1950s included the introduction of closed-loop electro-hydraulic test systems, which allowed better simulation of load histories on specimens, components, and total mechanical systems. Electron microscopy opened new horizons to better understanding of basic fatigue mechanisms. Irwin introduced the stress intensity factor K_I , which has been accepted as the basis of linear elastic fracture mechanics (LEFM) and of fatigue crack growth life predictions (Fuchs and Stephens, 1980). The stress intensity factor, the application of the stress intensity factor K to fatigue crack growth under CA (constant-amplitude)-loading and to fracture toughness K_{Ic} is well established by now. The first paper on the correlation between the fatigue crack growth rate da/dN and ΔK was published by Erdoğan et al. in 1961 (Schijve, 1988). Fatigue-crack-propagation tests are conducted to provide data for the prediction of fatigue life. The data may be plotted in an a/N plot (Figure 2.22) where a , the crack length, is the depth of a surface crack or one-half the total length of a surface or internal crack. More useful information is obtained by determining the rate of fatigue-crack propagation da/dN as the test progresses. Figure 2.23 is schematic log-log plot of da/dN versus ΔK , which illustrates typical fatigue crack growth behavior in metals. The sigmoidal curve contains three distinct regions. At intermediate ΔK values, the curve is linear, but the crack growth rate deviates from the linear trend at high and low ΔK levels. In the former case, the crack growth rate accelerates as K_{max} approaches K_{crit} , the fracture toughness of the material (Anderson, 1995).

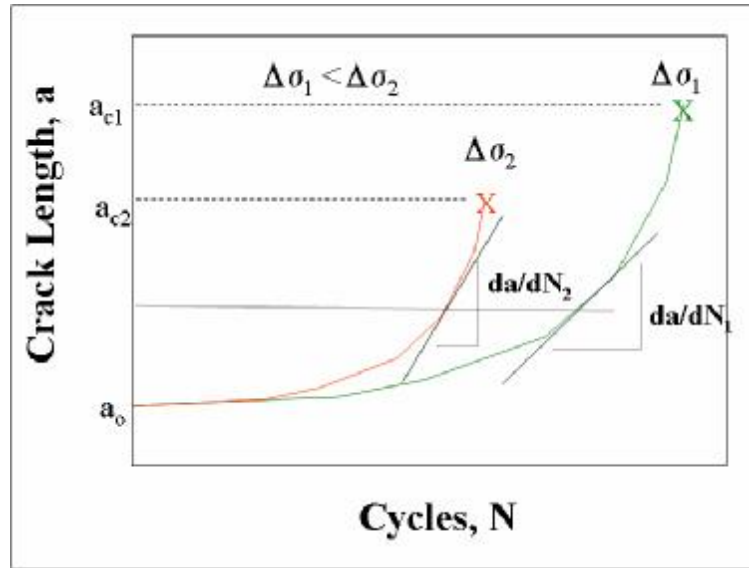


Figure 2.22 Fatigue crack length versus applied cycles (Fracture is indicated by x) (Schijve, 1988).

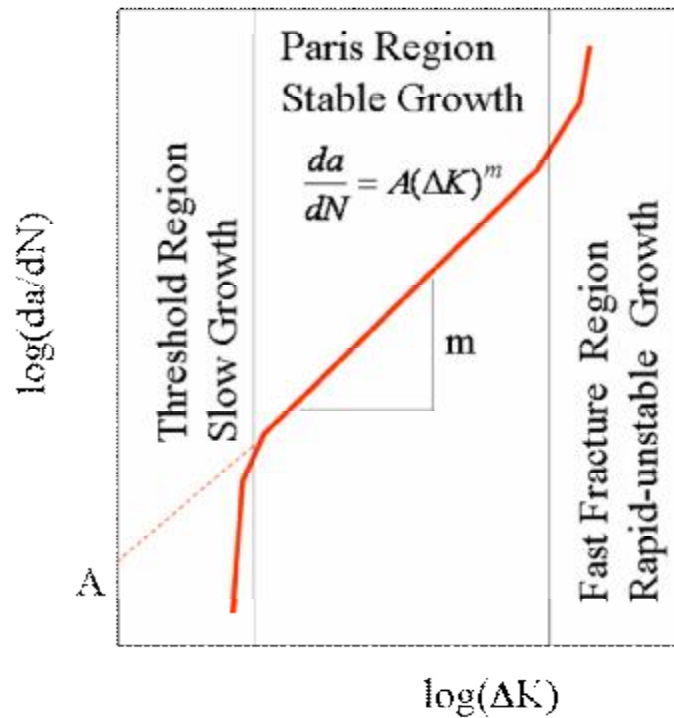


Figure 2.23 Schematic sigmoidal behavior of fatigue crack growth rate versus stress intensity factor range (Schijve, 1988).

Crack closure under cyclic tension was discovered by Elber in 1970. He proved the occurrence of plastic deformation in the wake of a growing fatigue crack by measuring non-linear crack opening behavior. It is surprising that the concept of crack closure under nominal tensile stress cycles was not recognized earlier. The situation now has drastically changed. It appears that no fatigue crack problem can be explained without considering crack closure. In the mean time, other mechanisms for crack closure have been proposed, such as surface roughness, oxidation, and crack bridging. It is noteworthy that previously Endo et al. in 1969 explained a lower crack growth rate in rotating beam steel specimens tested in salt water by referring to “wedge action caused by the metal oxide in cracks, which reduced the strain amplitude at the crack tip” (Schijve, 1988).

2.3.1 The three modes of loading

The three basic modes of loading, which can cause crack growth, as shown in Figure 2.24, are:

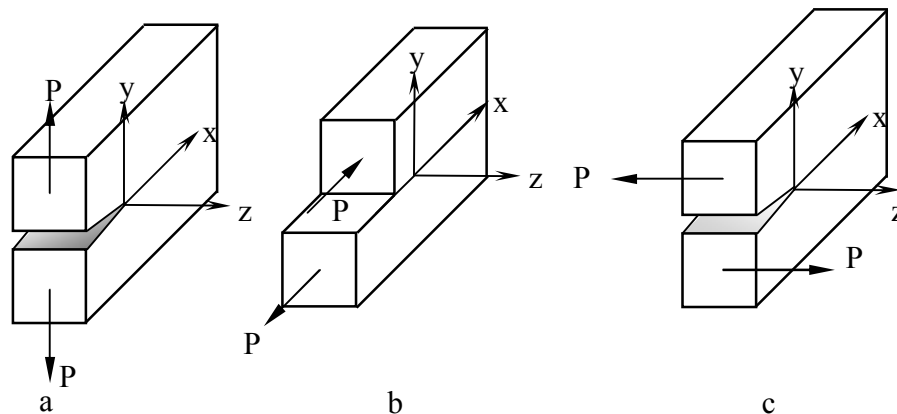


Figure 2.24 Three modes of loading a) Mode I, b) Mode II, c) Mode III (Anderson, 1995)

Mode I : The opening mode; where crack faces move directly apart.

Mode II. : In-plane shear mode; where the crack surfaces move normal to the crack front and remain in the crack plane.

Mode III. : Out-of-plane shear mode; where the crack surfaces move parallel to the crack front and remain in the crack plane (Anderson, 1995).

2.3.2 Micro Mechanisms of Fatigue

Metals are crystalline in nature, which means atoms are arranged in an ordered manner. Most structural metals are polycrystalline and thus consist of a large number of individual ordered crystals or grains. Each grain has its own particular mechanical properties, ordering direction, and directional properties.

Some grains are oriented such that planes of easy slip or glide are in the direction of the maximum applied shear stress. Slip occurs in ductile metals within individual grains by dislocations moving along crystallographic planes. This creates an appearance of one or more planes within a grain sliding relative to each other. Slip occurs under both monotonic and cyclic loading.

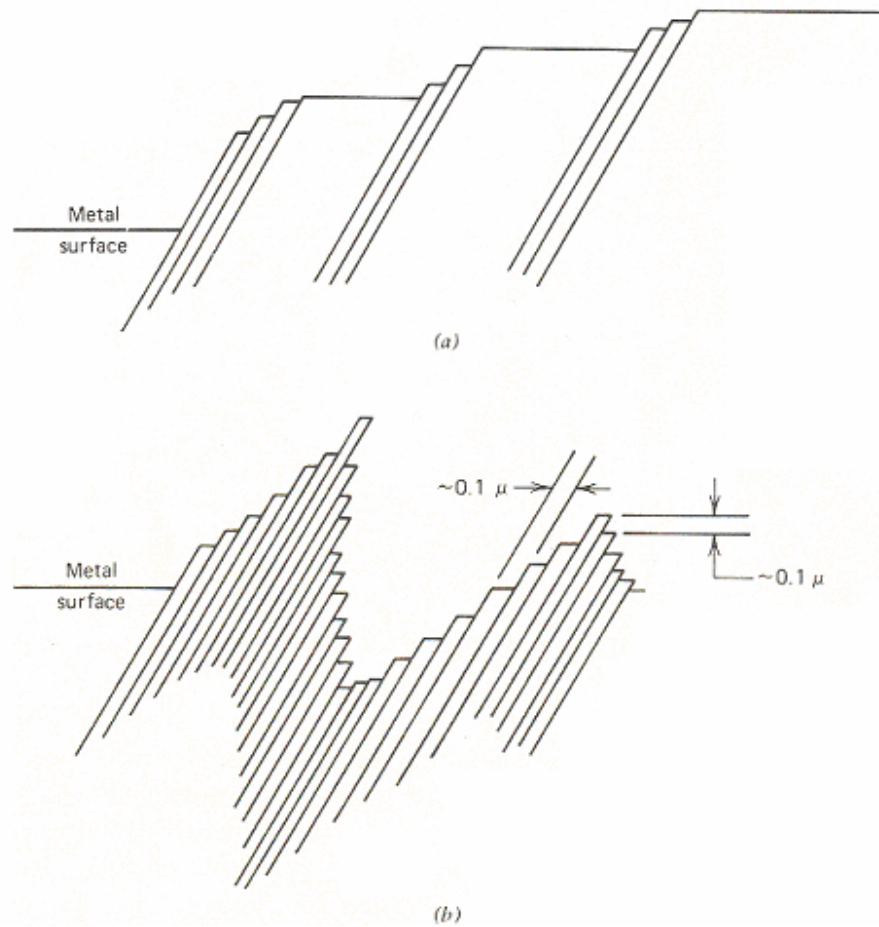


Figure 2.26 Slip in ductile metals due to external loads a) Static (steady stress)
b) Cyclic stress (Fuchs & Stephens, 1980)

Figure 2.26a shows an edge view of coarse slip normally associated with monotonic and high stress amplitude cyclic loading. Under lower stress amplitude cyclic loading fine slip occurs as shown in Figure 2.26b. Coarse slip can be considered as an avalanche of fine movements. Slip lines shown in Figure 2.26 appear as parallel lines or bands within a grain when viewed perpendicular to the free surface. Both fine and coarse slip are studied with pre-polished, etched specimens using optical and electron microscopy techniques (Fuchs & Stephens, 1980).

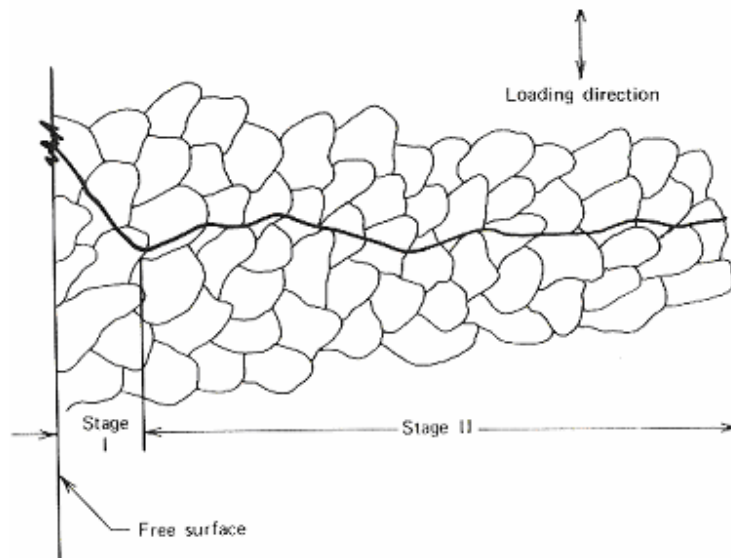


Figure 2.27 Schematic of stages I and II transcrystalline microscopic fatigue crack growth (Fuchs & Stephens, 1980)

Fracture under alternating fatigue stresses may be described roughly in terms of the mechanisms for two distinct stages:

a) Initiation: Fatigue cracks are initiated on the surfaces by the formation of “intrusions” in “persistent” slip-bands in pure metals, and at internal defects such as inclusions in commercial materials. Microcracks may coalesce at an angle of about 45° to the tensile axis (Stage I growth).

b) Propagation: The propagation of the fatigue crack, particularly under high strain amplitudes, give rise to the striations characteristic of fatigue failure. Such striations may be formed by shear on alternating planes radiating out from the crack tip (stage II growth). It has been established that one striation is generally formed during each fatigue cycle (Fuchs and Stephens, 1980).

Mechanisms of fracture can be generally separated into two categories:

1. Brittle; where, on the scale of observation the extent of inelastic deformation is small, and
2. Ductile, where, on the scale of observation, the extent of plastic flow is appreciable.

Brittle fracture is discussed above on the atomic basis. The other extreme is the rupture separation by viscous or plastic flow until the cross section vanishes. Figure 2.28 schematically illustrates three of the most common fracture mechanisms in metals and alloys (Anderson, 1995).

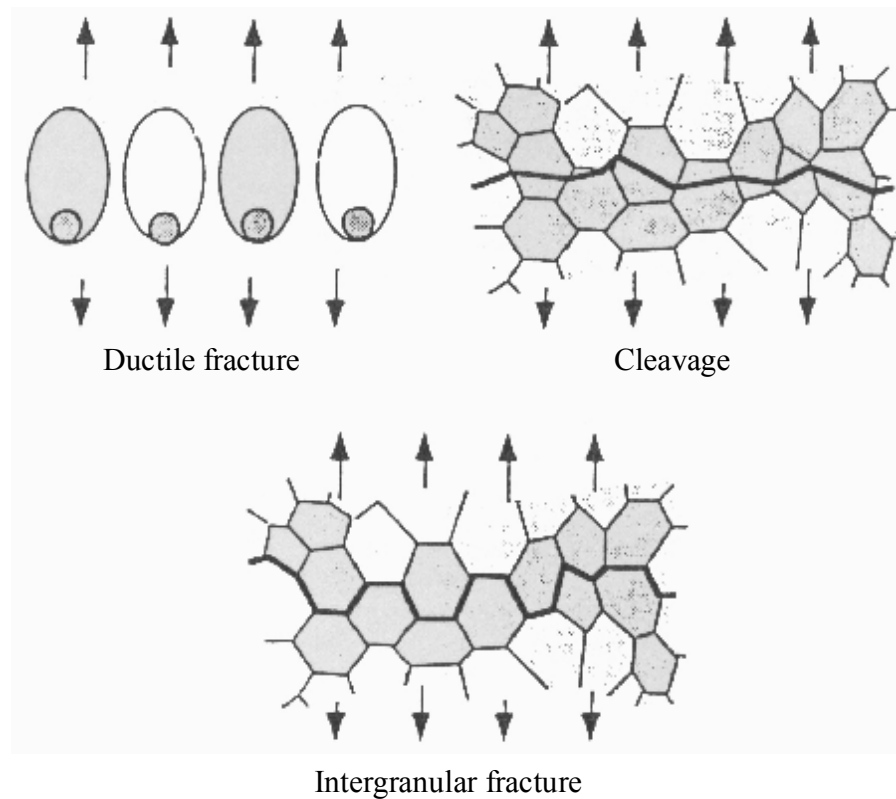


Figure 2.28 Three micro-mechanisms of fracture in metals (Anderson, 1995)

Ductile fracture involves nucleation, growth and coalescence of microscopic voids that initiate at inclusions and second phase particles. Cleavage fracture involves separation along specific crystallographic planes (cleavage planes), where the fracture path is transgranular. Although cleavage is often called brittle fracture, it can be preceded by large scale plasticity and ductile crack growth. Intergranular fracture occurs when the grain boundaries are the preferred fracture path in the material. In most cases metals do not fail along grain boundaries. Ductile metals usually fail by coalescence of voids formed at inclusions and second phase particles, while brittle metals typically fail by transgranular cleavage. Under special circumstances, however, cracks can form and propagate along grain boundaries (Anderson, 1995).

2.3.3 Crack Tip Plastic Zone Size

Whether a fracture occurs in a ductile or brittle manner, or a fatigue crack grows under cyclic loading, the local plasticity at the crack tip controls both fracture and crack growth. It is possible to calculate a plastic zone size at the crack tip as a function of stress intensity factor, K , and yield strength, σ_y , by using the stress eq. 2.3 and the von Mises or maximum shear stress yield criteria.

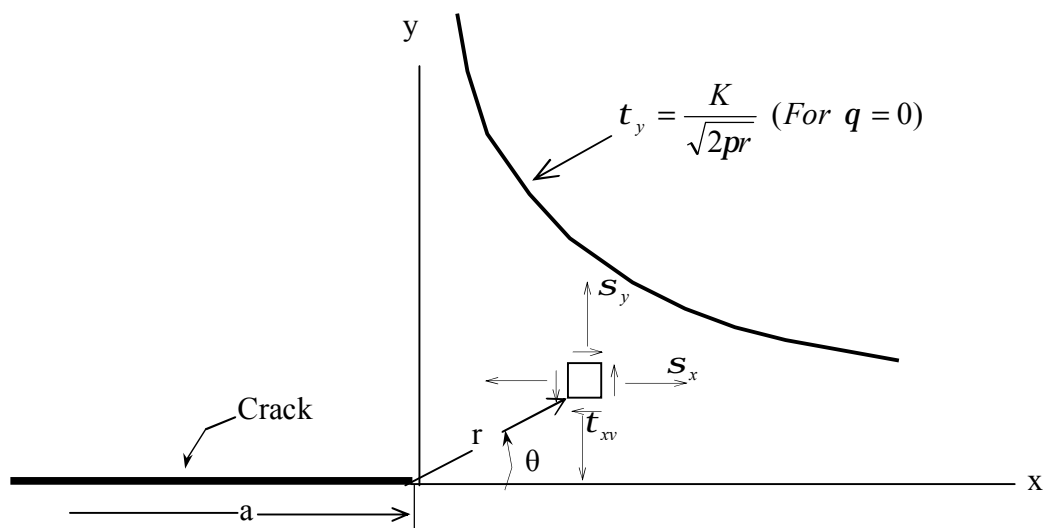


Fig. 4.4 Elastic stresses near the crack tip ($r \ll a$) (Fuchs & Stephens, 1980)

$$s_y = \frac{K}{\sqrt{2pr}} \cos \frac{q}{2} \left[1 + \sin \frac{q}{2} \sin 3 \frac{q}{2} \right]$$

$$s_x = \frac{K}{\sqrt{2pr}} \cos \frac{q}{2} \left[1 - \sin \frac{q}{2} \sin 3 \frac{q}{2} \right]$$

$$t_{xy} = \frac{K}{\sqrt{2pr}} \cos \frac{q}{2} \sin \frac{q}{2} \cos 3 \frac{q}{2}$$

$$s_z = t_{xz} = t_{yz} = 0 \quad \text{for plane stress}$$

$$\left. \begin{array}{l} s_z = m[s_x + s_y] \\ t_{xz} = t_{yz} = 0 \end{array} \right\} \text{for plane strain} \quad (2.3)$$

The resultant monotonic plastic zone shape for mode I using the von Mises criterion is shown schematically in Figure 2.30. For plane stress conditions, a much larger plastic zone exists compared to plane strain conditions, as indicated in the lower right corner. This is due to σ_z having a different value for plane stress than for plane strain as given in Figure 2.29, which decreases the magnitude of two of the three principal shear stresses. If we assume that a through thickness crack exists in a thick plate, then, the plate's free surfaces will have zero normal and shear stresses, and therefore the free surfaces must be in a plane stress condition. However, the interior region of the plate near the crack tip is closer to plane strain conditions as a result of elastic constraint away from the crack. Thus, the plastic zone along the crack tip varies similarly to that shown schematically in Figure 2.30. The actual stress-strain distribution within the

plastic zone is difficult to obtain; however, this is not significant for the use of linear elastic fracture mechanics in design (Fuchs & Stephens, 1980).

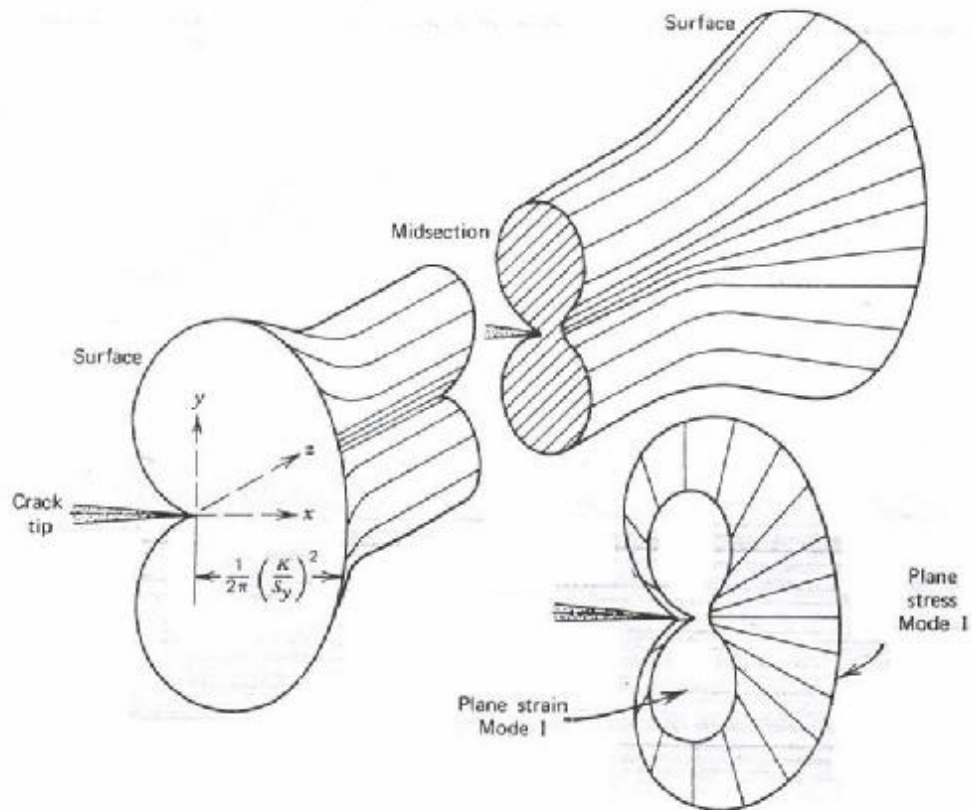


Figure 2.30 Plastic zone size at the tip of a through thickness crack (Fuchs & Stephens, 1980).

It is seen in Figure 2.30 that the plastic zone is proportional to the square of the ratio of the stress intensity factor to the yield strength. Because of plastic relaxation of the stress field in the plastic zone, the actual plane stress plastic zone size is approximately twice the value shown in Figure 2.30. The plane strain plastic zone size in the plane of the crack is usually taken as one-third the plane stress value. Thus, under monotonic loading, the plane stress plastic zone size, $2r_y$, at the crack tip, in the plane of the crack, is:

$$2r_y = 2 \left[\frac{1}{2p} \left(\frac{K}{s_y} \right)^2 \right] = \frac{1}{p} \left(\frac{K}{s_y} \right)^2 \quad (2.4)$$

and for plane strain:

$$2r_y \approx \frac{1}{3p} \left(\frac{K}{s_y} \right)^2 \quad (2.5)$$

Additional models for plastic zone size and shape, which have also received wide spread use, have been formulated by Dugdale, Hahn and Rosenfield. Under cyclic loading, a reversed plastic zone occurs when the tensile load is removed. Rice showed that it is much smaller than the peak monotonic values given by Eq. 2.4 or 2.5. For example, the size of the reversed plastic zone after unloading to zero load is only one-quarter of that which existed at the peak tensile load. Then the stresses in the plastic zone are compressive, while outside the plastic zone they change from compression to tension. Fatigue load sequence effects are caused by these plastic zones containing compressive or tensile stresses (Fuchs & Stephens, 1980).

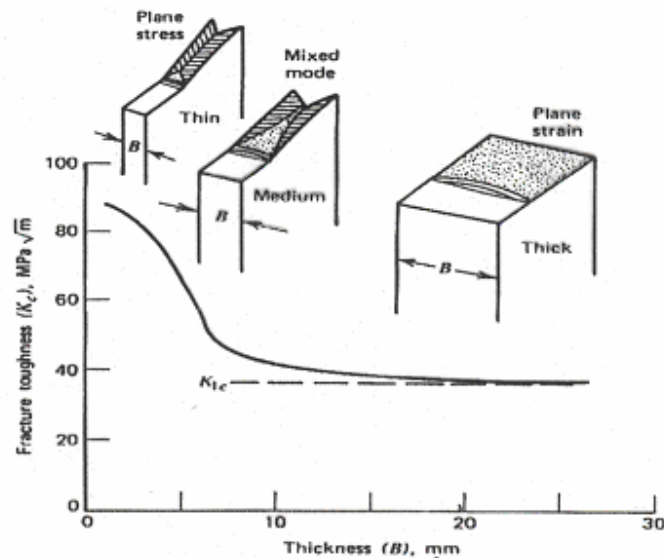


Figure 2.31 Effect of specimen thickness on fracture toughness (Fuchs & Stephens, 1980)

The general relationship between fracture toughness, K_c , and thickness is shown in Figure 2.31. The fracture appearance accompanying the different thicknesses is also shown schematically for single-edge notch specimens. The beach markings at the crack tip represent fatigue pre-cracking at low cyclic stress intensity factor range to assure a sharp crack tip. The fracture toughness values would be higher for dull, or notch type, crack fronts. It is seen that thin parts have a high value of K_c accompanied by appreciable "shear lips" or slant fracture. As the thickness is increased, the percentage of "shear lips" or slant fracture decreases, as does K_c . This type of fracture appearance is called mixed mode. For thick parts, essentially the entire fracture surface is flat and K_c approaches an asymptotic minimum value. Further increase in thickness does not decrease the fracture toughness, nor does it alter the fracture appearance. The minimum value of fracture toughness is called the "plane strain fracture toughness" K_{Ic} . The subscript I refers to the fact that these fractures occur almost entirely by mode I crack opening (Fuchs & Stephens, 1980).

The term "plane strain" is incorporated here since flat fractures best approach a true plane strain constraint throughout most of the crack tip region. For thin sections where appreciable "shear lips" occur, the crack tip region most closely experiences a plane stress situation. Thus, plastic zone sizes at fracture are much larger in thin parts as compared to thick parts. Plane strain fracture toughness K_{Ic} (*I*) is considered a true material property because it is independent of thickness. Approximate thickness required for steels and aluminums to obtain valid K_{Ic} values are given in Table 2.6. Low strength, ductile materials are subject to plane strain fracture at room temperature only if they are very thick. Therefore, most K_{Ic} data have been obtained for the medium and higher strength materials or for the lower strength materials at low temperatures (Fuchs & Stephens, 1980).

Table 2.6 Approximate thickness required for valid K_{Ic} tests (Fuchs & Stephens, 1980)

Thickness (mm)	Steel σ_y (MPa)	Aluminium σ_y (MPa)
76<	690	275
76	1030	345
45	1380	448
19	1720	550
6	2070	620

2.3.5 Fatigue Design Criteria

The four design philosophies discussed below have been developed over the years, and each is still applicable for specific structures and components.

2.3.5.1 Infinite-Life Design

If all stresses are below the endurance limit, failure should never occur. This criterion is an appropriate method for designing structures such as some rotating parts. For an infinite-life design, the fatigue design stresses are based on the maximum normal operating stresses (Fuchs & Stephens, 1980).

2.3.5.2 Safe-Life Design

Infinite-life design was appropriate for the railroad axles that Wöhler investigated, but automobile designers learned to use parts that, if tested at the maximum expected stress or load, would last only some hundred thousands of cycles instead of many millions. The maximum load or stress in a suspension spring or in a reverse gear may never occur during the life of a car; designing for a finite life under such loads is quite satisfactory. The practice of designing for a finite life is known as "safe-life" design. It is used in many other industries too, for instance, in pressure vessel design and in jet engine design (Fuchs & Stephens, 1980).

The safe life must of course include a margin for the scatter of fatigue results and for other unknown factors. The calculations may be based on stress-life relations, strain-life relations, or crack growth relations.

Ball bearings and roller bearings are noteworthy examples of safe-life design. The ratings for such bearings are often given in terms of a reference load that 90 percent of all bearings are expected to withstand for a given lifetime, for instance, 3000 hours at 500 rpm or 90 million revolutions. For different loads or lives or for different probabilities of failure the bearing manufacturers list conversion formulas. They do not list any load for infinite life, nor for zero probability of failure at any life.

2.3.5.3 Fail-Safe Design

A design philosophy, developed in the aircraft industry, assumes that the structure's construction is such that limited cracking or even failure of a given component would not produce a complete or catastrophic failure of the structure. This condition is most easily attained by the use of redundancy. A fail-safe condition can also be attained by having multiple load paths. The aircraft industry commonly uses structural details in wings or fuselages which serve as crack stoppers and prevent cracks from growing to a dangerous length between their scheduled inspections. A fail-safe design generally requires information about the fracture toughness and crack-propagation characteristics of the material (Fuchs & Stephens, 1980).

2.3.5.4 Damage-Tolerant Design

The aircraft industry has taken the fail-safe concept further by assuming that crack-initiation time is zero. In other words, they assume that a manufacturing flaw exists at a critical section. The principle is shown schematically in Figure 2.32. The initial flaw size is the longest length that cannot be reliably detected by their inspection method. A schedule of

periodic inspections is set up, depending in part on a fracture analysis of how large the crack can grow before it would cause a rapid fracture.

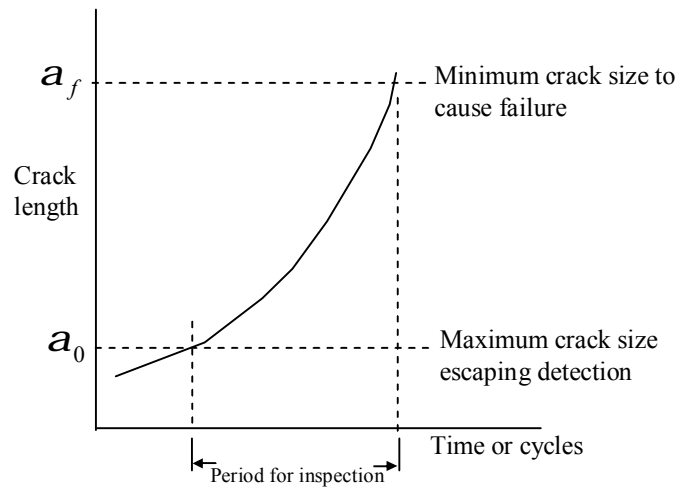


Figure 2.32 Damage-tolerance approach to design (Fuchs & Stephens, 1980)

2.3.5.5 Life Prediction for Crack Propagation

The total life (N) of a component is. number of cycles to initiate crack (N_i) + number of cycles to propagate crack (N_p) (Dogan, 1995).

Design against fatigue failure is based on either:

i) total life N ; stress/strain life approach

or

ii) propagation life N_p ; defect - tolerant approach.

i) Stress - Strain Life Approach (Local Strain Approach): is based on stress ($\Delta\sigma$) or strain ($\Delta\varepsilon$) to give finite life N , where N is the number of cycles to both initiate and propagate crack i.e. $N = f(\sigma \text{ or } \varepsilon)$

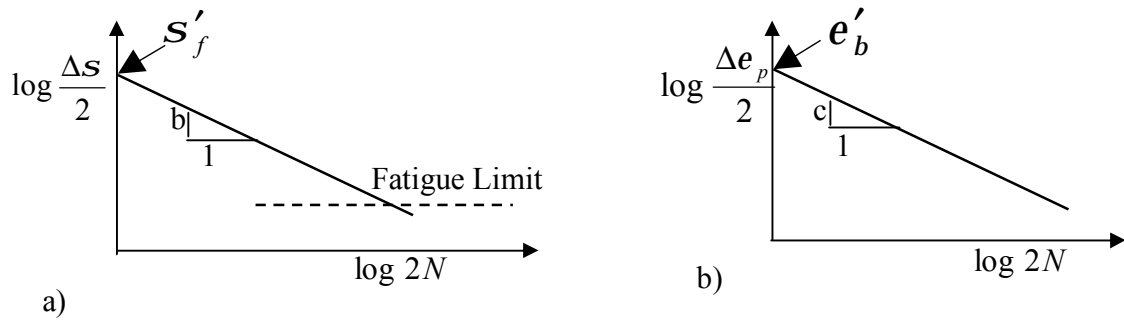


Figure 2.33. Schematic stress-strain life approach based on a) stress ($\Delta\sigma$) b) strain($\Delta\varepsilon$) (Dogan, 1995).

The empirical laws:

a) Basquin law:
$$\frac{\Delta S}{2} = S'_f (2N)^b \quad (2.6)$$

b) Coffin - Manson law:
$$\frac{\Delta e}{2} = e'_f (2N)^c \quad (2.7)$$

The approach requires corrections for such factors as

- a) Mean stress (Goodman relationship)
- b) Notches (stress concentration factors, Neubers law)
- c) Environment.

The approach is utilised extensively for non-safety critical applications, such as machine parts, washing machines, automobiles etc.

ii) Defect - Tolerant Approach: is based on number of cycles to propagate (N_p) the longest undetected crack to failure. The linear elastic fracture mechanics is utilised to describe fatigue crack propagation which is shown in Figure 2.34

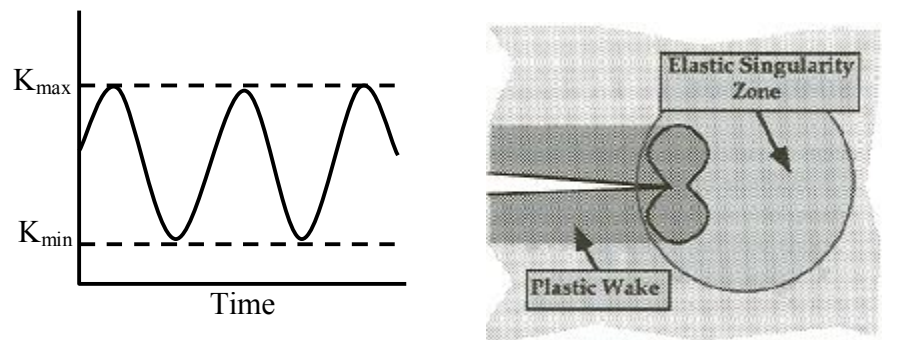


Figure 2.34 Constant amplitude fatigue crack growth under small scale yielding conditions (Anderson, 1995)

Crack-growth-propagate data may be represented by

$$\frac{da}{dN} = C_i \Delta K^{m_i} \quad (2.8)$$

$$\frac{da}{dN} = f(\Delta K, K_{\max}, R, f, \text{environment}, \text{etc}) \quad (2.9)$$

where a = crack size

N = number of cycles

da/dN = crack-growth rate

DK = stress-intensity range

f = frequency

C_i and m_i = the scaling constants

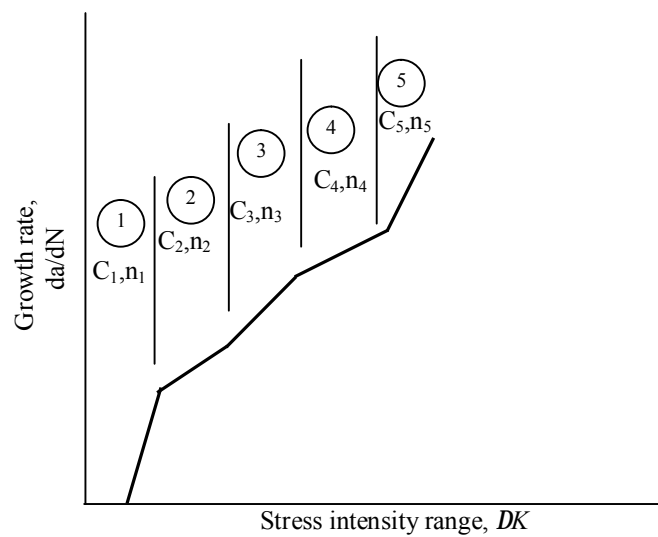


Figure 2.35 Straight-line approximation of fatigue crack growth behavior (Fuchs & Stephens, 1980).

Aluminum will often show several links in the da/dN — DK relationship, and thus will require a set of constants for each straight-line segment. This is illustrated in Figure 2.35. The expression given in Eq. (2.8) may be rearranged as follows:

$$N = \int_{a_i}^{a_f} \frac{da}{C_i \Delta K^{m_i}} \quad (2.10)$$

Where a_i = initial crack size

a_f = final crack size

In cases where DK is a simple function of crack length, the expression may be integrated directly. Where the stress-intensity solution is more complex, numerical integration is required. Further, an S-N curve may be developed for a specific combination of initial crack length and geometric conditions by simply varying the nominal stress.

$$\Delta K = K_{\max} - K_{\min} = K_{\max} (1 - R), \quad \Delta K = \frac{\Delta P}{B\sqrt{W}} f\left(\frac{a}{w}\right) \quad (2.11)$$

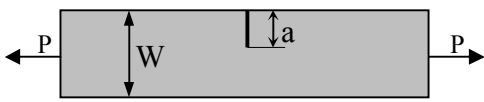
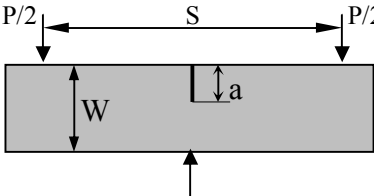
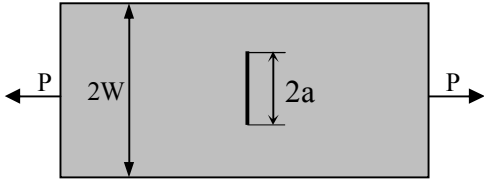
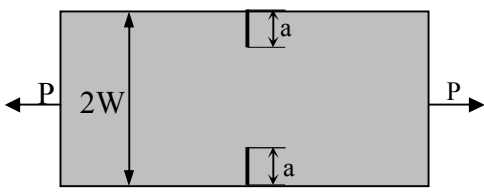
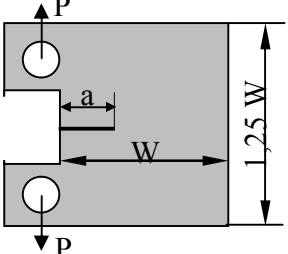
While plane stress strain fracture toughness is calculated, $f(a/W)$ to be required is selected from ASTM norms (see table 2.7)

$$K_{\max} = f(s_{\max} \sqrt{pa}) \quad (2.12)$$

$$R \text{ is the load ratio, } R = K_{\min} / K_{\max} \quad (2.13)$$

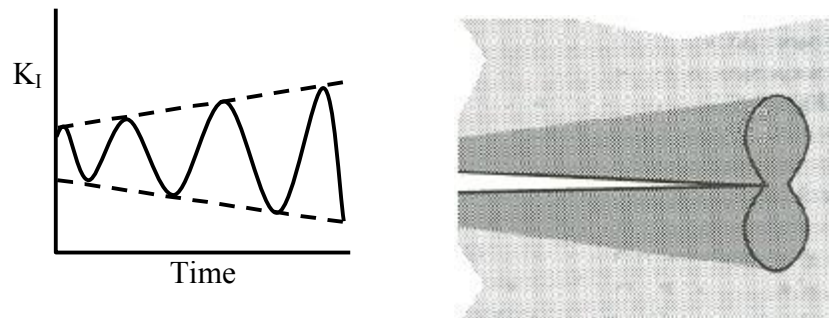
The life time is determined by integrating crack growth law (i.e. Eq.2.8) from assumed initial defect size to final failure. Since Paris et. al. demonstrated the application of fracture mechanics to characterise crack growth by fatigue, the approach is utilised in safety - critical applications, such as aircraft, aerospace and nuclear industries (Anderson, 1995).

Table 2.2. $f(a/w)$ values at ASTM (Anderson, 1995)

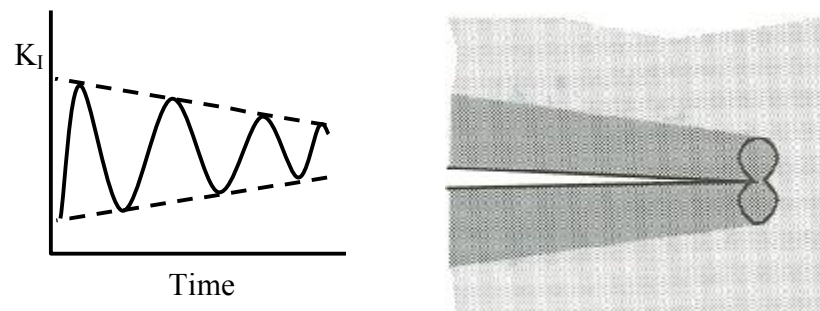
Geometry	F(a/W)
Single edge notched tension (SENT) panel 	$\frac{\sqrt{2 \tan \frac{pa}{2W}}}{\cos \frac{pa}{2W}} \left[0,752 + 2,02 \left(\frac{a}{W} \right) + 0,37 \left(1 - \sin \frac{pa}{2W} \right)^3 \right]$
Single edge notched bend specimen (SENB) 	$\frac{3 \frac{S}{W} \sqrt{\frac{a}{W}}}{2 \left(1 + 2 \frac{a}{W} \right) \left(1 - \frac{a}{W} \right)^{3/2}} \left[1,99 - \frac{a}{W} \left(1 - \frac{a}{W} \right) \left\{ 2,15 - 3,93 \left(\frac{a}{W} \right) + 2,7 \left(\frac{a}{W} \right)^2 \right\} \right]$
Middle tension (MT) panel 	$\sqrt{\frac{pa}{4W}} \sec \frac{pa}{2W} \left[1 - 0,025 \left(\frac{a}{W} \right)^2 + 0,06 \left(\frac{a}{W} \right)^4 \right]$
Double edge notched tension (DENT) panel 	$\frac{\sqrt{\frac{pa}{2W}}}{\sqrt{1 - \frac{a}{W}}} \left[1,122 - 0,561 \left(\frac{a}{W} \right) - 0,205 \left(\frac{a}{W} \right)^2 + 0,471 \left(\frac{a}{W} \right)^3 + 0,190 \left(\frac{a}{W} \right)^4 \right]$
Compact tension specimen (CT) 	$\frac{2 + \frac{a}{W}}{\left(1 - \frac{a}{W} \right)^{3/2}} \left[0,886 + 4,64 \left(\frac{a}{W} \right) - 13,32 \left(\frac{a}{W} \right)^2 + 14,72 \left(\frac{a}{W} \right)^3 - 5,60 \left(\frac{a}{W} \right)^4 \right]$

The procedures for analysing constant amplitude fatigue under small scale yielding conditions are fairly well established, although a number of uncertainties remain.

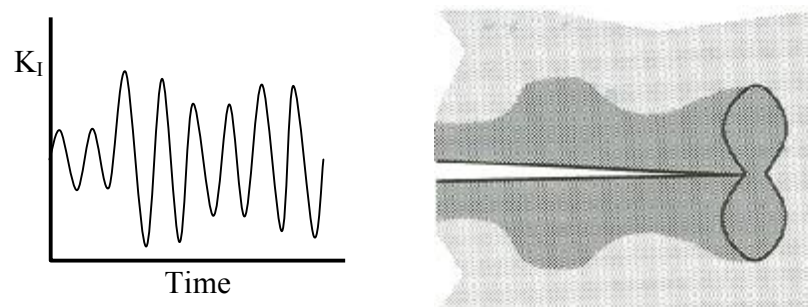
Variable amplitude loading, large scale plasticity and short cracks introduce additional complications that are not fully understood. Figure 2.36 illustrates several examples where the unique definition of the crack tip conditions by single loading parameter (the concept of similitude) is invalid. (Anderson, 1995).



(a) K_I increasing



(b) K_I decreasing



(c) Random

Figure 2.36 Examples of cyclic loading that violate similitude (Anderson, 1995)

In each case, prior loading history influences the current conditions at the crack tip

CHAPTER THREE

EXPERIMENTAL PROCEDURE

3.1 Material

In this study, Al 6056 (AA6056) alloy in T6 post-weld heat treatment condition has been used in the experiments. Pechiney-patented 6056 alloy is an Al-Si-Mg-Zn-Cu-Mn alloy, developed to provide weldable thin extrusions with an excellent compromise on high strength and corrosion resistance. (Leigh, 2002) The delivery treatment is T4511, and two metallurgical tempers are proposed after welding for the thin extrusions, peak aged -T6511 and overaged – intergranular corrosion insensitive T78511, conferring on 6056 superior combinations of weldability, high strength and corrosion resistance attractive for a wide variety of aerospace applications.

The aim of the ongoing research and development work on the new metallic fuselage is to achieve significant cost and weight savings in comparison to conventional aluminium–rivet constructions (Lenczowski, 2002) Thanks to its lower density, 6056 (density 2,72 g/cm³) alloy offers a 2,5% weight advantage over 2024 (density 2,78 g/cm³) alloy.

6056-T6/-T78 sheet and thin plate are particularly suited for fuselage panels, especially when weldability and corrosion resistance are the key design characteristics. 6056-T78 material can be recommended in a bare version, due to its resistance to intergranular corrosion. Use of sheets and thin plates in conjunction with 6056 extruded stringers is also recommended.

Precipitation hardening (age hardening) heat treatments are designed to produce a uniform dispersion of fine hard coherent precipitate in a softer and more ductile matrix (Horn & Kent,1967). There are three steps in an age hardening heat treatment:

- Step 1: Solution treatment
- Step 2: Quenching

- Step 3: Aging.

During solution treatment, the alloy is heated to a temperature to dissolve any second phase particles and to produce a homogeneous single-phase solution. After solution treatment, the material is then quenched (i.e., rapidly cooled). The atoms do not have time to diffuse to potential nucleation sites resulting in a supersaturated solution. Finally the supersaturated solid solution is heated to a temperature below the solvus and held for some time (i.e., artificial aging). At this lower temperature, atoms are able to diffuse short distances and precipitates will form at selected nucleation sites. The precipitates which form are coherent in arresting dislocation movement thus increasing the material's strength. Some alloys even continue to age at room temperature (i.e., natural aging) (Marsico & Kossowsky, 1989).

Post weld heat treatment graphic of AA 6056 from T4 to T6 is given in Figure 3.1.

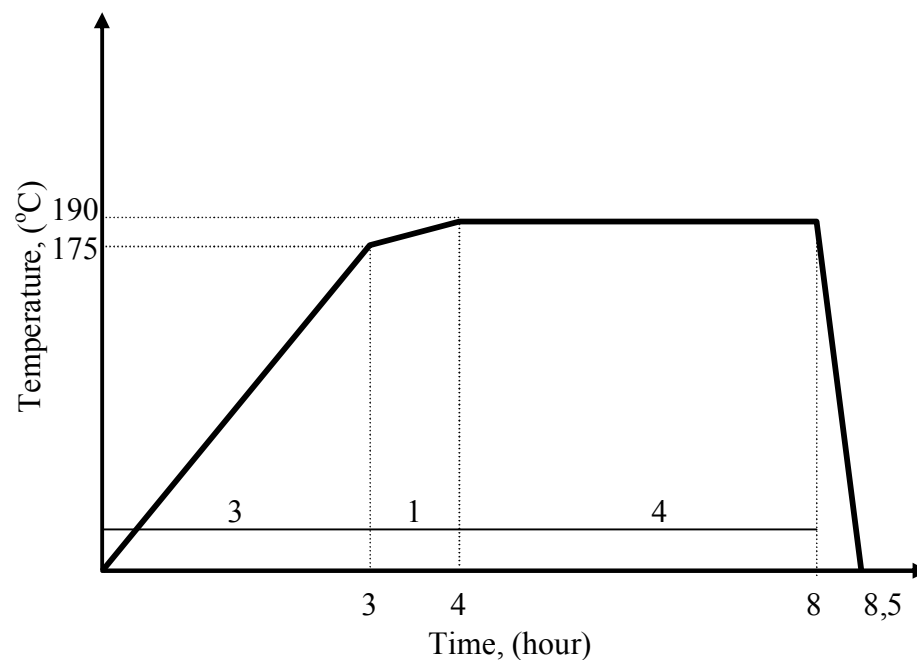


Figure 3.1 Heat treatment application conditions from T4 to T6 (Anonymous, 2004)

6056 aluminium alloy sheets of 6 mm thickness to which T6 thermal process was applied were joined with AlSi 12 wire filler using CO₂ laser beam welding. The chemical compositions of 6056-T6 sheet and wire filler are shown in Table 3.1.

Table 3.1. Chemical compositions of AA6056 and wire filler

Element (%)	AA 6056	AlSi12
Si	0,7-1,30	11,00-13,00
Fe	≤0,50	≤0,50
Cu	0,50-1,10	≤0,05
Mg	0,40-1,00	≤0,05
Mn	0,60-1,20	≤0,15
Cr	≤0,25	---
Zn	0,10-0,70	≤0,10
Ti	Ti+Zr ≤0,20	≤0,05
Be	---	≤0,008

Plates have been butt-welded parallel to their rolling directions using a 6,9 kW CO₂ laser with a welding speed of 3 m/s. The filler wire used is AlSi12 (Ø 1,2 mm).

Weld line has been investigated using X-ray radiography, scanning electron microscope (SEM), and optic microscope before applying mechanical tests to sheets which were welded. Mechanical characteristics of 6056 series aluminium sheets were determined and fatigue crack propagation (FCP) values were measured.

3.2 Microstructure

Material microstructure was examined under optical microscope and scanning electron microscope (SEM). Base metal, fusion zone (FZ) and heat-affected zones (HAZ) were inspected in detail.

3.3 Microhardness

Shimadzu HMV-2000 model Microhardness measurement machine is used in the hardness measurements. Vicker's microhardness profiles were measured at a load of 200 g with an indentation spacing of 0,3 mm. Microhardness profiles were formed at three locations, namely top, middle, and bottom of the joints:

Top: 1 mm from the crown

Middle: 3 mm from the crown and the root, and

Bottom: 1 mm from the root.

Each location has about 170 measurement points across the fusion zone.

3.4 Tensile Tests

Transverse tensile and microflat tensile specimens were prepared to determine the general and local mechanical characteristics of material.

3.4.1 Micro-tensile Test

Micro-tensile specimens extracted according to the cutting plan illustrated in Figure 3.2, were tested to determine the mechanical characteristics of the three different areas, namely the BM, fusion zone and the heat affected zone. This technique was developed at GKSS Research Center for facilitating the determination of local mechanical property changes in materials, especially in narrow high power beam welds (Koçak, Çam, Riekehr, Torster & Dos Santes, 1998). The micro-flat tensile specimen cutting plane is shown in Figure 3.3 and test mechanism in Figure 3.4. The micro-flat tensile tests were conducted at a rate of 0,4 mm/sec.

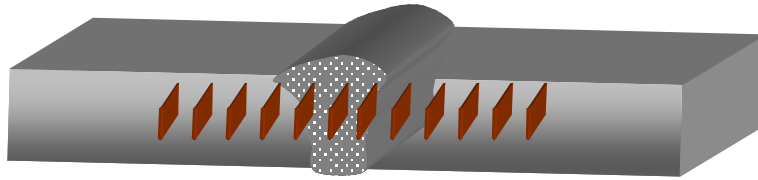


Figure 3.2 Micro-flat tensile specimen cutting plane

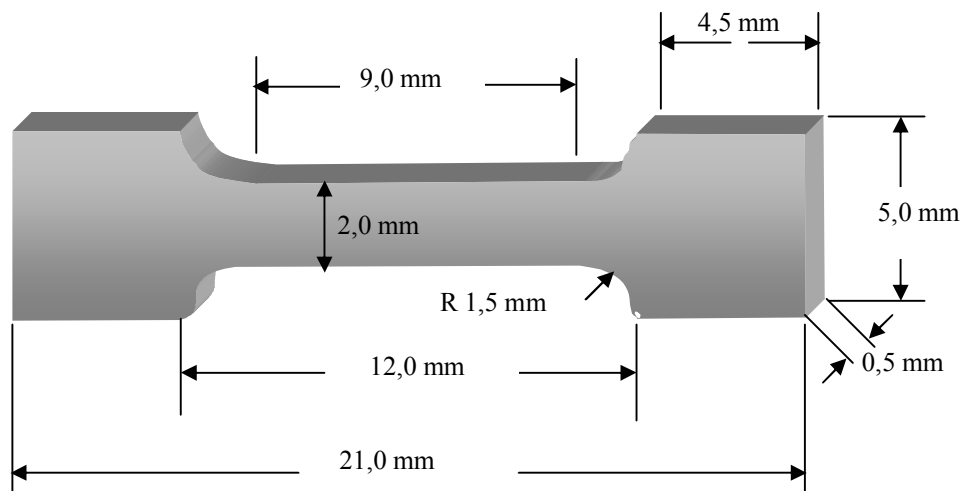


Figure 3.3 Micro-flat tensile specimen dimensions

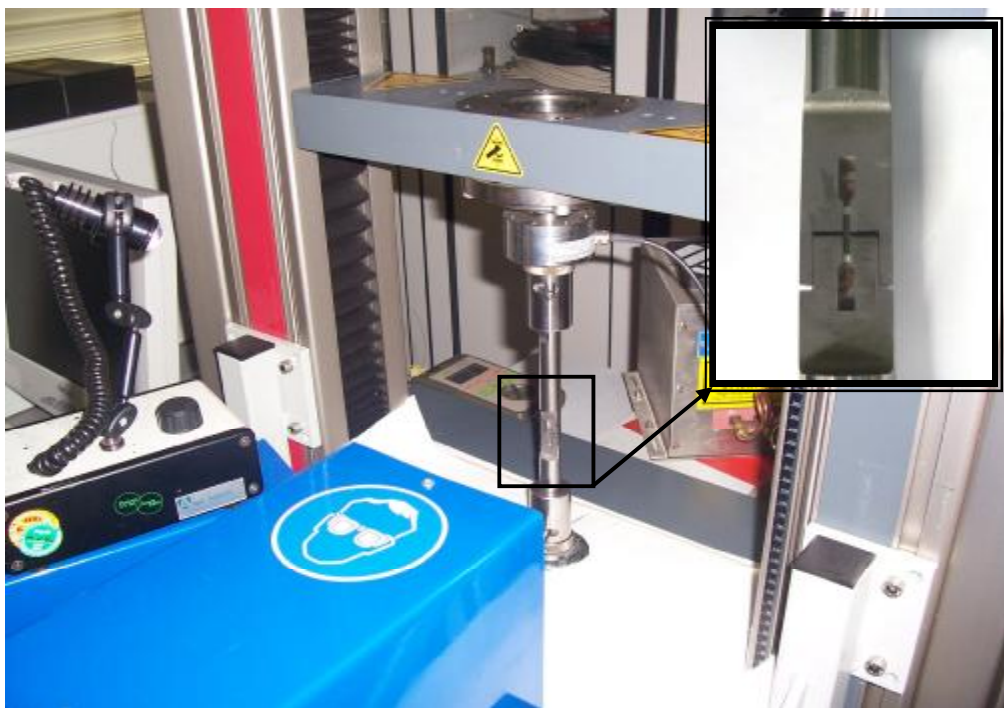


Figure 3.4 Micro-flat tensile testing machine and its detail

3.4.2 Transverse Tensile Test

Standard transverse tensile specimens at dimensions illustrated in Figure 3.5 were prepared according to DIN EN 895 norms and in LT-TL base metal and TL-welded directions.

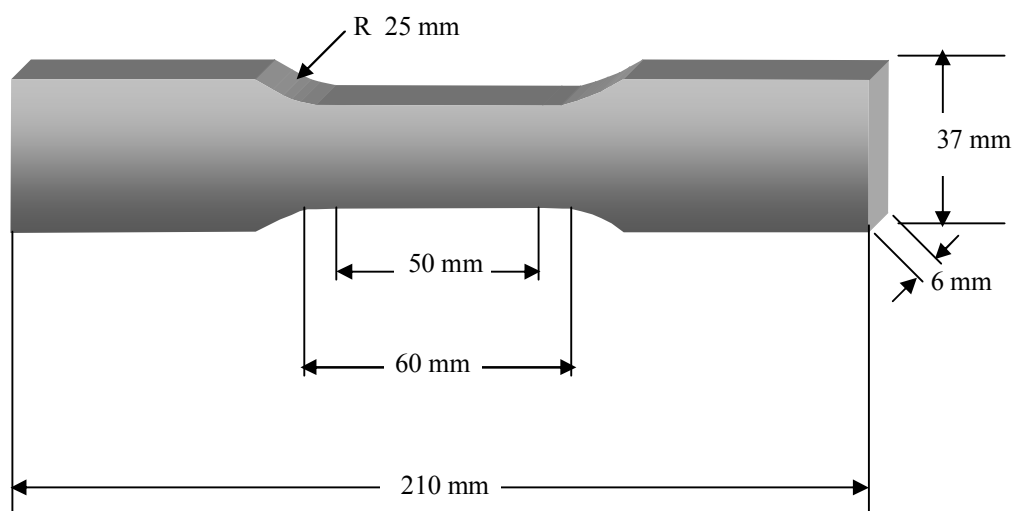


Figure 3.5 Standard flat tensile specimen dimensions

3.5 Fatigue Crack Propagation (FCP) Test

FCP tests have been carried out in in Schenk servo-hydraulic ($\pm 25\text{kN}$) machine using C(T) 100-type compact tension specimens. C(T) 100-type specimens for FCP testing, together with transverse tensile specimens have been extracted from 500 mm x 500 mm plates as shown in Figs. 3.6 and 3.7.

The specimens prepared are given codes in LT-TL directions in accordance with ASTM 399, as shown in Fig. 3.8.

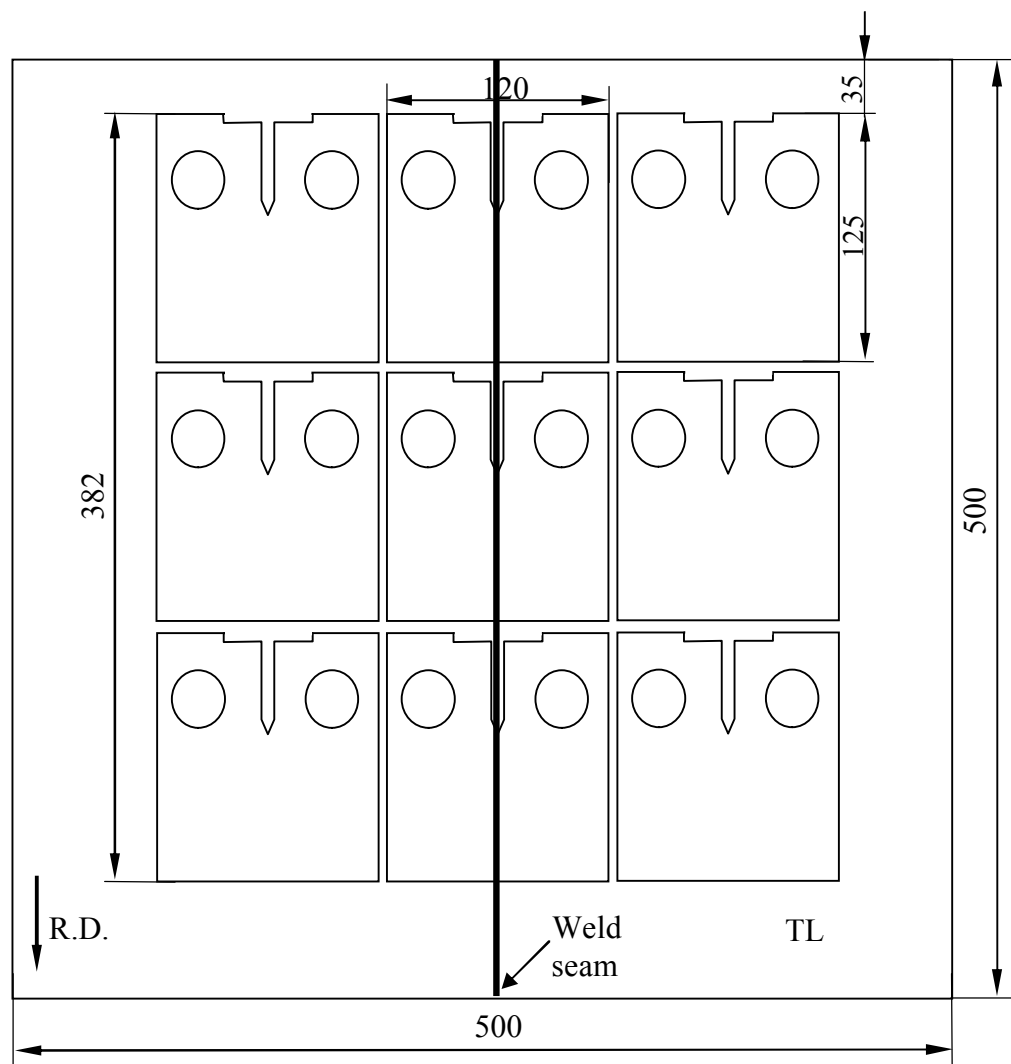


Figure 3.6 TL-C(T)100 specimens cutting plane

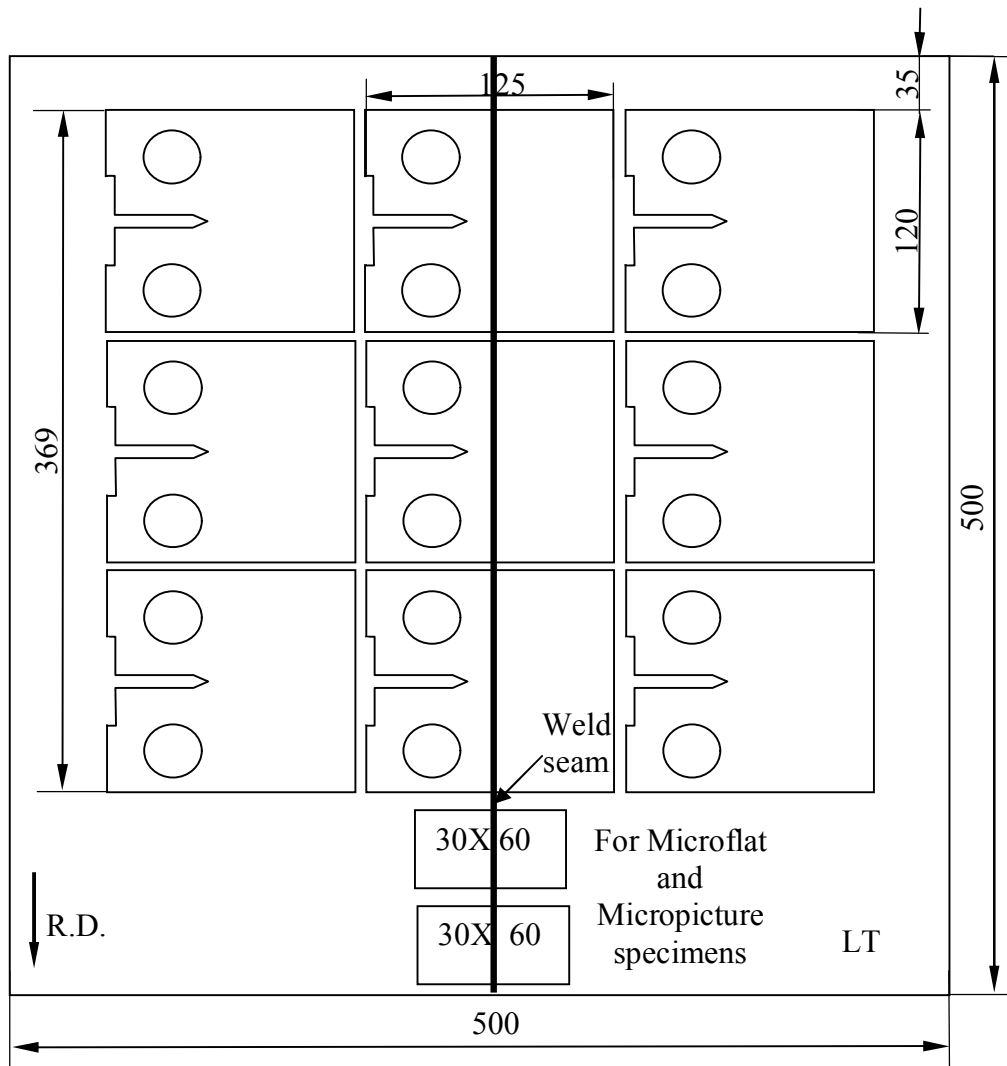


Figure 3.7 LT-C(T)100, microflat, and micropicture specimens cutting plane

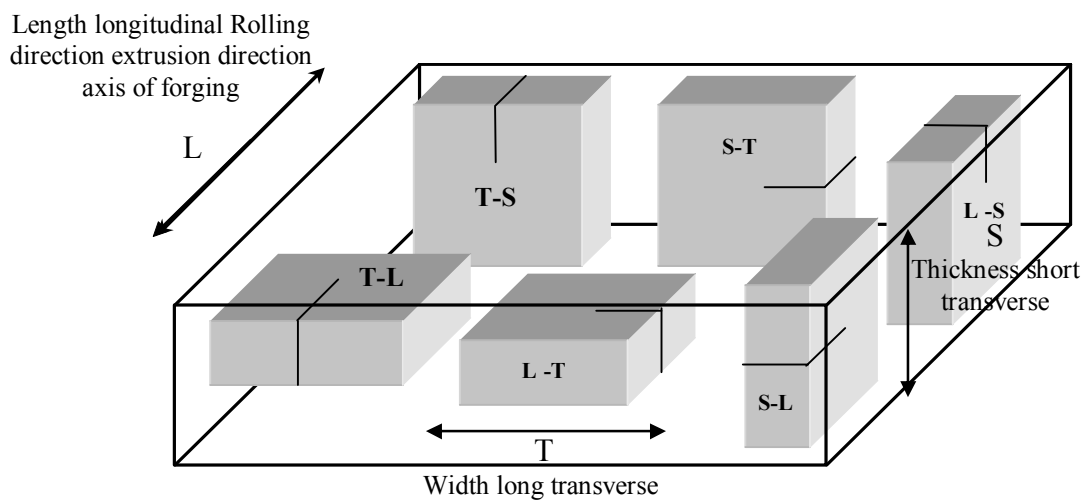


Figure 3.8 ASTM standard codes of CT-samples (ASTM399).

The specimens have gone through a series of processes as can be seen in Figures 3.9a to 3.9e, and finally they were polished with diamond pastry prior to testing..

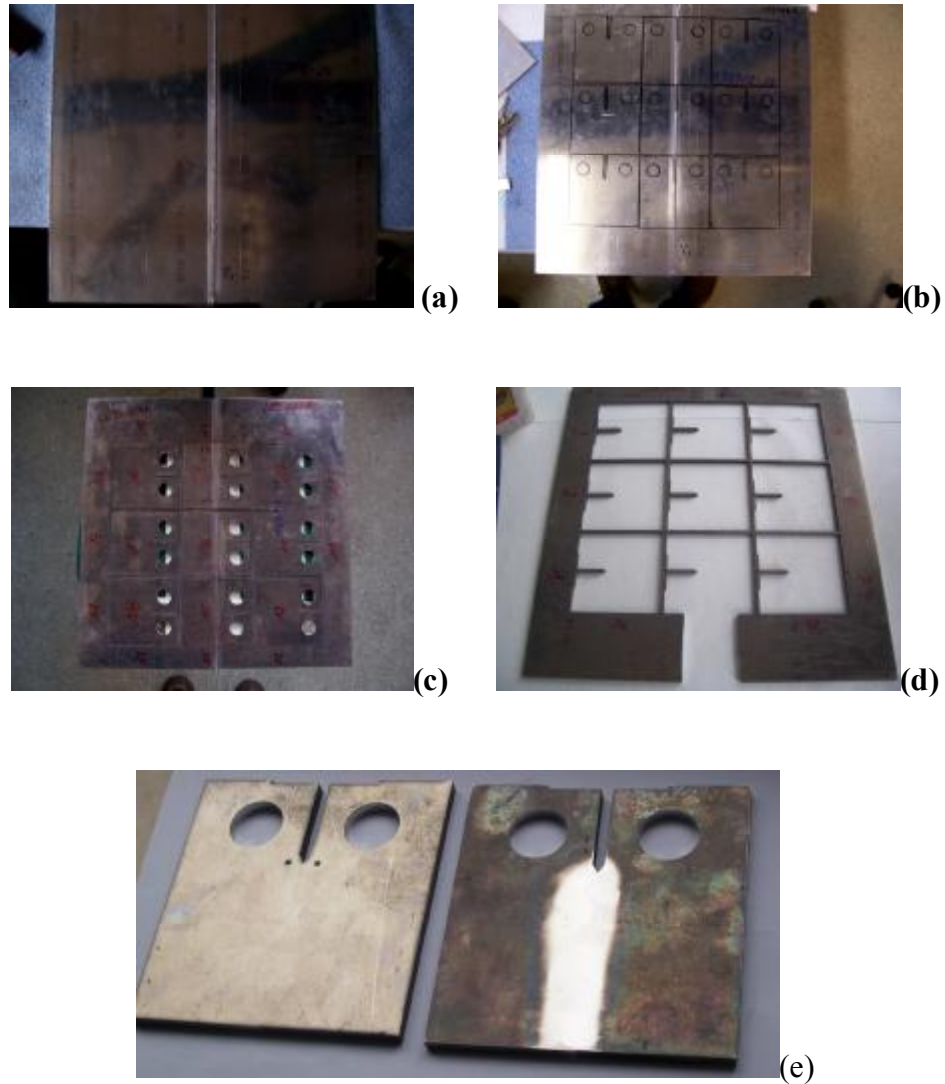


Figure 3.9. AA 6056 Aluminum plates joined with CO₂ laser beam welding

All of the fatigue crack propagation tests were conducted in accordance with ASTM E647. C(T) 100-type specimens were selected for the FCP tests (see Figure 3.10), the reason being that C(T) 100-type specimens allow for better examination of the effect of porosity compared to C(T) 50-type specimens.

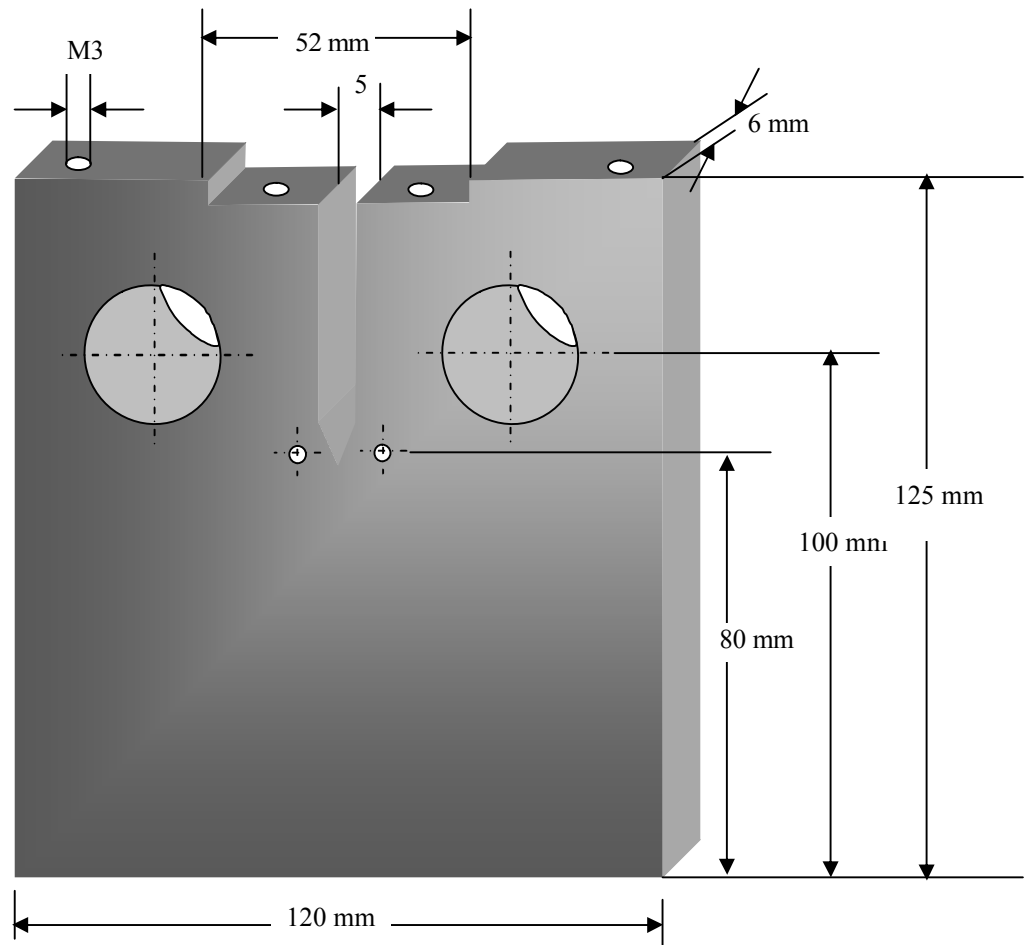


Figure 3.10 C(T) 100 specimens dimensions (ASTM399)

The loading rate and the frequency of the FCP tests were determined according to ASTM 647; they also had to meet the requirements of Eq. 3.11, which allows for the verification of a suitable ΔK value (determined from Eq. 3.2).

$$(W - a) \geq \left(\frac{4}{P} \right) \left(\frac{K_{\max}}{S_{YS}} \right)^2 \quad (3.1)$$

$$\Delta K = \frac{\Delta P}{B\sqrt{W}} f\left(\frac{a}{W}\right)^* \quad (\Delta P = P_{\max} - P_{\min}, \Delta K = K_{\max} - K_{\min}) \quad (3.2)$$

$$f\left(\frac{a}{W}\right)^* = \frac{2 + \frac{a}{W}}{\left(1 - \frac{a}{W}\right)^{3/2}} \left[0,886 + 4,64\left(\frac{a}{W}\right) - 13,32\left(\frac{a}{W}\right)^2 + 14,72\left(\frac{a}{W}\right)^3 - 5,60\left(\frac{a}{W}\right)^4 \right]$$

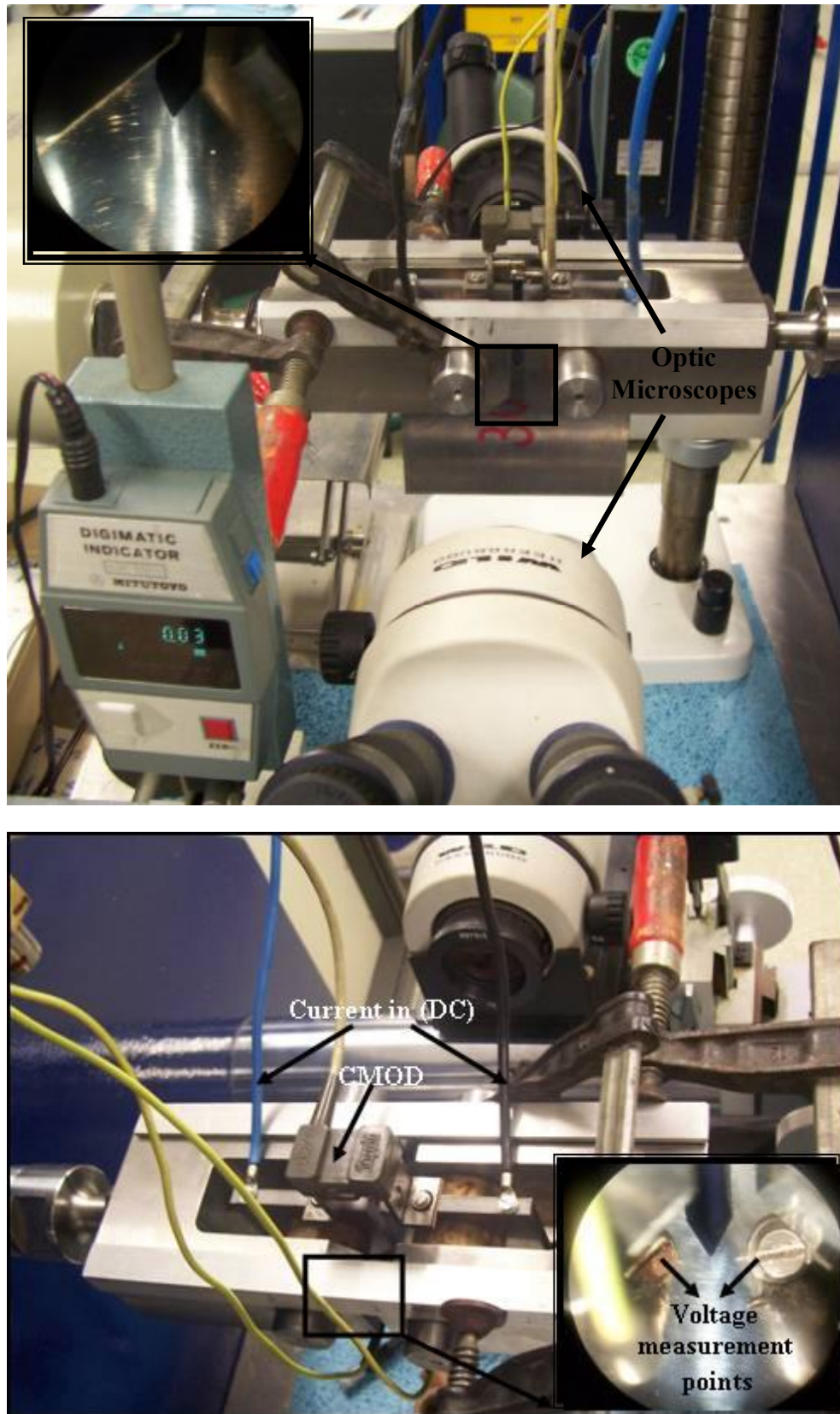


Figure 3.11 Front and top view of fatigue test machine

Fracture surfaces and crack propagation paths obtained from FCP tests have been investigated by optical microscopy and it has been seen that the porosity is a major problem in crack propagation in welded specimen; a special emphasis has been given to this fact.

3.5.1 Measurement of Fatigue Crack Propagation

Fatigue crack propagation during testing was measured both with a CMOD (Crack Opening Mouth Displacement) clip and EPD (Electrical Potential Drop) Technique; the increase in crack length has been transferred to the computer (see Figure 3.11). Moreover, crack length has been measured by digital microscopes from both sides and the three measurement values have been compared with each other.

The measurement according to Electrical Potential Drop technique was conducted by recording the change in potential (v) resulting from the change in crack length. Crack length versus EPD diagrams have been constructed from these measurements. Measurement details are given in Figure 3.12 and the coefficients are presented in Table 3.2. DC flow was employed in Al alloys (ASTM647).

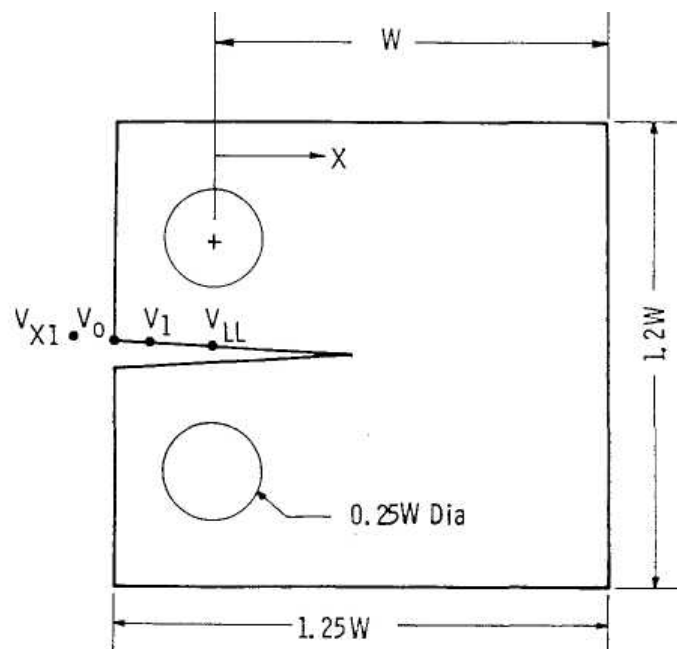


Figure 3.12 EPD measurement points in C(T) specimens

Table 3.2 Coefficients for EPD measurements points in C(T) specimens (ASTM647)

Meas, Location	X/W	C ₀	C ₁	C ₂	C ₃	C ₄	C ₅
C(T) Specimen							
V _{x1}	-0,345	1,0012	-4,9165	23,057	-323,91	1798,3	-3513,2
V ₀	-0,250	1,0010	-4,6695	18,460	-236,82	1214,9	-2143,6
V ₁	-0,1576	1,0008	-4,4473	15,400	-180,55	870,92	-1411,3
V _u	0	1,0002	-4,0632	11,242	-106,04	464,33	-650,68

$$a = a/W = C_0 + C_1 u_x + C_2 u_x^2 + C_3 u_x^3 + C_4 u_x^4 + C_5 u_x^5$$

$$u_x = \left\{ \left[\frac{EvB}{P} \right]^{\frac{1}{2}} + 1 \right\}^{-1} \text{ for EPD}$$

Measurement according to CMOD method was carried out by optically measuring the crack length and obtaining the CMOD (δ) versus load curves (Kusko, 2004).

$$a = a/W = 1.00098 - 4.66951X + 18.4601X^2 - 236.825X^3 + 1214.88X^4 - 2143.57X^5$$

$$X = \left\{ \left[\frac{EdB}{P} \right]^{\frac{1}{2}} + 1 \right\}^{-1} \text{ for CMOD}$$

CHAPTER FOUR

RESULTS AND DISCUSSION

4.1 Microstructural Aspects and Weld Quality

X-ray photographs were taken to identify the general problem of porosity in the fusion zone (FZ) of CO₂ laser beam welded aluminum alloys. As can be seen in Figure 4.1, there is a considerable amount of porosity in the weld seam.

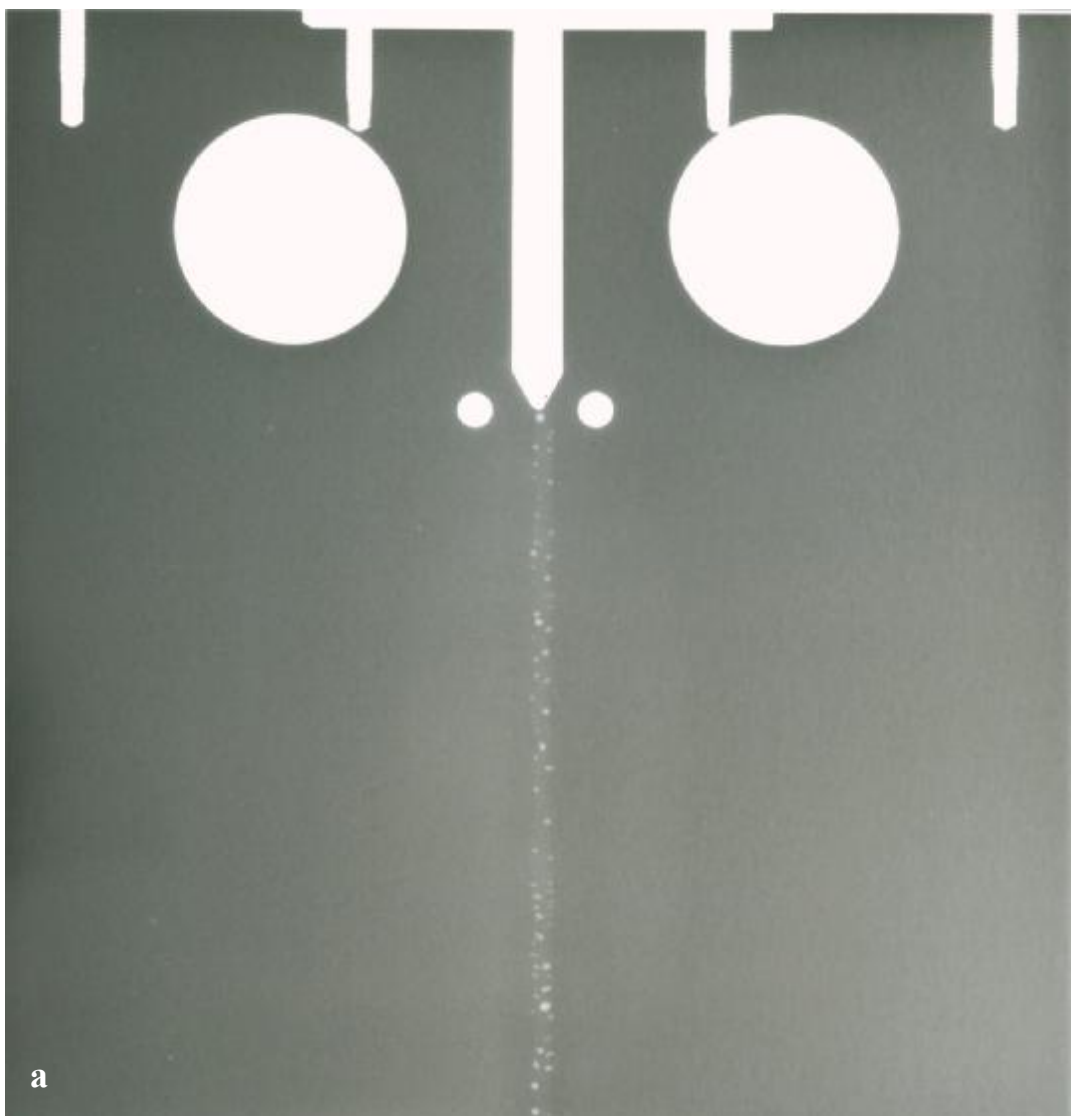


Figure 4.1 Porosity in the fusion zone laser beam welded joint used in this study (a,b)

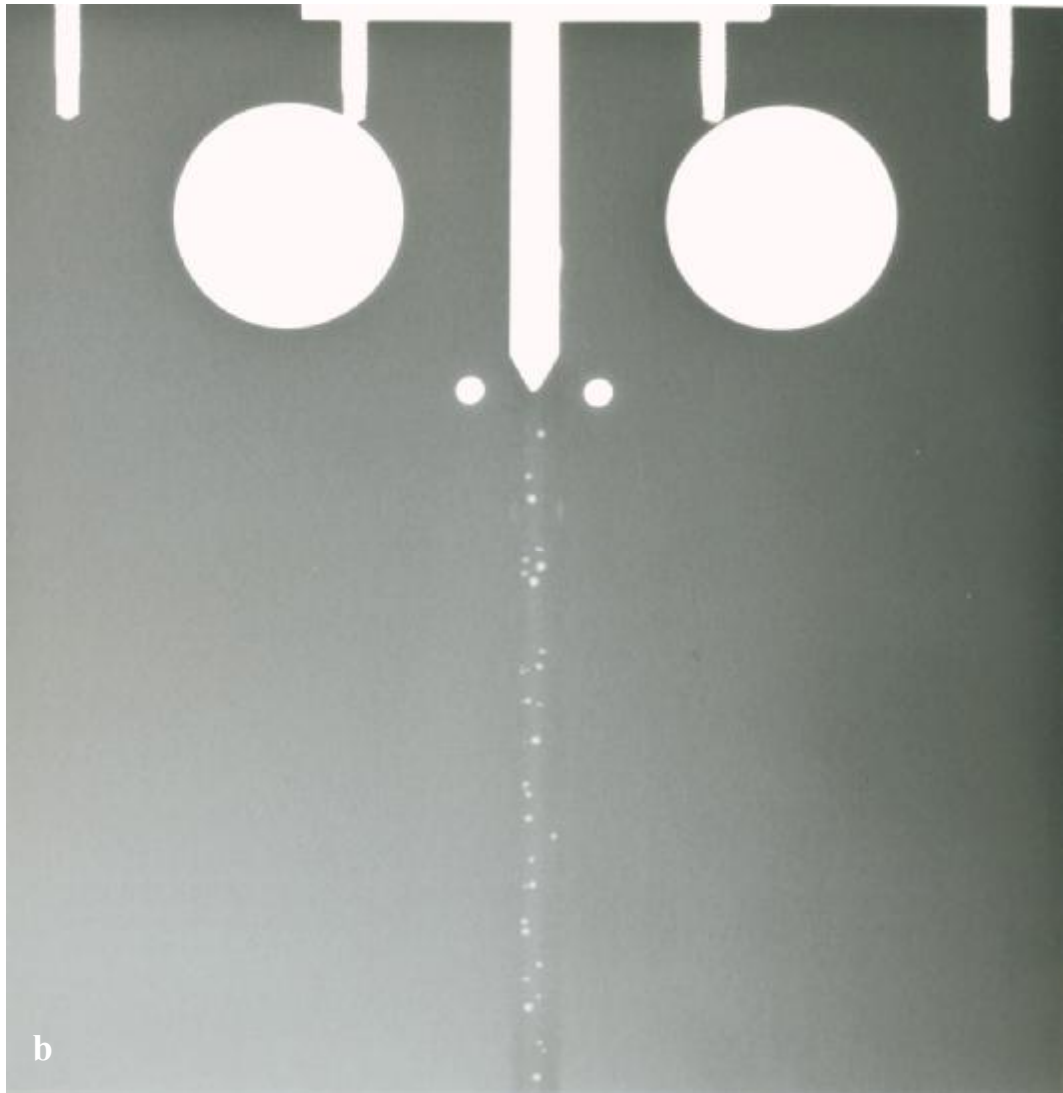


Figure 4.1 Porosity in the fusion zone laser beam welded joint used in this study (a,b) [Countined].

Specimens were examined under optical microscope in order to detect whether there are defects in the weld region besides porosity. It can be seen in the micrographs in Figure 4.2 that the welding was accomplished with no other defects. In optical microscope examinations, no phase in the weld region, like intermetallic layer, was detected, while some grain boundary liquation was detected in the fusion and heat affected zones.

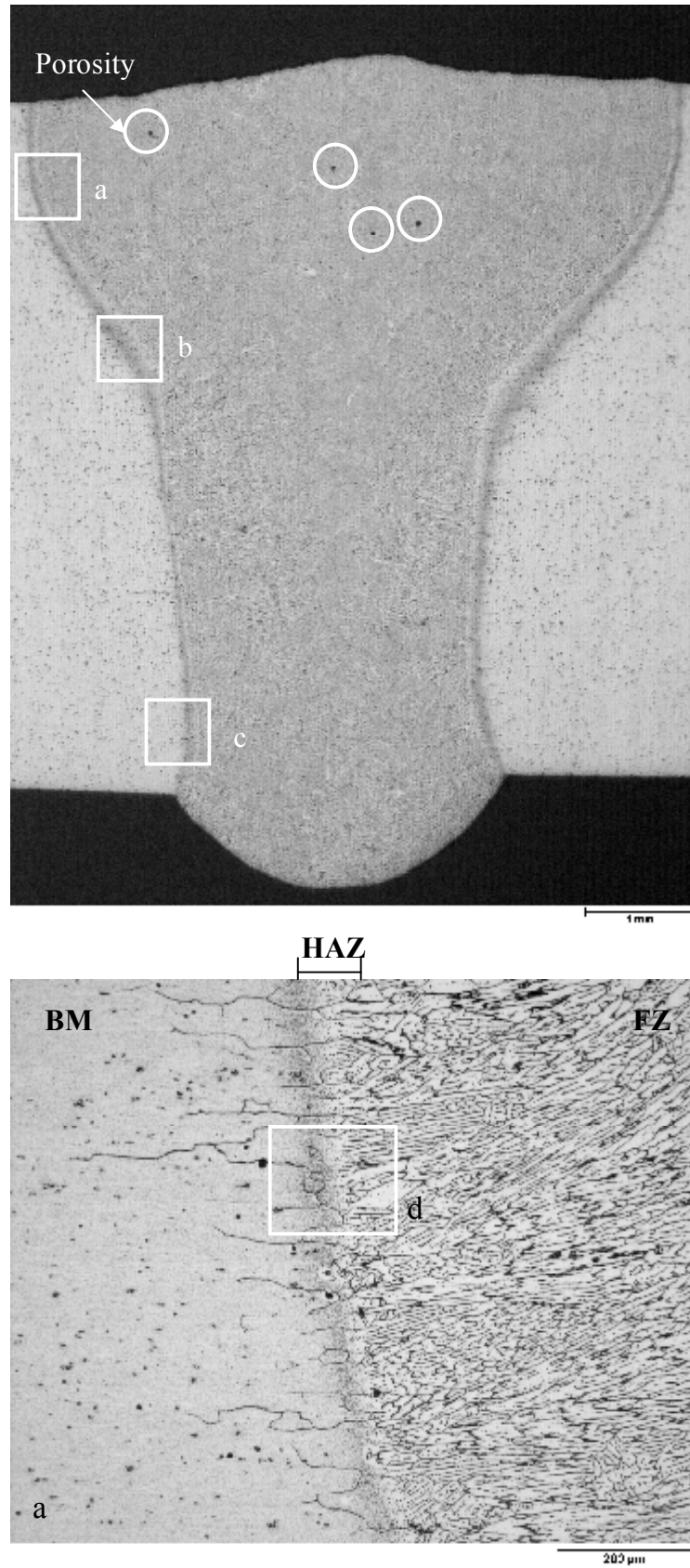


Figure 4.2 Micrograph of the weld area of AA6056 T6 and its details (a,b,c,d, and e)

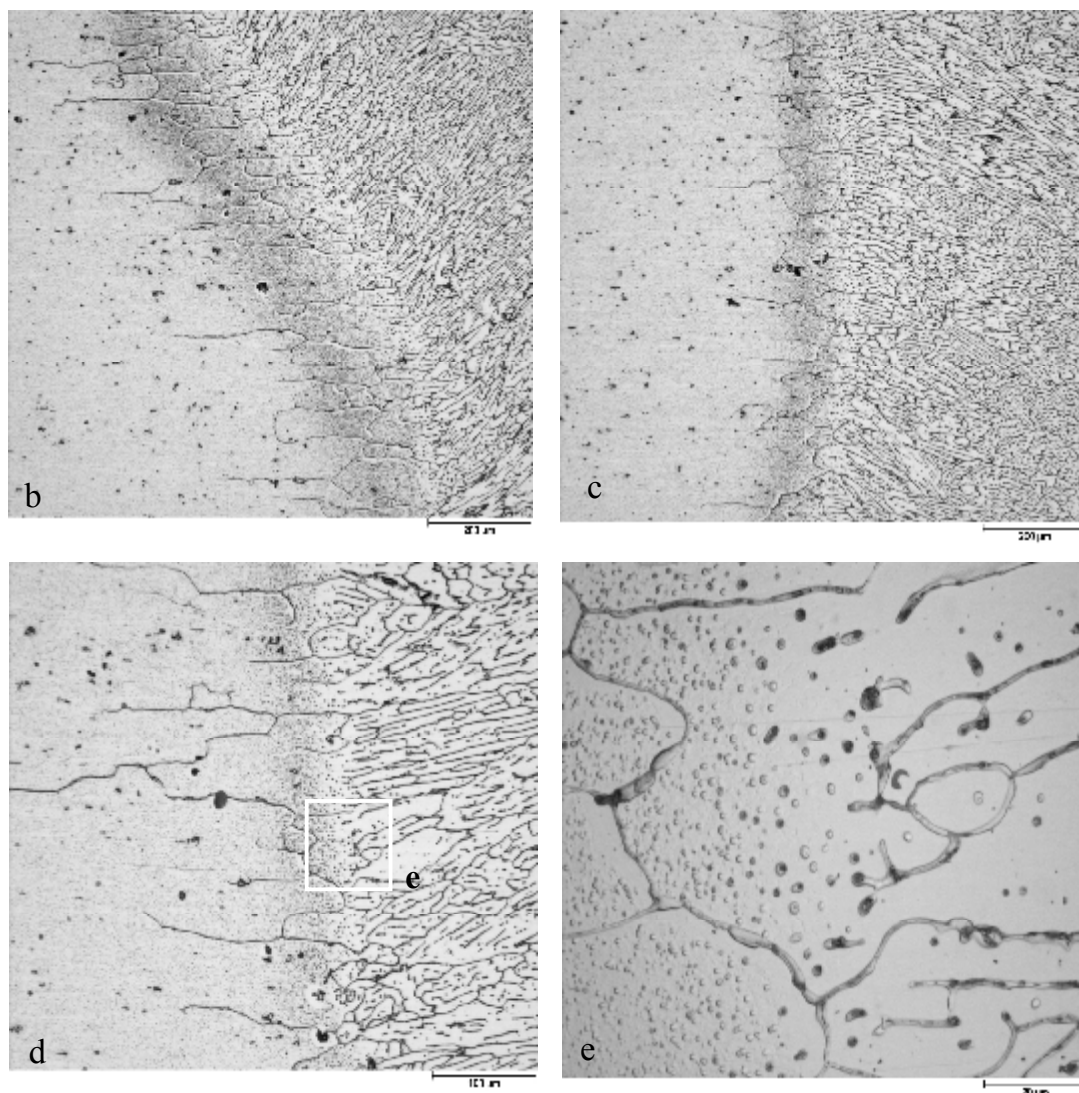


Figure 4.2 Micrograph of the weld area of AA6056 T6 and its details (a,b,c,d, and e) [Countined].

SEM micrographs of the BM, FZ and HAZ microstructures are shown in Figure 4.3. As seen in these SEM photos, no solidification cracking or liquation cracking have occurred in the FZ or the HAZ which are typical of aluminum alloys. No welding related problems were detected also at the HAZ near to the BM. The effect of grain boundary liquation to crack growth will be discussed in the following sections.

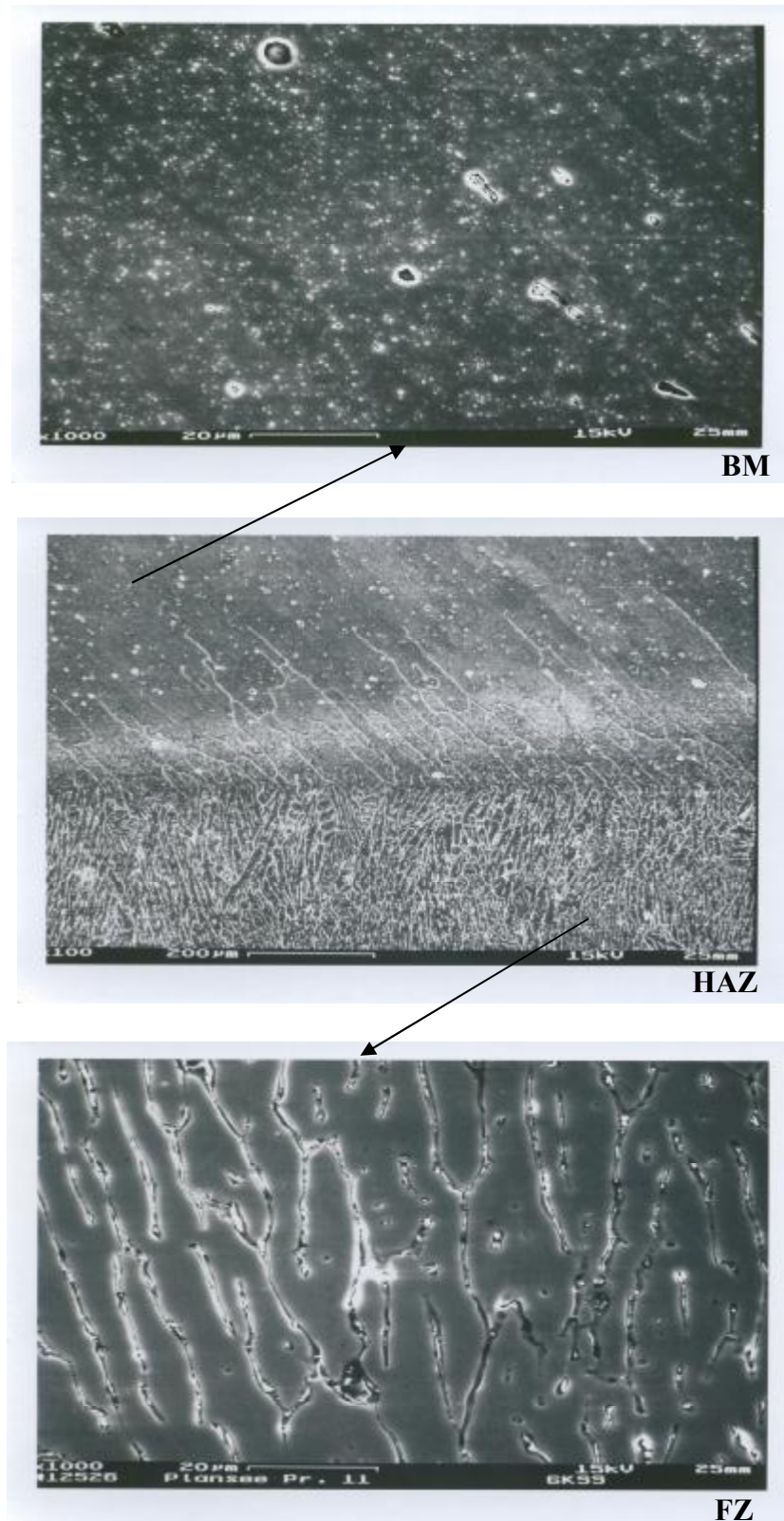


Figure 4.3 SEM micrographs of 6056-T6 BM, FZ, and HAZ

4.1.1 Microhardness Profile

Microhardness profiles obtained from three different locations as explained in Experimental Procedure Section are given in Figure 4.4. The examination of hardness decrease by the help of SEM analysis are given in Figure 4.4.

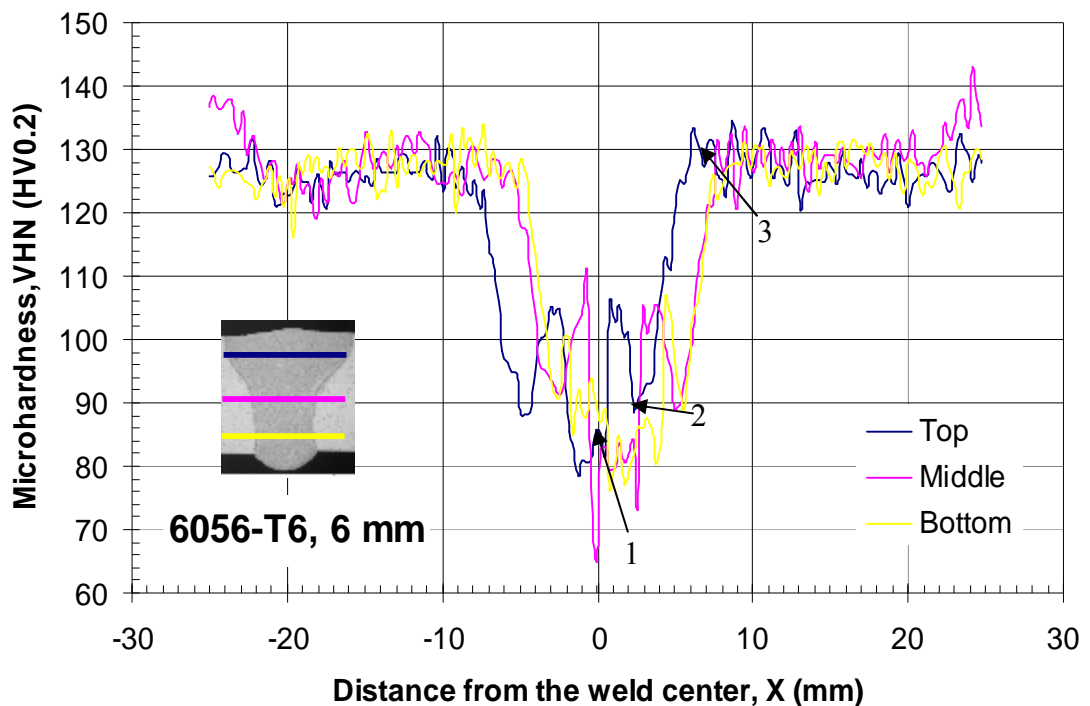


Figure 4.4 Microhardness profile of the weld joint at T6 condition.

The reason for the decrease in the microhardness in the joint region is due to the fact that overaging in the precipitation aged (T6) aluminum alloy in this region takes place as a result of heat input during welding. This is a usual case in the fusion welding of 6xxx series Al-alloys as overaging takes place at temperatures higher than 595 °C, as can be seen in Figure 4.5 and Figure 4.6.

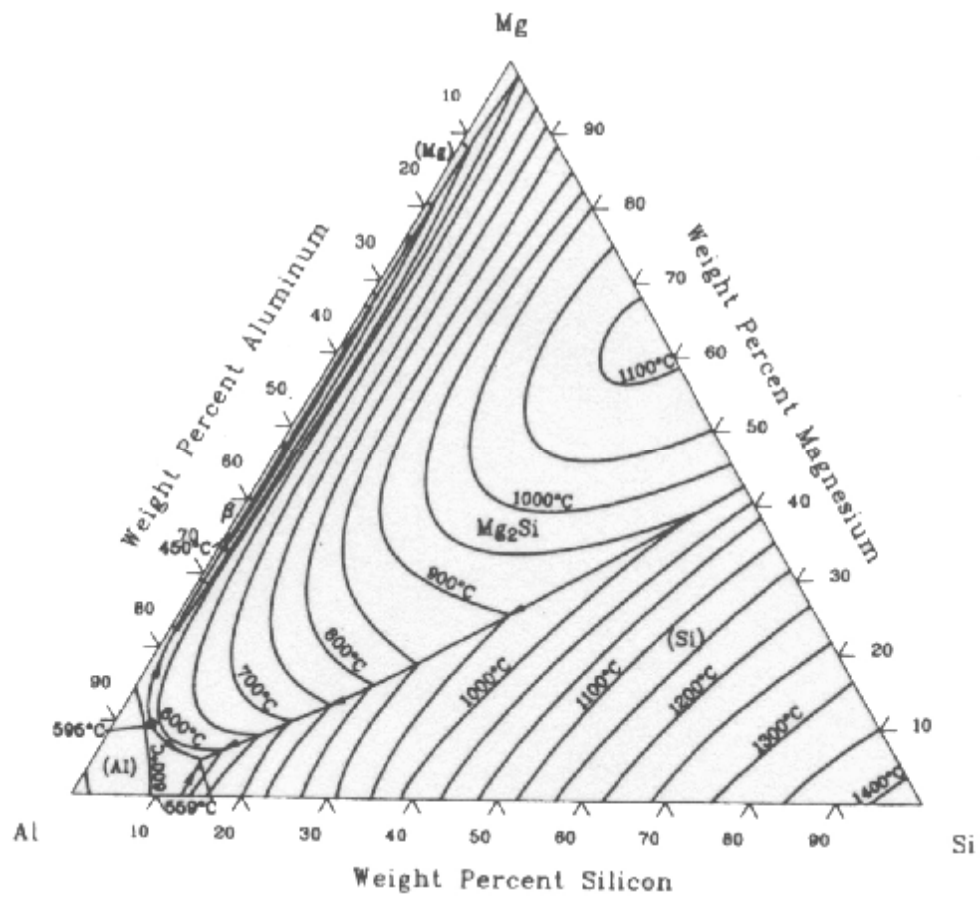


Figure 4.5 The phase diagram of Aluminum-Magnesium-Silicon (Horn & Kent, 1967)

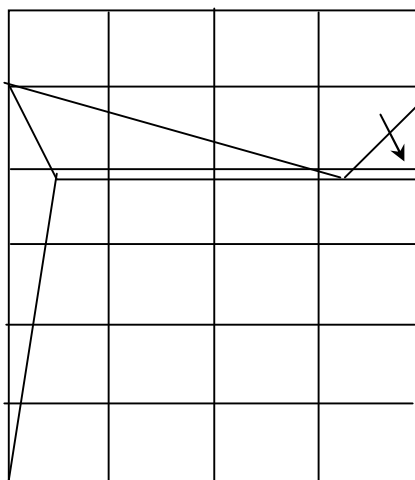


Figure 4.6 The quasi-binary phase diagram of Magnesium-Silicon with Aluminum (Horn & Kent, 1967)

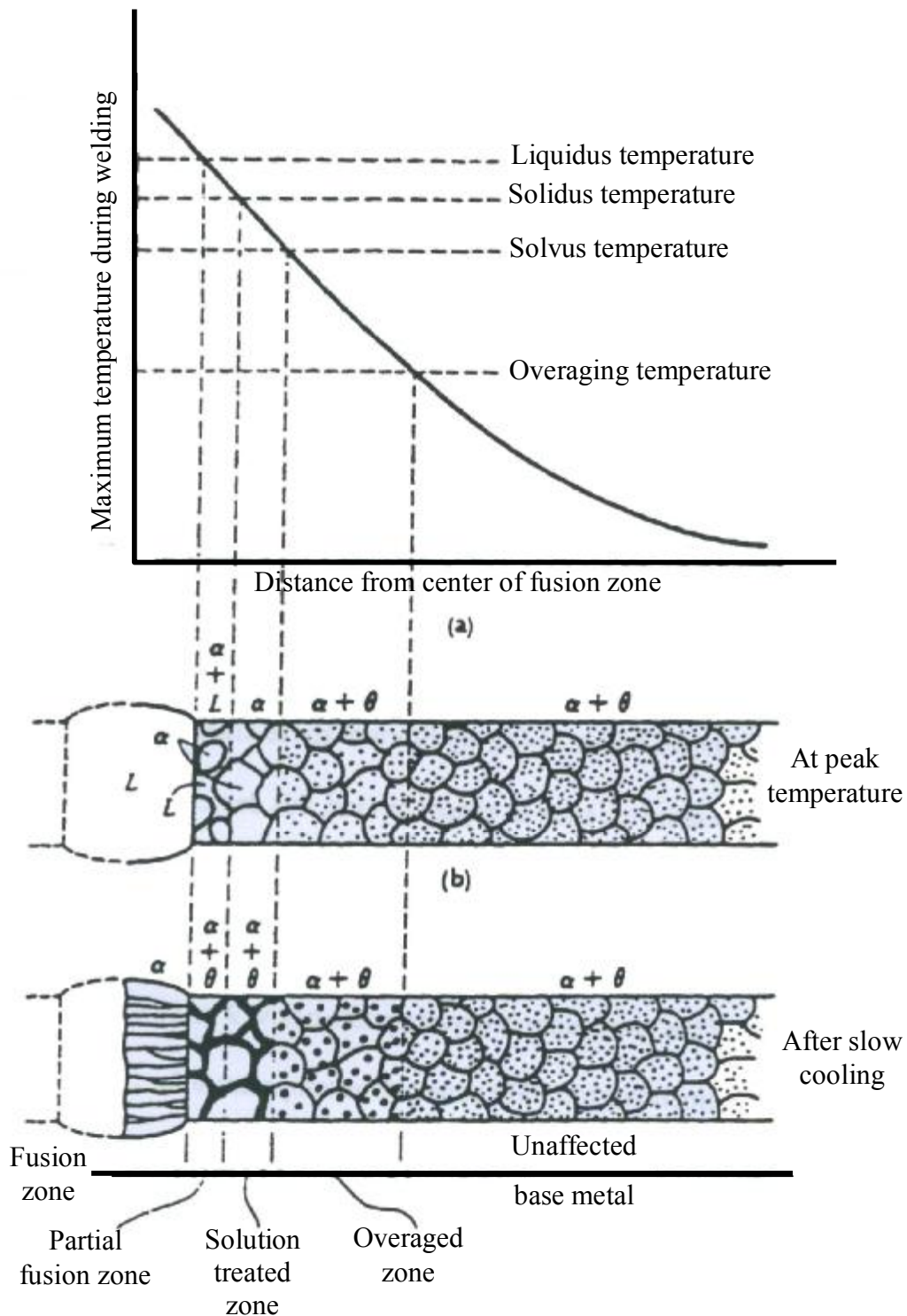


Figure 4.7 Microstructural changes that can occur in age-hardened alloys during fusion welding (Marsico & Kossowsky, 1989)

When welding an age hardenable alloy, the heat affected zone area can be thought of as two temperature zones. The lower temperature zone near the unaffected base metal is exposed to temperatures just below the solvus line and may overage, a process associated with the formation and growth of equilibrium precipitates. As temperatures exceed the various solvi, the respective phases are dissolved. Subsequently, at positions adjacent to the fusion zone higher peak temperatures are experienced and greater amount of dissolution of strengthening phases can occur. The higher temperature zone becomes solutionized eliminating the effects of age hardening (See Figure 4.7) (Marsico & Kossowsky, 1989).

Compared to other conventional welding processes, laser beam welding offers the benefit of narrow heat affected zones that help minimize metallurgical problems that can arise from welding age hardened aluminum alloys. The low net weld heat input associated with this process, results in rapid solidification rates in the fusion zone and lower peak temperatures in the adjacent base metal. Subsequently, this results in the formation of narrow heat affected zones, and therefore reduced thermal degradation of the adjacent base metal occurs. Moreover, the high solidification rates in the fusion zone result in a fine-grained microstructure, which helps retaining the strength of the re-solidified aluminum (Martukanitz, 1993).

At the regions indicated by 1, 2 and 3 in the middle location of the hardness profile (Fig. 4.4), micrographs were obtained and microstructural analysis and variations in the chemical compositions at grain boundaries, as well as the chemical composition of the matrix were determined and presented in Table 4.1. Analysis was carried out around the hardness indentations at the middle location. SEM photograph (Jeol JSM-6060) was analysed in the Department of Metallurgy and Materials Engineering of DEU, Turkey.

1st region: It is the region around the hardness indentation point 0 ($x = 0\text{mm}$) in the microhardness profile. It is also the center point of the fusion zone. (See Figure 4.8 a b)

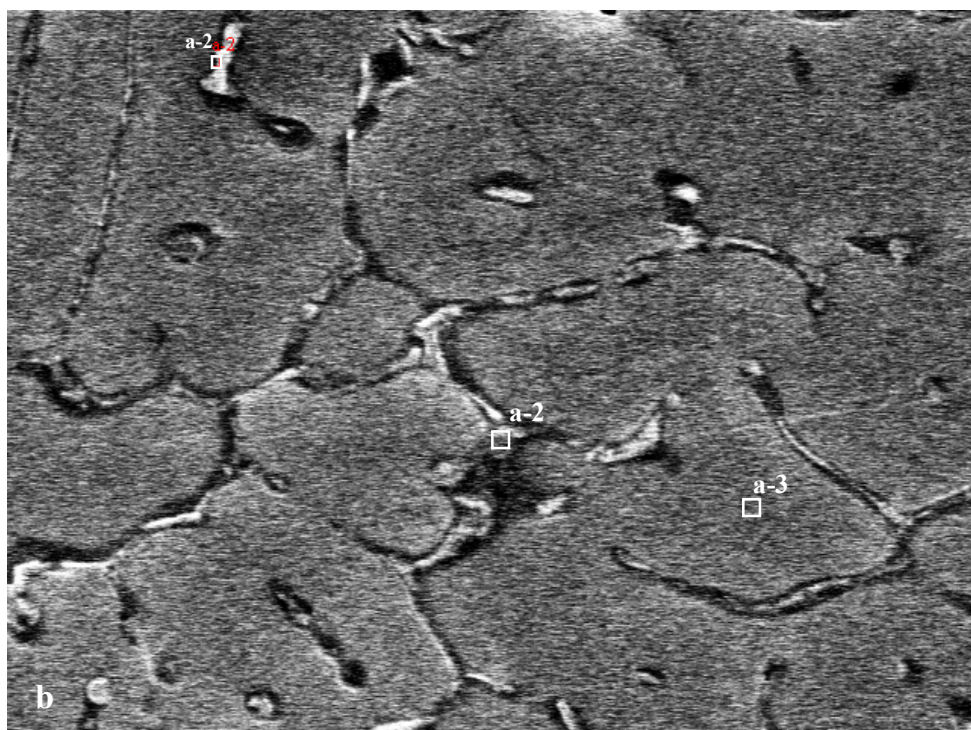
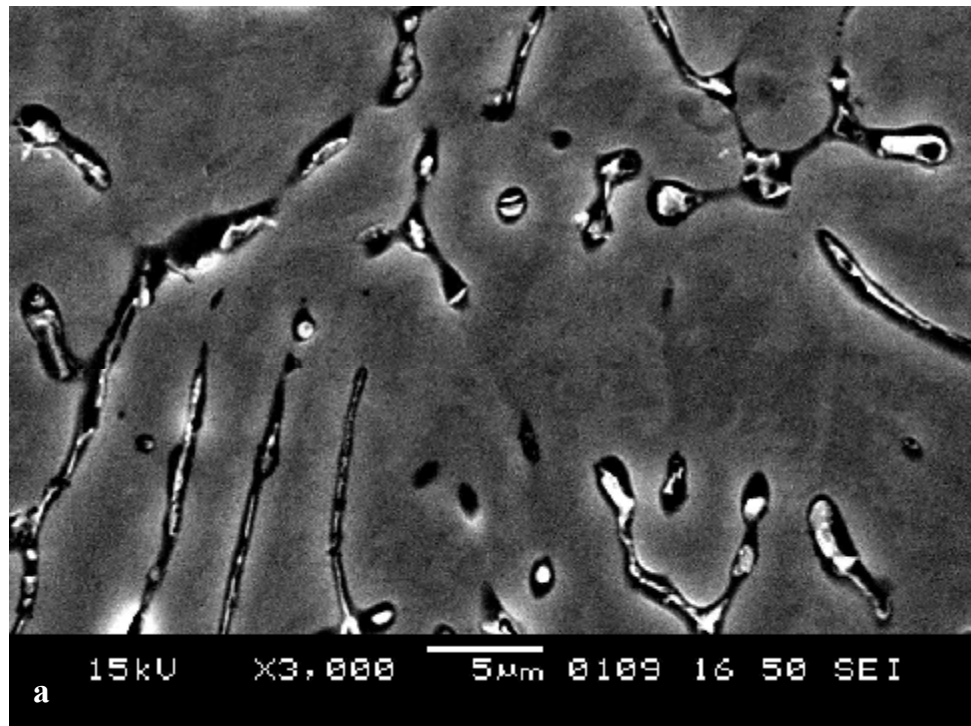


Figure 4.8 SEM micrograph of the 1st region (a) and detailed analysis points (b)

2nd region: This region corresponds to the hardness indentation, which is about 2.5 mm away from point 0. Although this region is still in the FZ, it is the region of overaging. What is of interest here is that when Figure 4.8 and Figure 4.9 are compared, it is seen that grain boundary liquation distribution is less in this region. Grain size increase may be the cause for this.

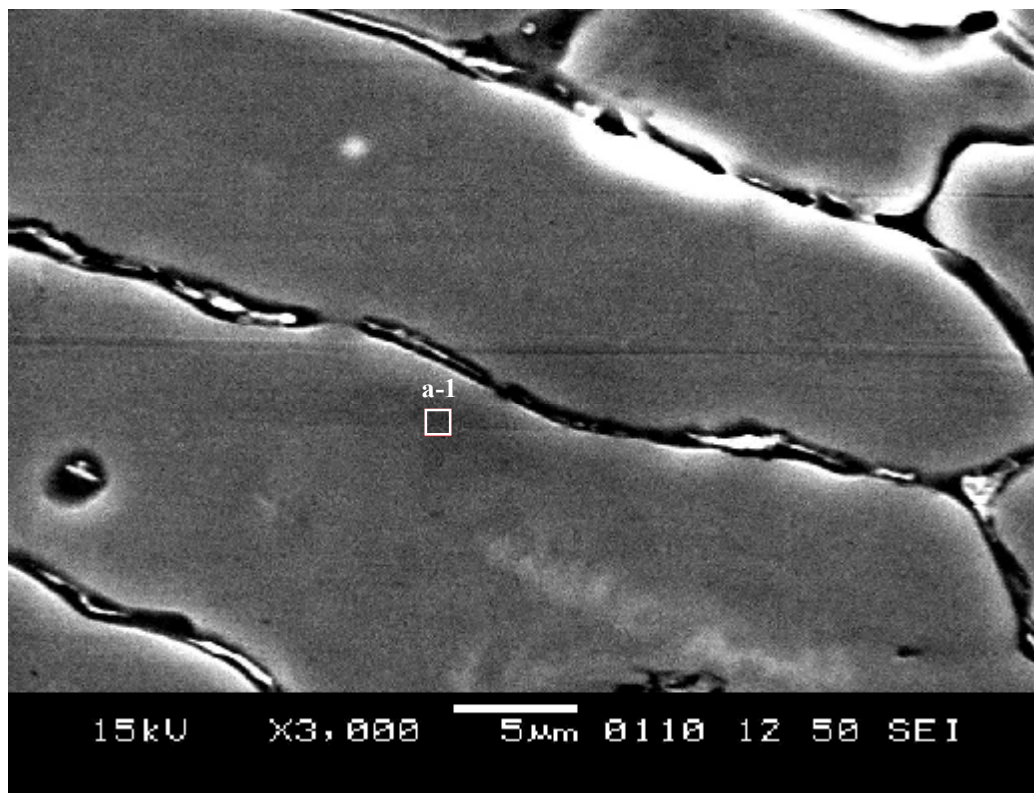


Figure 4.9 SEM Micrograph of the 2nd region and analysis points

3rd region: This point is 7 mm away from the 1st point. It was chosen for the determination of BM chemical composition. (See Figure 4.10)

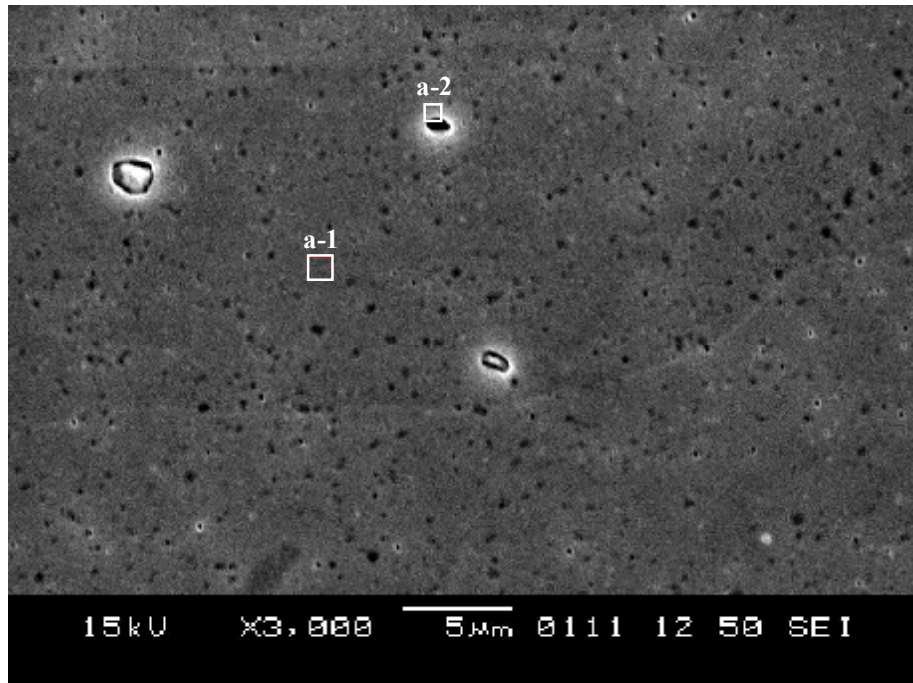


Figure 4.10 SEM photograph of the 3rd region and analysis points

When the chemical compositions given in Table 4.1, where SEM analyses were carried out, are examined, it is seen that there is an increase in Si and Mg content. In terms of FCP, this causes different crack growth rates in the BM and the FZ.

Table 4.1 6056-T6 Chemical analyses results

Zone		Cu (wt. %)	Mg (wt. %)	Mn (wt. %)	Fe (wt. %)	Si (wt. %)	Al (wt. %)
First Zone	a ₁	0,555	1,249	0,282	0,079	1,422	96,412
	a ₂	2,944	3,167	0,615	0,402	7,292	85,580
	a ₃	0,270	0,961	0,399	0,093	0,124	98,144
Second Zone	a ₁	1,081	1,924	0,273	0,155	1,112	95,454
Third Zone	a ₁	0,589	1,416	0,261	0,080	0,449	97,205
	a ₂	0,656	1,329	0,174	0,054	0,352	97,434

Parameters : kV 20,0

Takeoff Angle 35,0

Elepsad Livetime 100,0

4.2 Tensile Test

Full stress-strain curves have been obtained using base metal transverse tensile specimens (both in LT and TL directions, that is, parallel and normal directions to the rolling direction) and welded transverse tensile specimens (3 specimens for each condition). Test results representing each condition are given in Table 4.2. Mechanical properties obtained from tensile tests are illustrated in Figure. 4.11

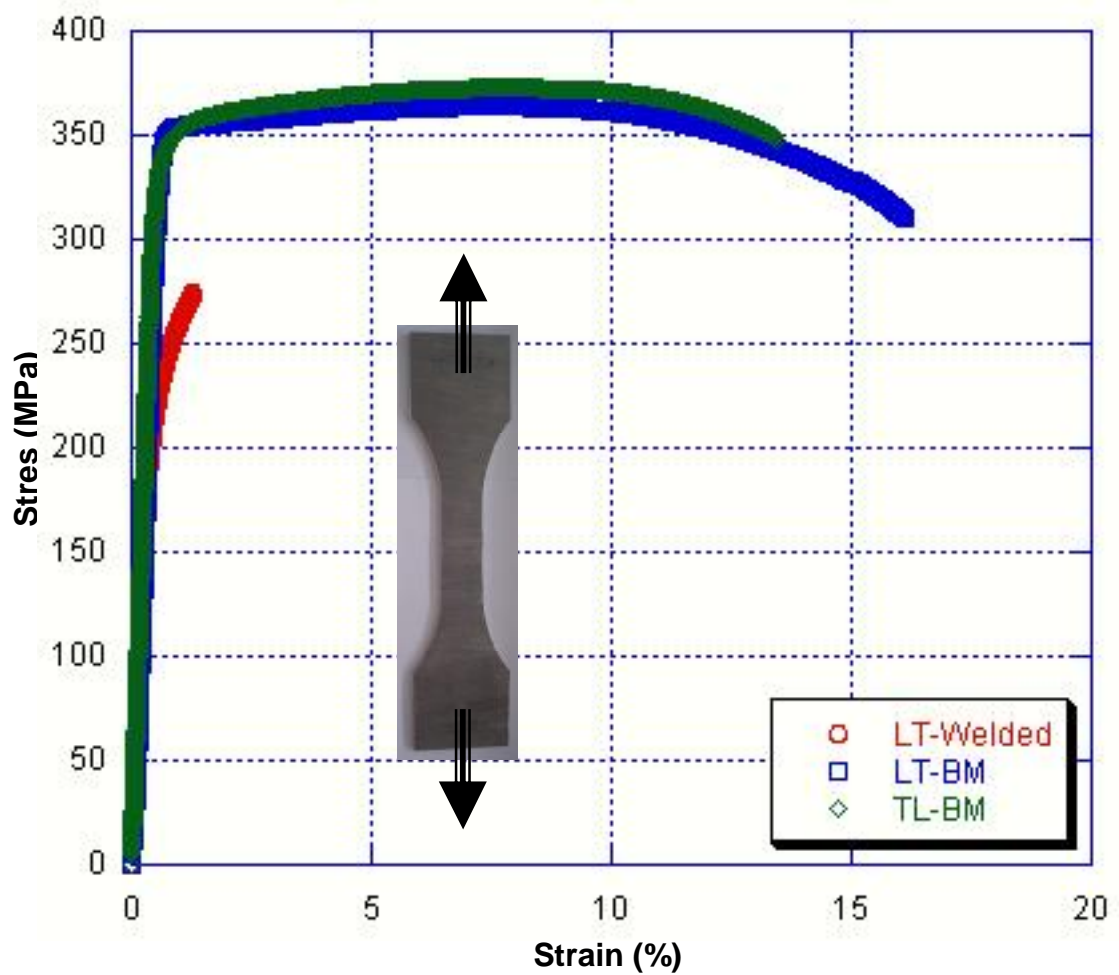


Figure 4.11 Stress-strain curves of longitudinal, transverse base metal, and longitudinal welded specimens

Table 4.2 Tensile properties of Al6056-T6 as obtained from standard base metal and welded tensile specimens

Material	E (GPa)		R _{p0,2} (MPa)		R _m (MPa)		A (%)	
6056 T6-L	71,6	70,9±1	348	347±1	363	362±1	16,3	16,0
	69,8		345		360		15,8	
	71,8		348		362		16,1	
6056 T6-TL	72,6	71,4±1	348	347±1	372	371±1	13,8	13,2
	70,8		345		371		13,0	
	71,8		348		372		12,9	
6056 T6-Welded	71,1	70,3±1	225	226±1	275	275±1	0,88	0,90
	69,6		225		276		0,94	
	69,8		227		275		0,94	

Tensile property profiles of the welded joints obtained by micro-flat tensile specimens are illustrated in Figure 4.12. Variations in strength and hardness values in the weld zone are in good agreement (see Fig. 4.4 and Fig. 4.12). Furthermore, these values are consistent with transverse tensile specimen results (see Fig. 4.13).

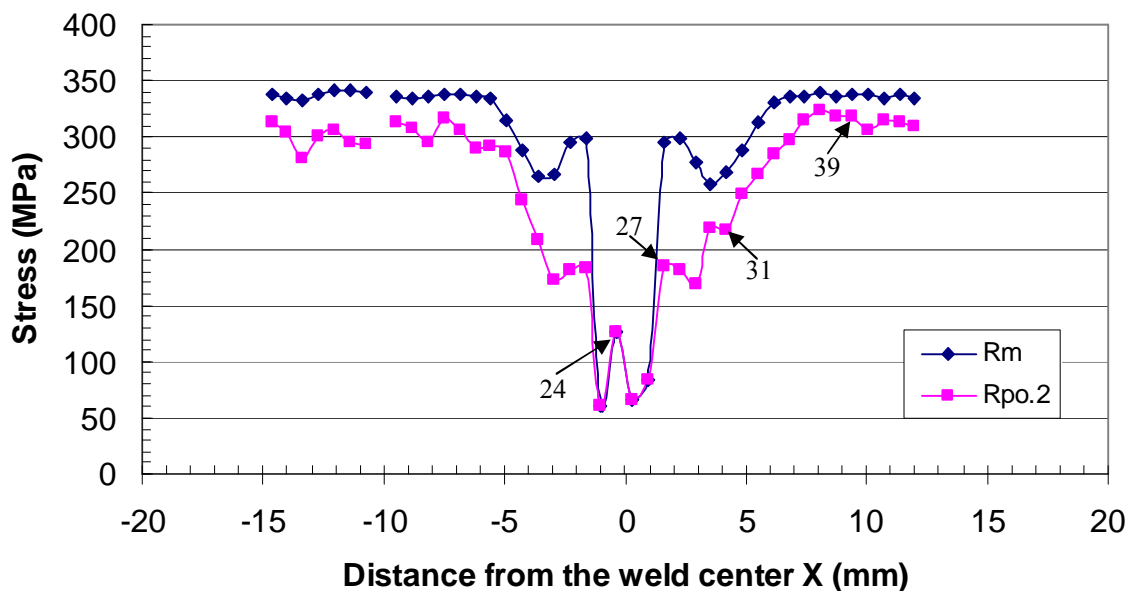


Figure 4.12 Tensile property profile of the welded joint from micro-flat tensile specimens

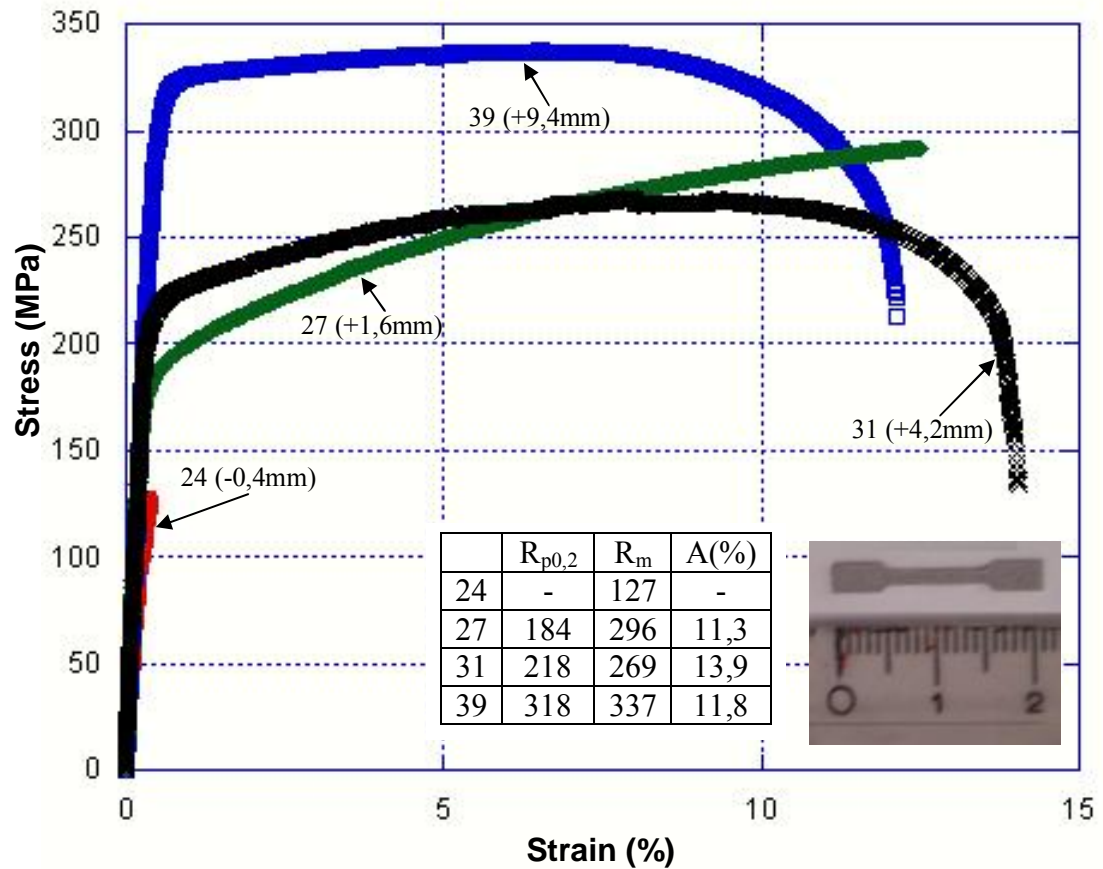


Figure 4.13 Stress-strain curves of base metal microtensile and all-weld microtensile specimens

$$M^* = \frac{R_{m-welded}}{R_{m-BM}} = \frac{275}{371} = 0,74$$

M^* : Weld material mismatch ratio (UTS (welded sample)/UTS BM)

4.3 FCP Test Result

$da/dN-\Delta K$ curves have been constructed using both EPD and CMOD measurement techniques (Figure 4.14). It has been seen that similar results are obtained with both techniques. In order to obtain unity all $da/dN-\Delta K$ curves are drawn with respect to CMOD.

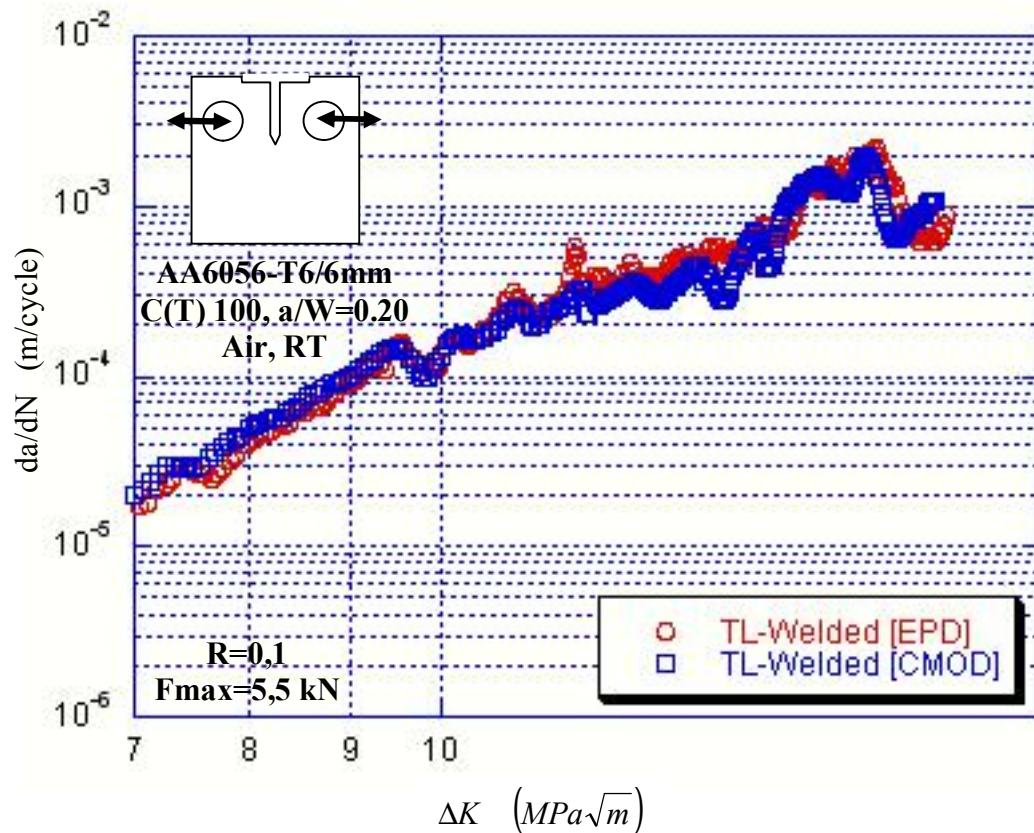


Figure 4.14 da/dN- ΔK curves according to EPD and CMOD measurement techniques

Appropriate parameters to be applied to LT-BM, TL-BM and TL-welded C(T) specimens are calculated separately according to ASTM 647 Norms. The maximum load, the frequency and other related parameters for valid crack lengths (between $0,20 \leq a/W \leq 0,60$) are calculated. As a result of these calculations, the applied frequency was 10 Hz in all FCP tests, the maximum load was 5.5 kN and all tests were conducted in air at room temperature.

$$\frac{da}{dN} = C_i \Delta K^{m_i} \quad (4.1)$$

In order to calculate the constants in Paris-Erdogan equation (4.1) the curves in Figures 4.15, 4.16, and 4.17. are used. By the method of curve fitting to these curves, the constants C (or A) and m (or n) in Eq 4.1. are calculated. The values of the constants are given in Table 4.3.

Table 4.3 C and m values

Specimens	Stress ratio							
	0,1		0,3		0,5		0,7	
	m	C	m	C	m	C	m	C
LT-BM	2,6	$1,3 \cdot 10^{-7}$	3,0	$5,8 \cdot 10^{-8}$	3,6	$1,5 \cdot 10^{-8}$	4,5	$3,3 \cdot 10^{-9}$
TL-BM	3,9	$2,9 \cdot 10^{-7}$	3,8	$7,7 \cdot 10^{-9}$	4,1	$6,9 \cdot 10^{-9}$	5,0	$1,7 \cdot 10^{-9}$
TL-Welded	7,7	$5,8 \cdot 10^{-14}$	5,8	$4,6 \cdot 10^{-11}$	3,6	$1,8 \cdot 10^{-8}$	3,9	$2,1 \cdot 10^{-8}$

In Table 4.3, as seen from the variation in constant “m”, since the crack propagation direction in LT-BM specimens is transverse to the rolling direction, the crack propagation rate is slower compared to TL-BM. In TL-welded specimens, the FCP rate is faster compared to BM. This fact can also be seen in the crack length-number of cycle graphics.

When the graphics in Figures 4.18, 4.19, 4.20 and 4.21 are examined in detail, in TL-welded specimens, there is retardation in crack initiation due to the decrease in R value. The retardation for R=0.1 is shown in Figure 4.22. Since the yield and tensile strengths of the weld region are lower compared to those of the base metal, the value of ΔK is greater in this region and, therefore, some amount of plastic yielding occurs at this place locally. (see Fig. 4.24). There is a visible wake zone in Figure. 4.24, while there are no visible wake zones in BM specimens in Figs. 4.25a and 4.26a. In Fig. 4.27 for R=0.7, in TL-welded specimens, since the value of ΔK is low, there is no plastic zone formation and therefore, no retardation in crack initiation (See Figure 4.23).

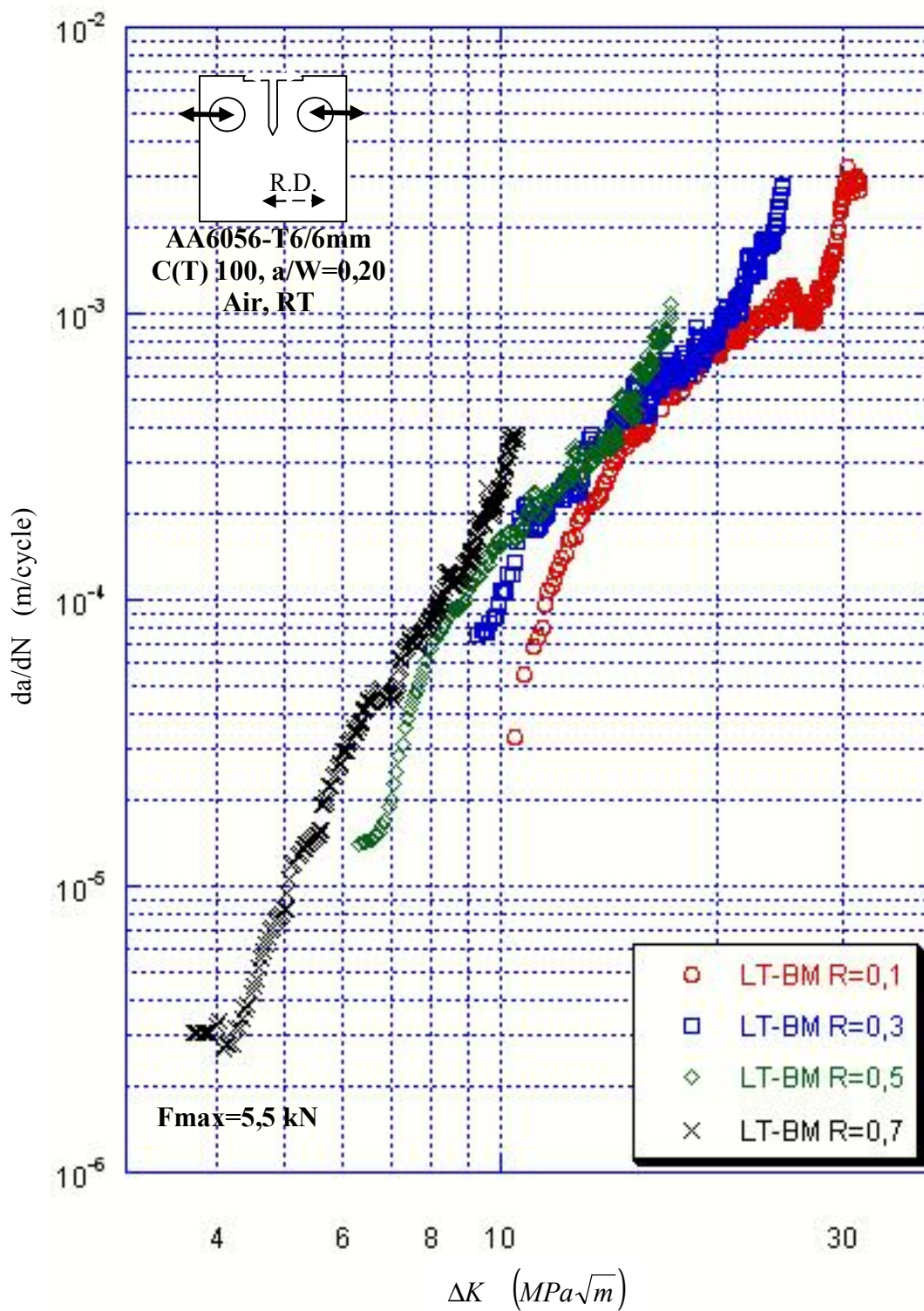
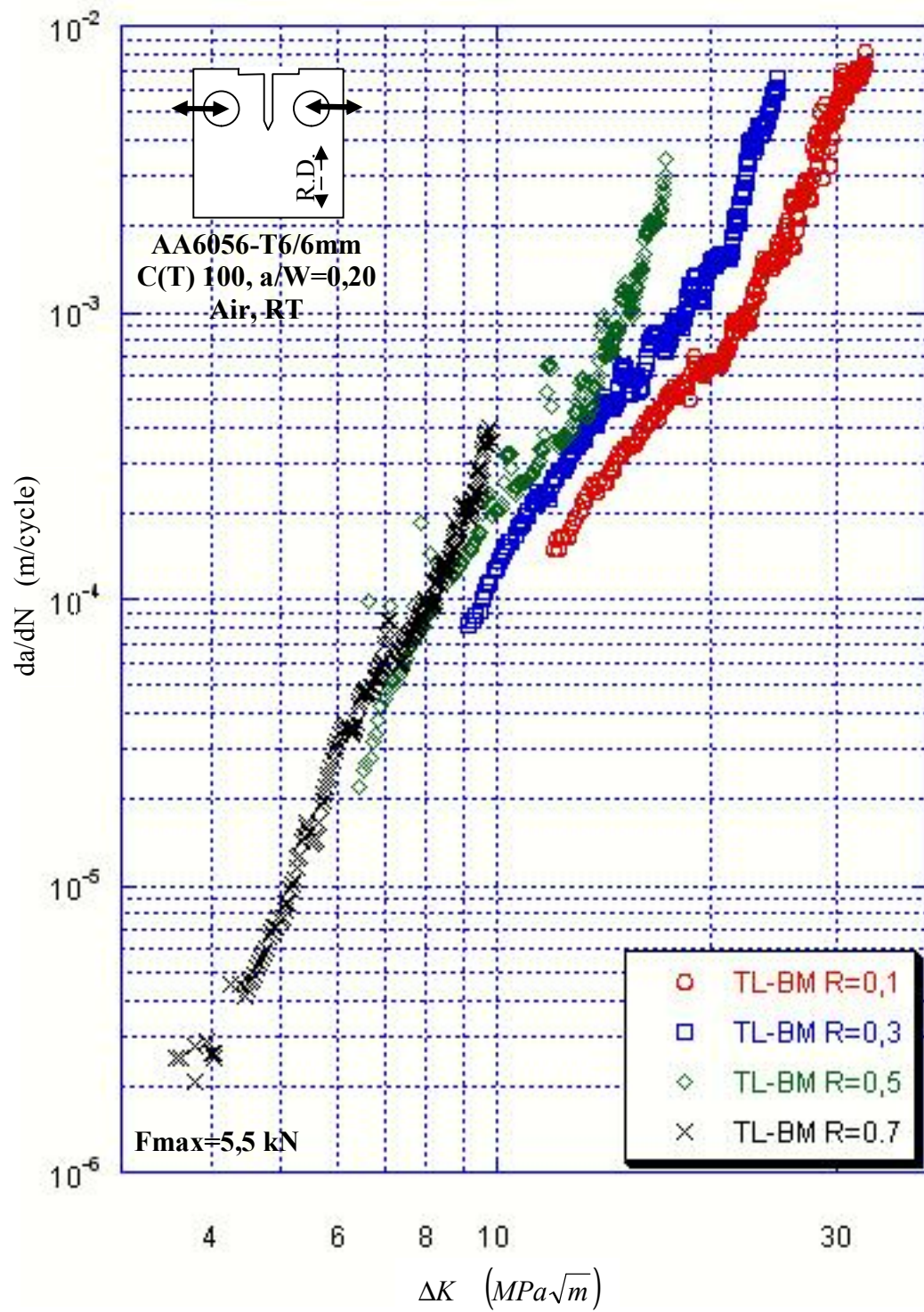


Figure 4.15 da/dN - ΔK curves of LT-BM specimens

Figure 4.16 da/dN - ΔK curves of TL-BM specimens

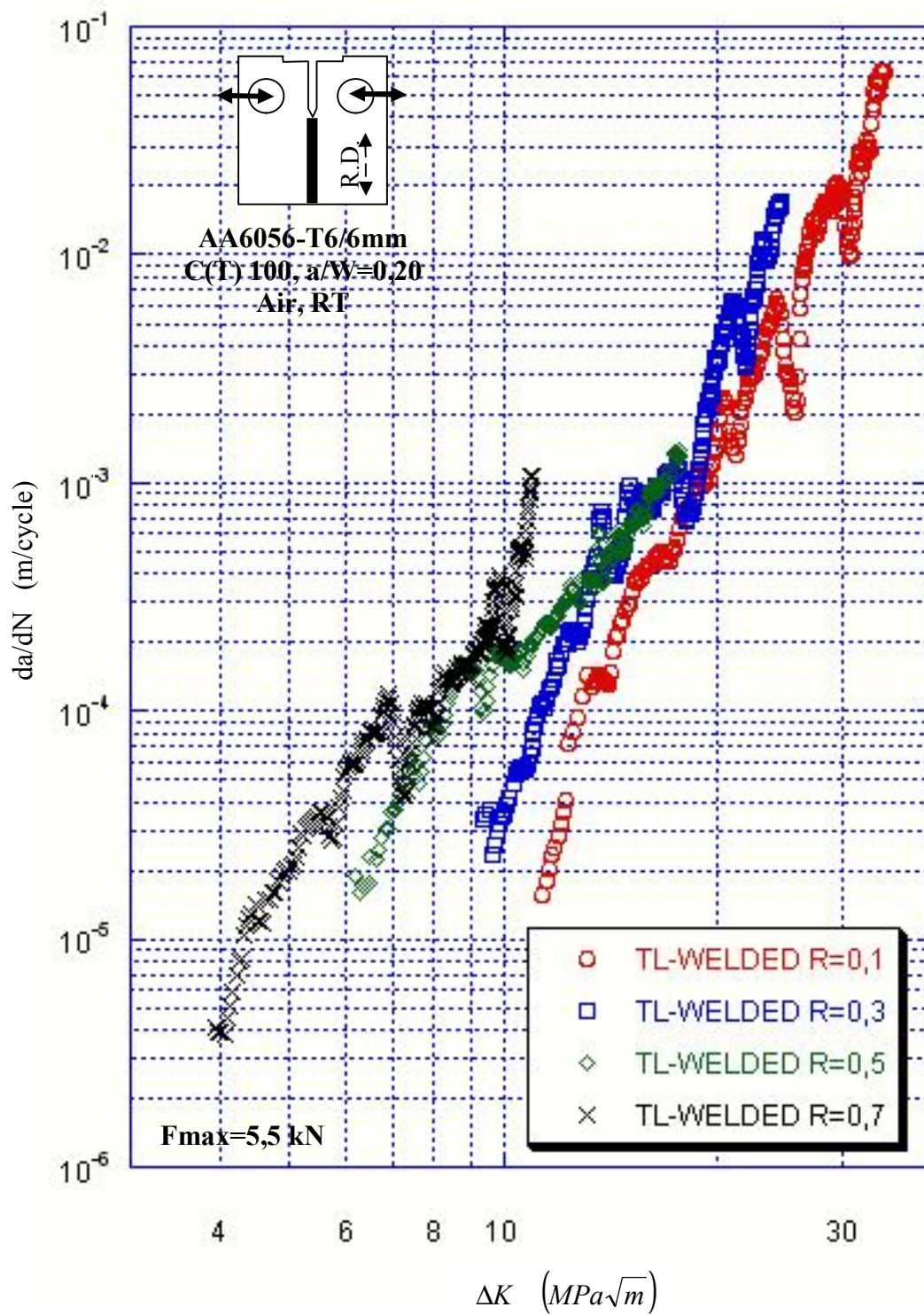


Figure 4.17 da/dN - ΔK curves of TL-welded specimens

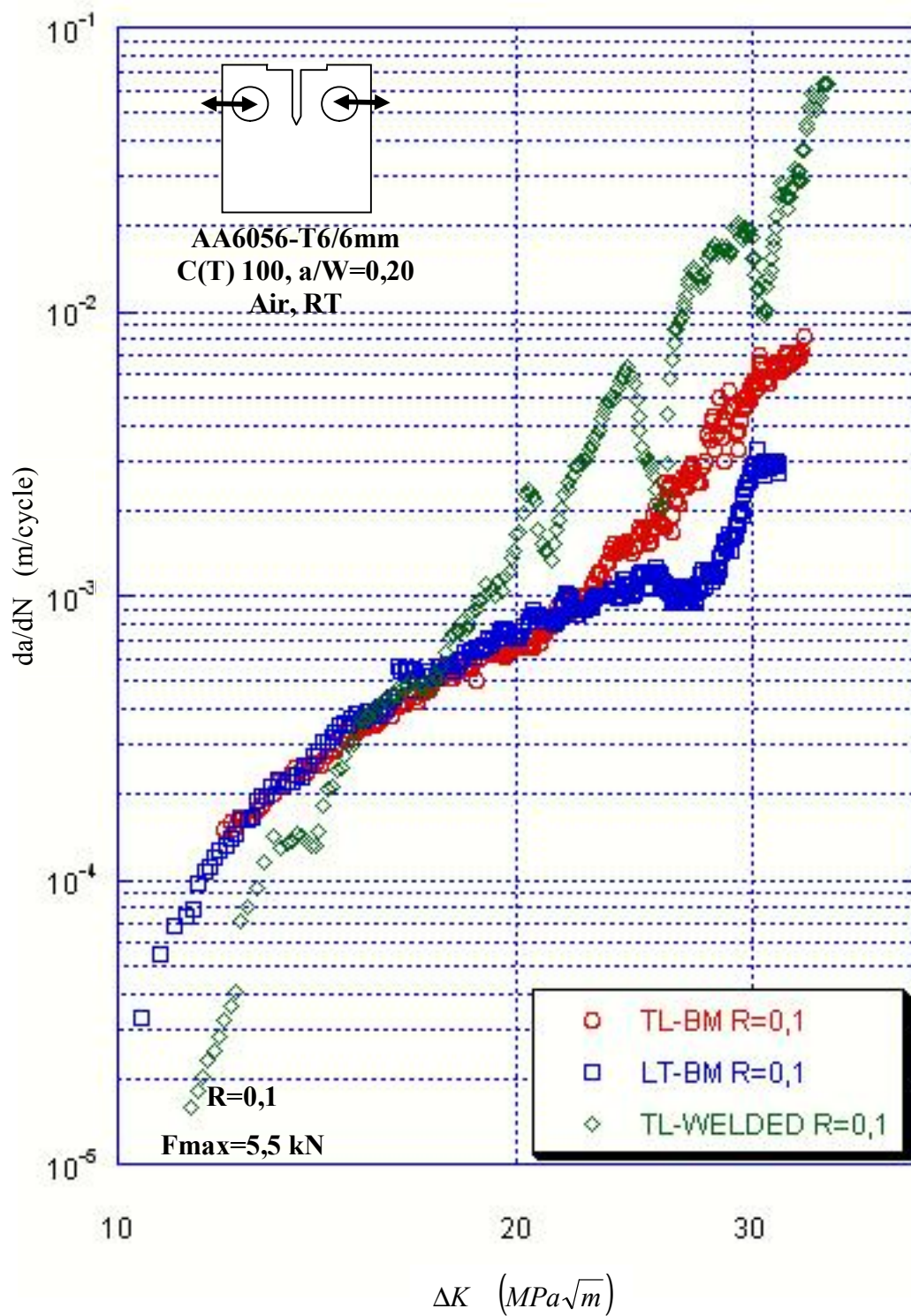


Figure 4.18 da/dN - ΔK curves of TL-BM, LT-BM and TL-welded specimens for $R=0,1$

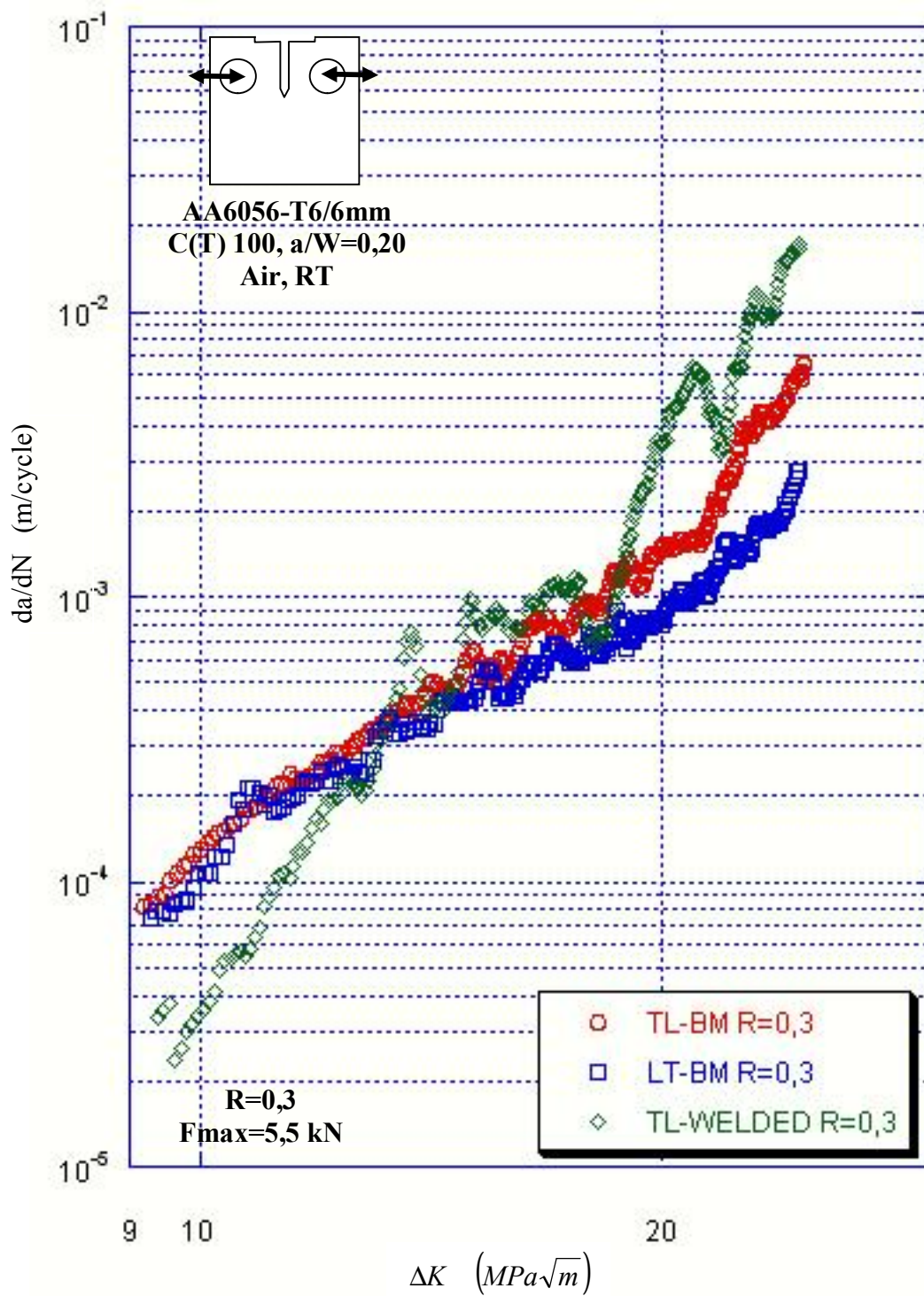


Figure 4.19 da/dN - ΔK curves of TL-BM, LT-BM and TL-welded specimens for $R=0,3$

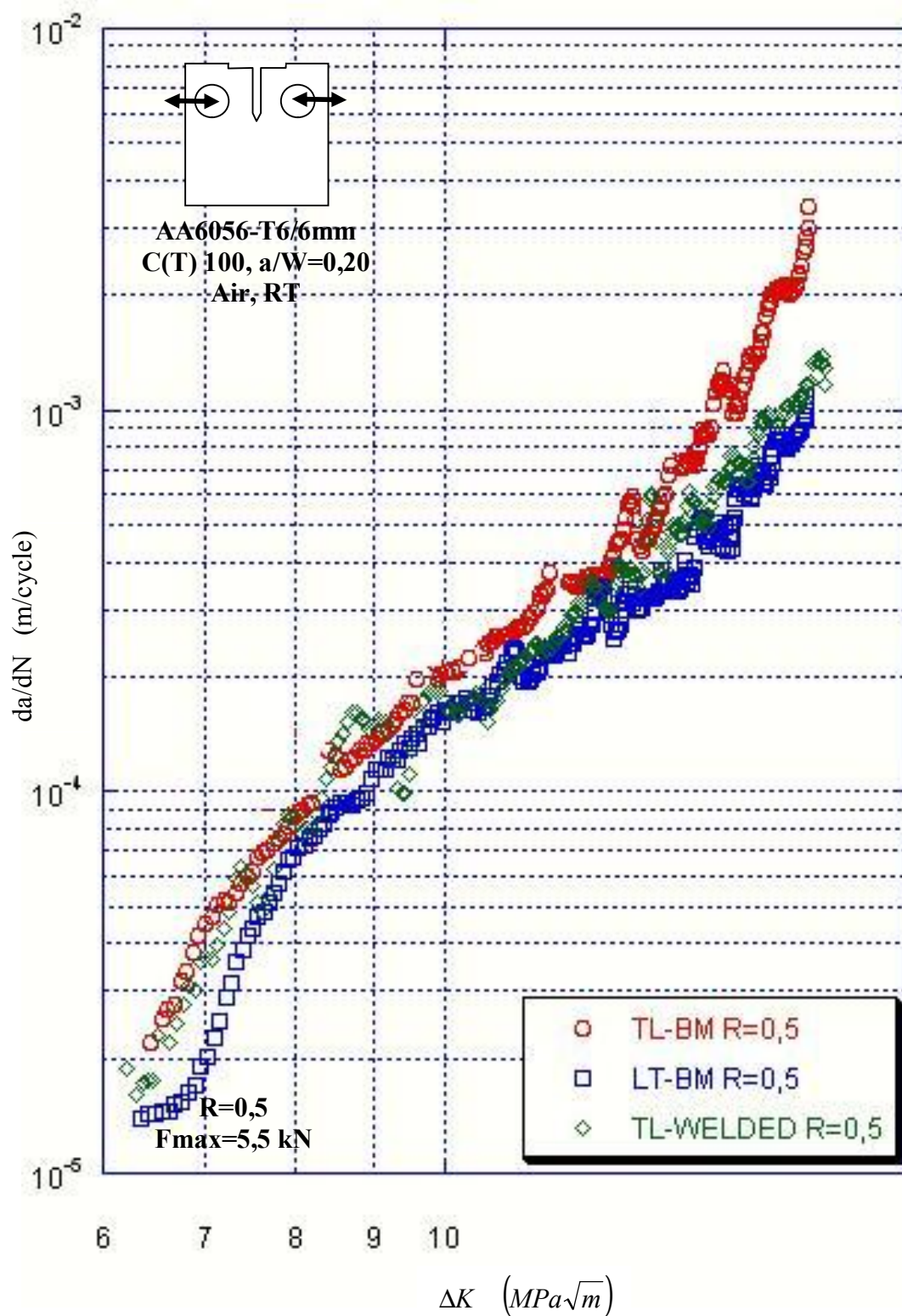


Figure 4.20 da/dN - ΔK curves of TL-BM, LT-BM and TL-welded specimens for $R=0,5$

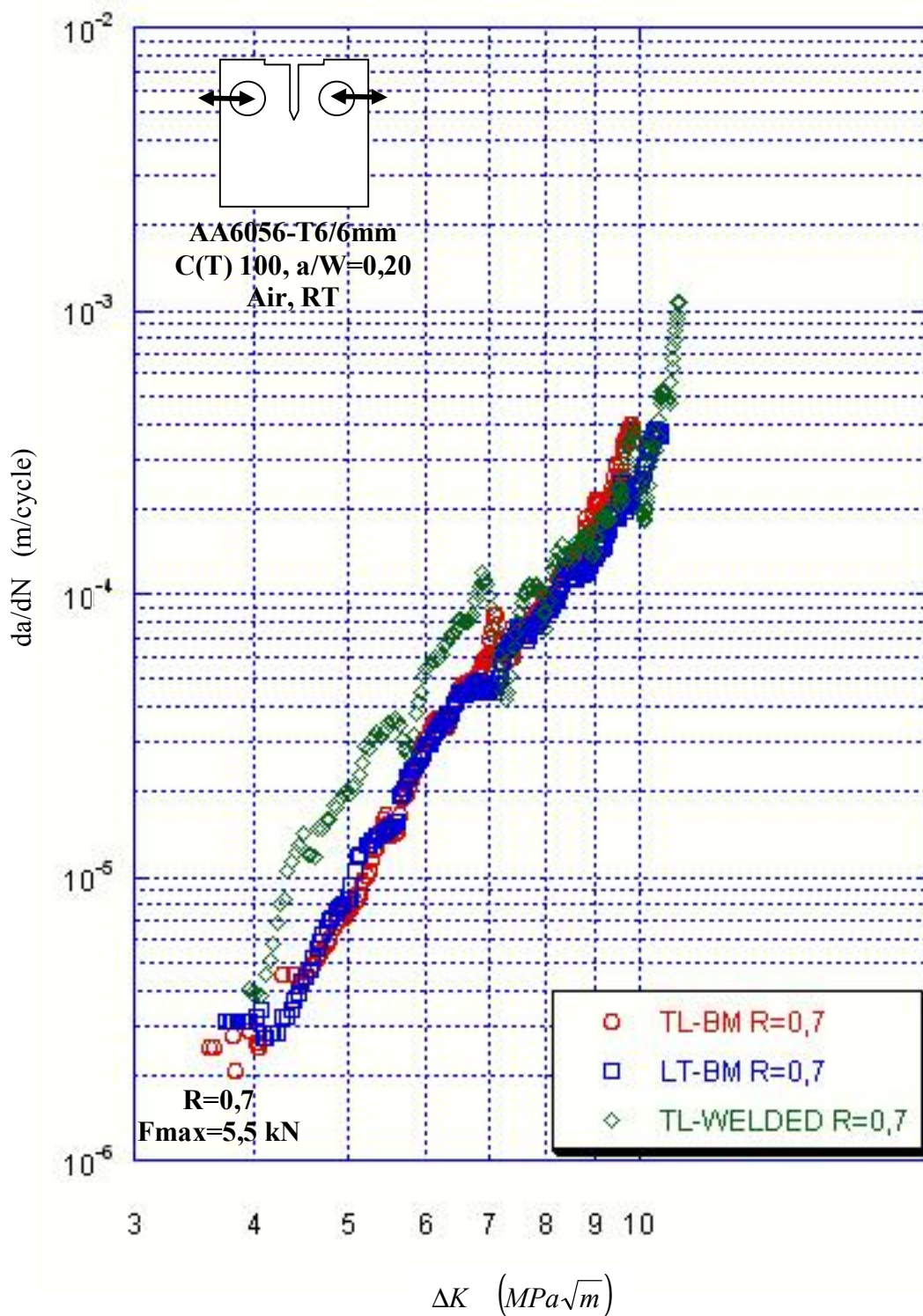


Figure 4.21 da/dN - ΔK curves of TL-BM, LT-BM and TL-welded specimens for $R=0,7$

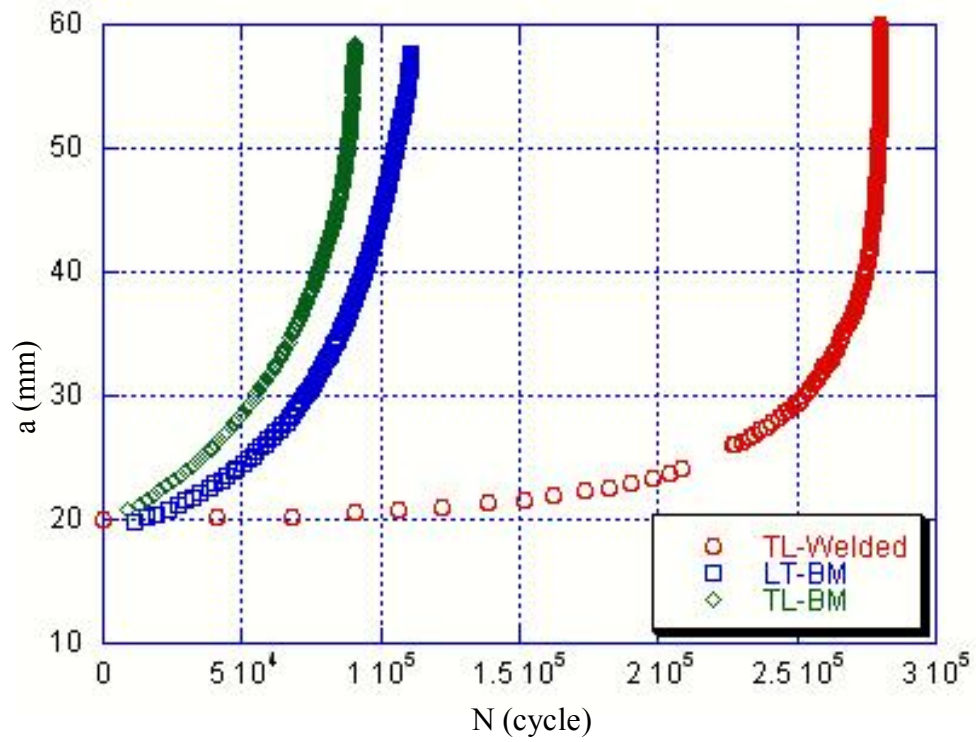


Figure 4.22 a-N curves of TL-BM, LT-BM and TL-welded specimens for $R=0,1$

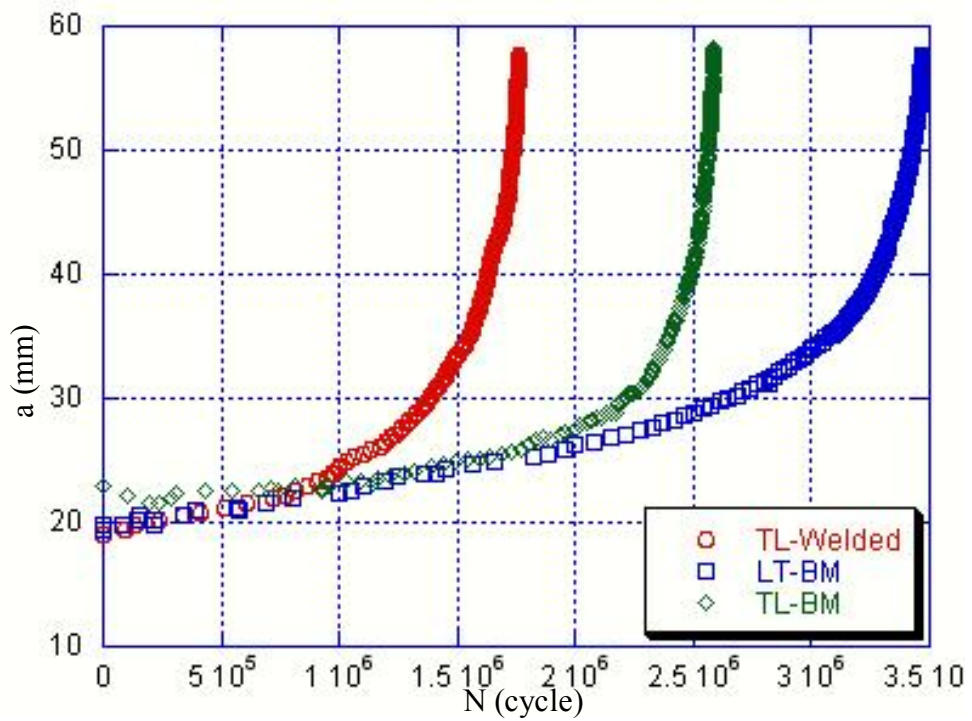


Figure 4.23 a-N curves of TL-BM, LT-BM and TL-welded specimens for $R=0,7$

While the crack propagation rates are comparatively parallel to each other in LT and TL-BM specimens, a higher crack propagation rate is detected in TL-welded specimens. When the crack propagation paths are examined, the crack propagation occurs as a result of void formation and their coalescence typical in ductile fracture mechanisms in BM specimens. The crack propagation mechanism in the welded region, on the other hand, is due to intergranular propagation along the grain boundaries (See figure 4.24).

All of the curves shown in Figures. 4.24, 4.25 and 4.26 are for $R=0.3$. It is seen from these Figures that the fatigue crack propagates always in the same direction without any deviations.

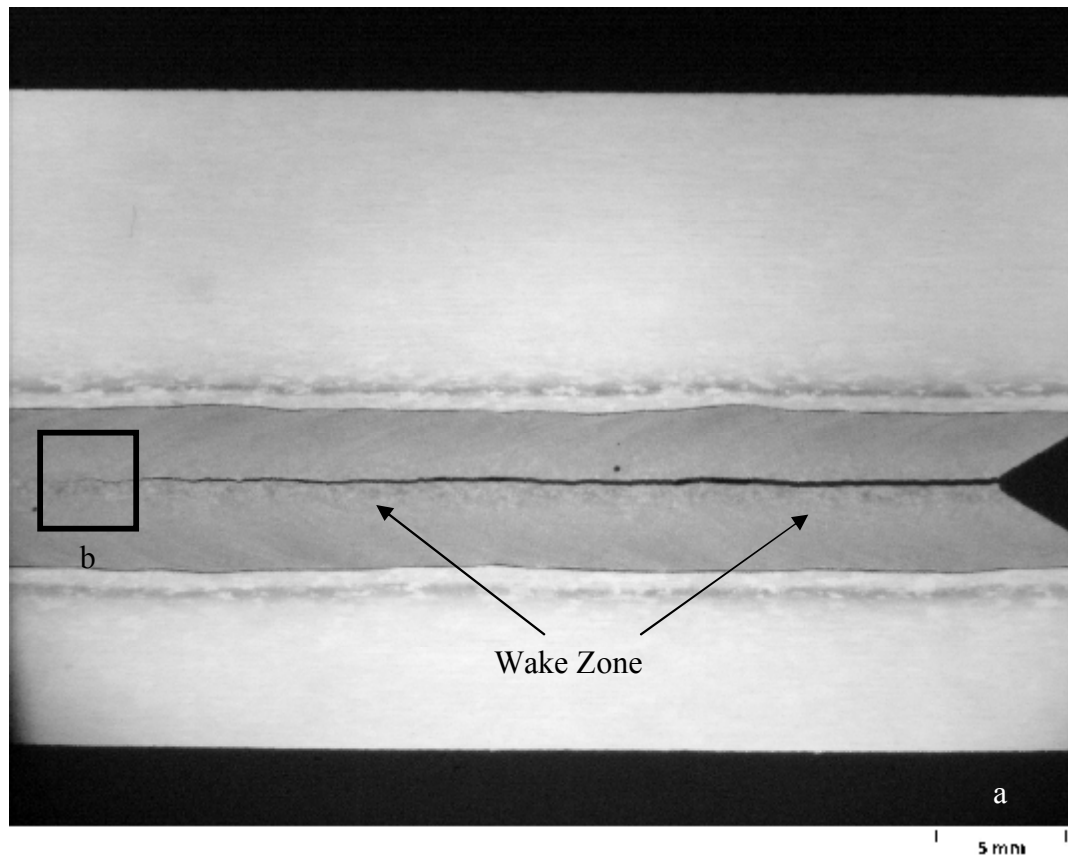


Figure 4.24 FCP path in TL-welded specimen

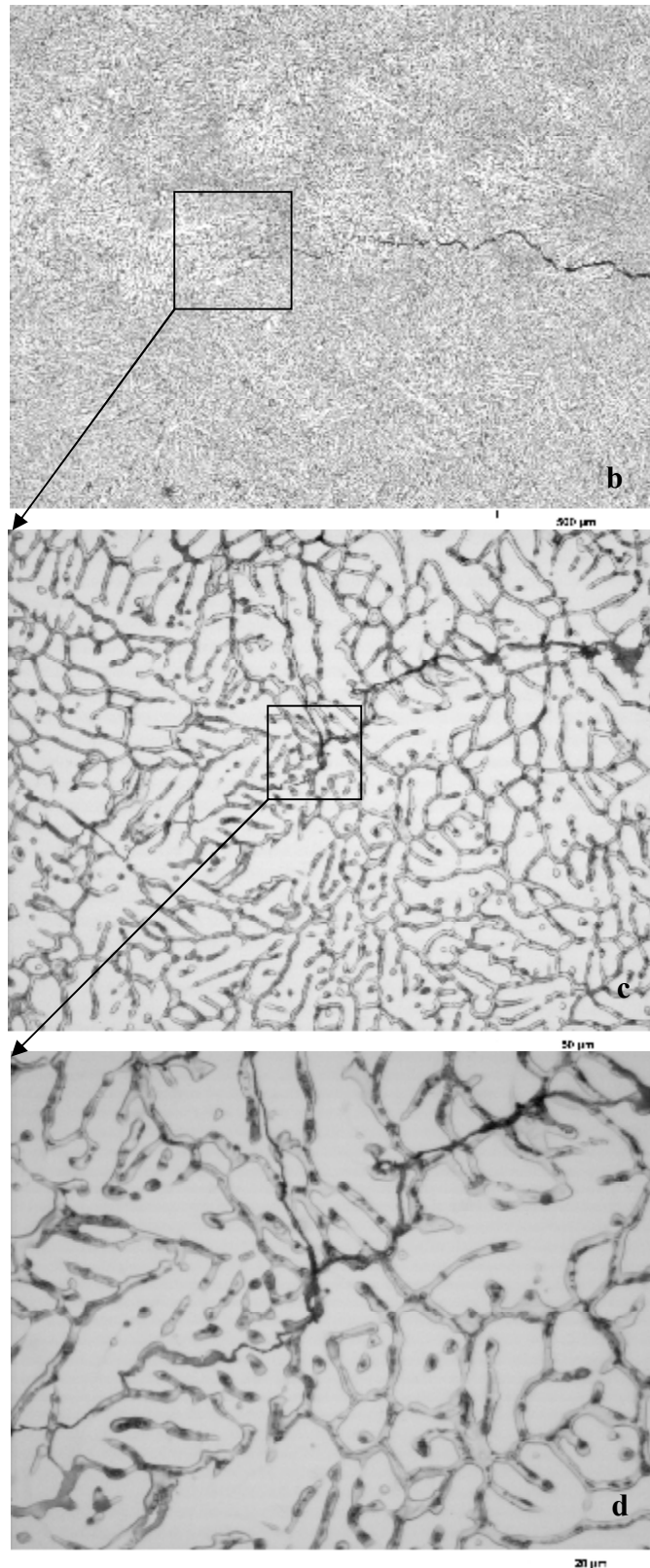


Figure 4.24 FCP path in TL-welded specimen [Continued].

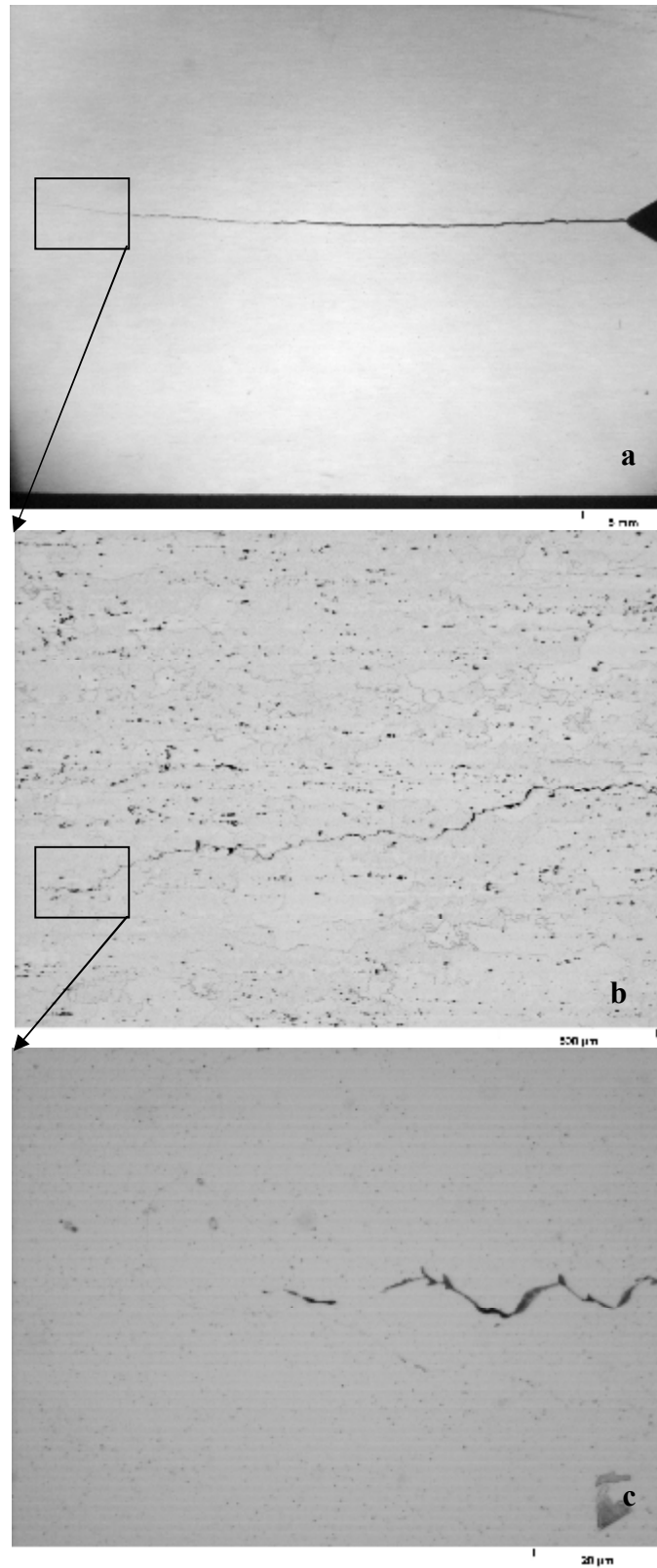


Figure 4.25 TL-BM FCP path

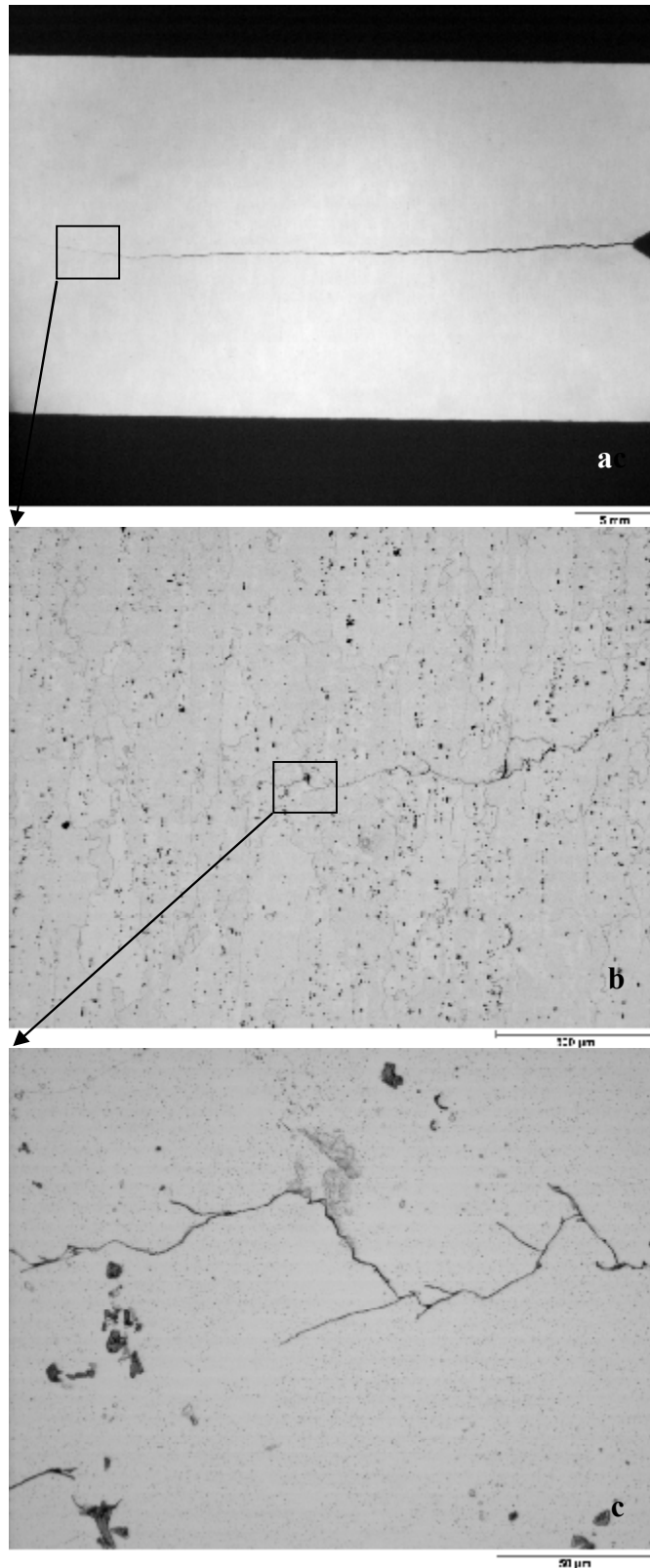


Figure 4.26 LT-BM FCP path

While the crack propagation is parallel in LT and TL-BM specimens as seen in Figs. 4.18 and 4.19, it is seen that the crack propagation rate is higher in TL-BM specimens than LT-BM specimens for $R=0.1$ after $\Delta K \approx 23 \text{ MPa}\sqrt{\text{m}}$. A river pattern was detected on the fracture surfaces of TL-BM specimens as seen in Figure 4.28 a. This of course causes rapid crack propagation.

The formation of river patterns was described by Anderson as follows: The multifaceted surface is typical of cleavage in a polycrystalline material; each facet corresponds to a single grain. The "river patterns" on each facet are also typical of cleavage fracture. These markings are so named because multiple lines converge to a single line, much like tributaries to a river.

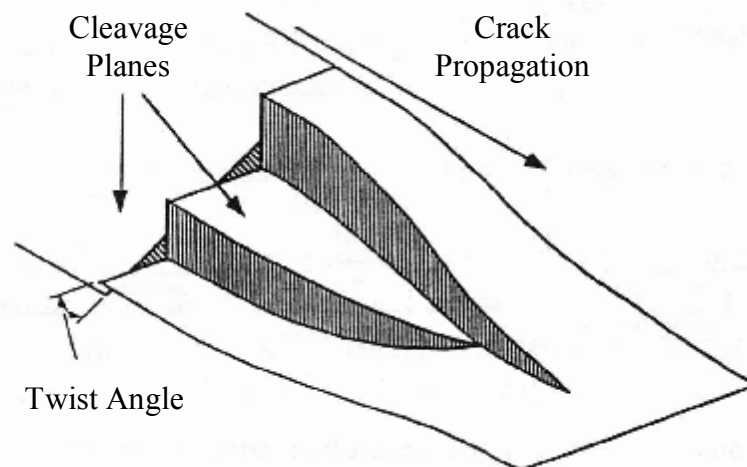


Figure 4.27 Formation of river patterns, as result of a cleavage crack crossing a twist boundary between grains. (Anderson, 1995)

Figure 4.27 illustrates how river patterns are formed. A propagating cleavage crack counters a grain boundary, where the nearest cleavage plane in the adjacent grain is oriented at a finite twist angle from the current cleavage plane. Initially, the crack accommodates the twist mismatch by forming on several parallel planes. As the multiple cracks propagate, they are joined by tearing between planes. Since this process consumes more energy than crack propagation on a single plane, there is a tendency for the multiple cracks to converge into a single crack. Thus, the direction of crack propagation can be inferred from river patterns (P.286).



Figure 4.28 (a) TL-BM and (b) LT-BM fracture surface ($R=0,1$)

What is of interest in Figure 4.17 and other fatigue diagrams is the instant variations in the fatigue curves of TL welds and decrease in crack propagation as a result of these variations. Porosity is thought to be the cause of this decrease.

It has been detected that porosity decreases crack propagation rate. In order to detect this effect, two specimens have been examined under a stress ratio of $R=0.5$. One of the specimens has comparatively less porosity at crack initiation. As a result, it was observed that the porosity causes decrease in crack propagation, Figure 4.29.

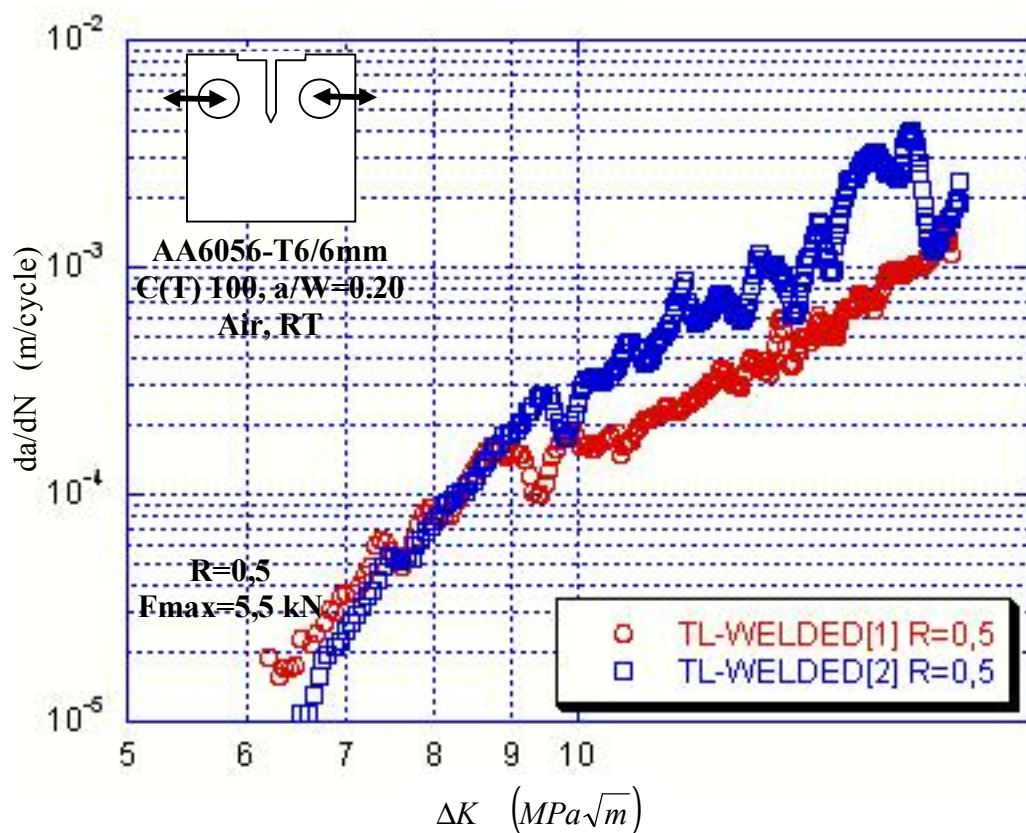


Figure 4.29 2-TL-welded specimens da/dN - ΔK curves ($R=0,5$)

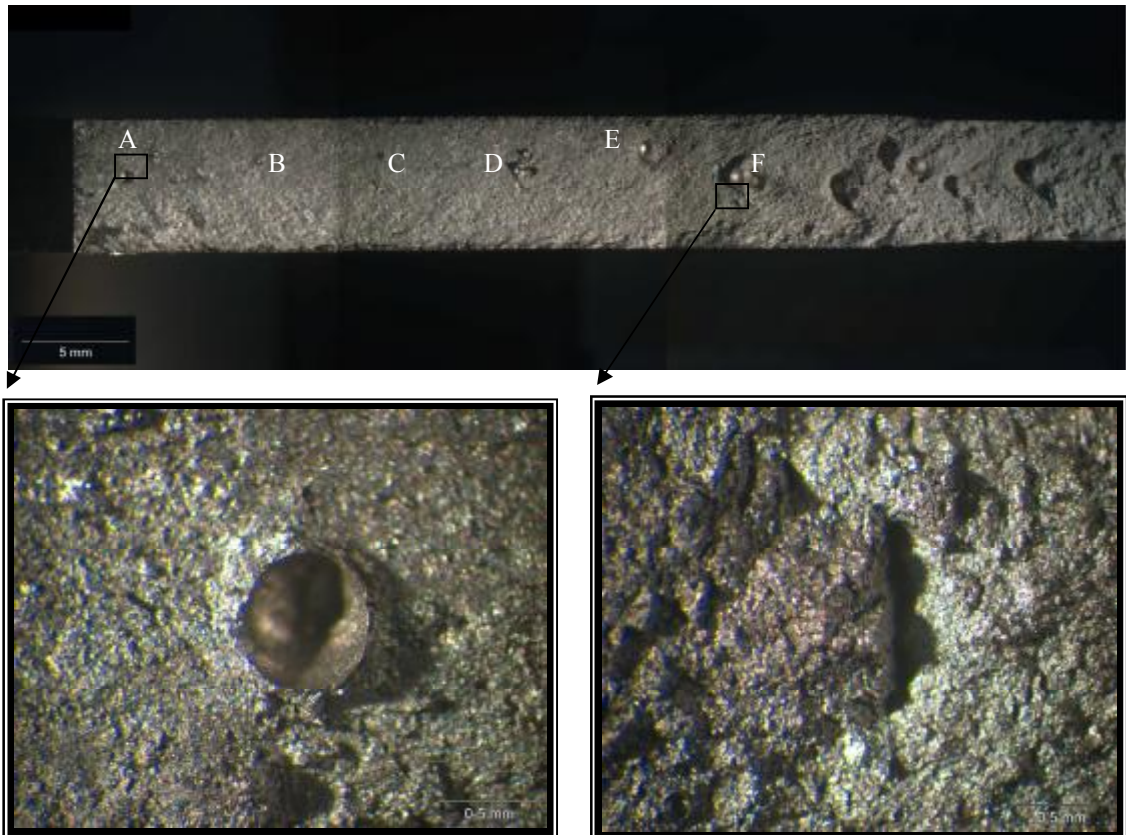
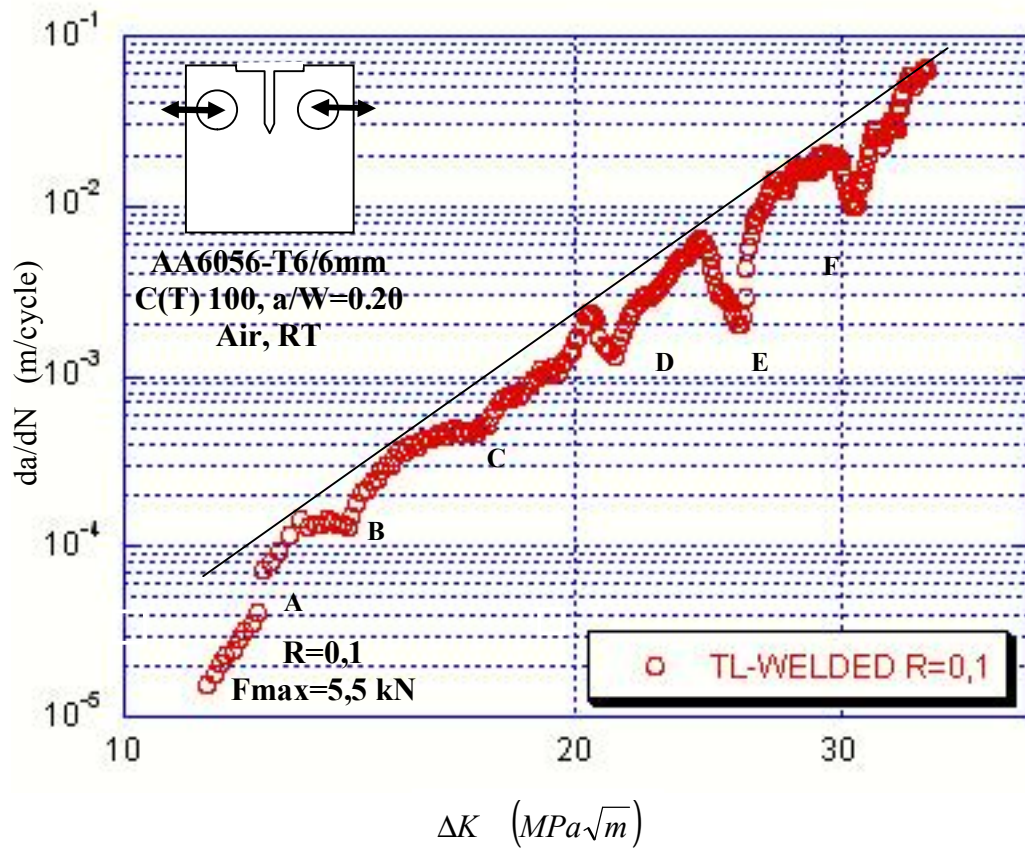


Figure 4.30 TL-welded specimens da/dN - ΔK curves and fracture surface ($R=0,1$)

In Figure 4.30, the details of porosity, effective in crack propagation and fracture surface, are given. Due to the crack blunting, the presence of porosity temporarily slows down crack propagation, after the formation of a sharp crack tip in a short time, and then the crack propagation rate increases again. The cracks detected in fracture surface and their dimensions are given in Table 4.4.

Table 4.4 Porosity effective da/dN for $R=0,1$

Porosity Name		Location (mm)	DK ($MPa\sqrt{m}$)	Size (mm)	da/dN
A	Start	22,150	No effect	0,670	No effect
	Finish	22,820			
B	Start	28,525	13,533	0,236	$1,556 \cdot 10^{-4}$
	Finish	28,761	14,098		$1,165 \cdot 10^{-4}$
C	Start	33,796	16,469	0,355	$5,314 \cdot 10^{-4}$
	Finish	34,151	17,220		$4,279 \cdot 10^{-4}$
D	Start	40,606	20,371	0,412	$2,422 \cdot 10^{-3}$
	Finish	41,018	21,308		$1,219 \cdot 10^{-3}$
E	Start	45,763	24,090	1,075	$6,424 \cdot 10^{-3}$
	Finish	46,838	25,824		$1,881 \cdot 10^{-3}$
F	Start	50,160	29,434	0,715	$2,040 \cdot 10^{-2}$
	Finish	50,875	30,663		$9,219 \cdot 10^{-3}$

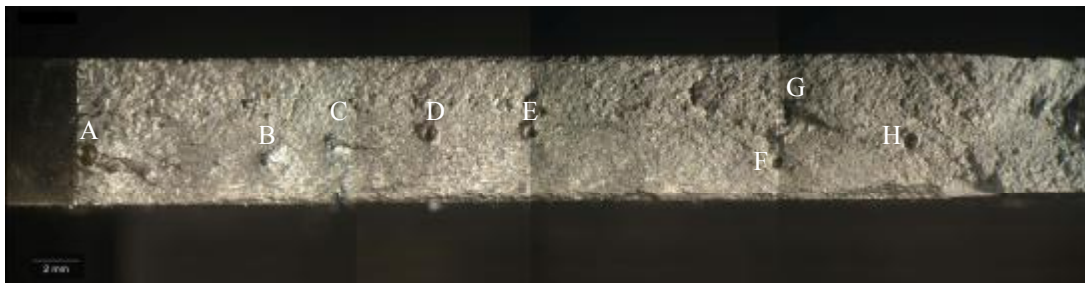
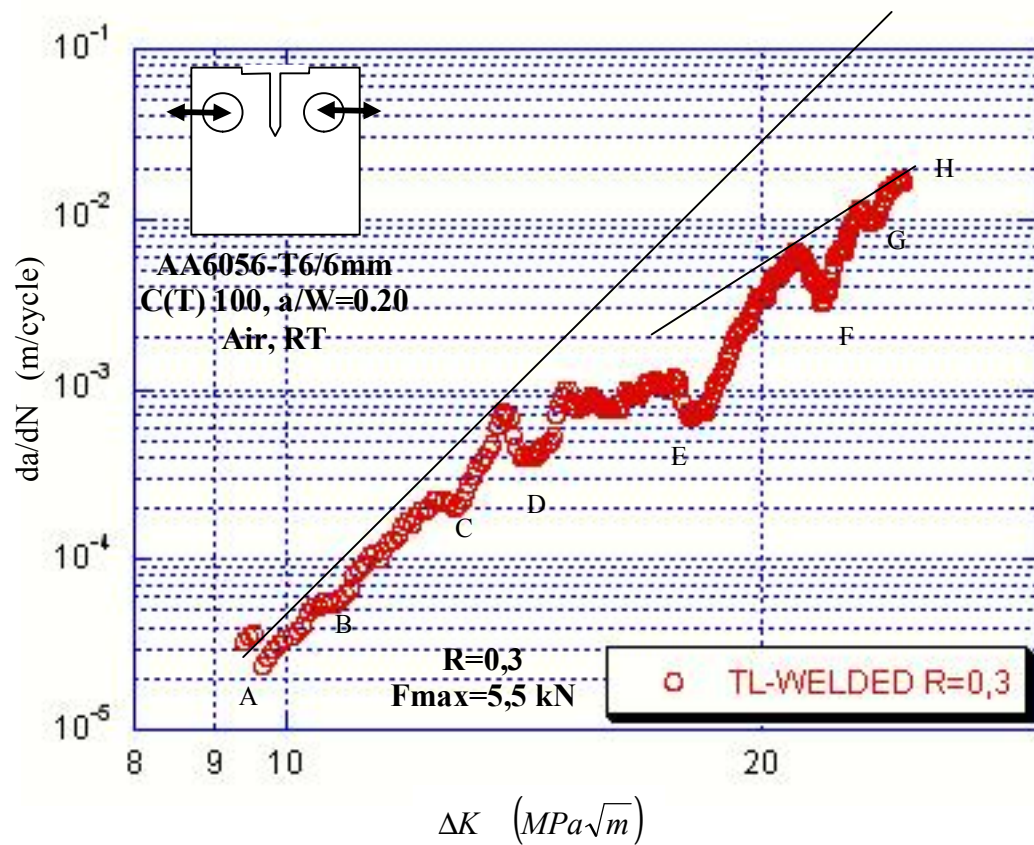


Figure 4.31 TL-welded specimens da/dN - ΔK curves and fracture surface ($R=0,3$)

As seen in Figure 4.31, when $R=0.3$, the presence of porosity causes crack blunting in contrast to $R=0.1$, in regions C and D the crack propagation proceeds intermittently. The cracks detected in fracture surface and their dimensions are given in Table 4.5.

Table 4.5 Porosity effective da/dN for R=0,3

Porosity Name		Location (mm)	DK ($MPa\sqrt{m}$)	Size (mm)	da/dN
A	Start	20,049	9,241	0,880	$3,293 \cdot 10^{-5}$
	Finish	20,929	9,497		$2,213 \cdot 10^{-5}$
B	Start	27,748	10,469	0,480	$5,869 \cdot 10^{-5}$
	Finish	28,228	10,717		$5,080 \cdot 10^{-5}$
C	Start	30,599	12,380	0,428	$2,401 \cdot 10^{-4}$
	Finish	31,027	12,723		$1,798 \cdot 10^{-4}$
D	Start	34,643	13,701	0,662	$7,907 \cdot 10^{-4}$
	Finish	35,305	14,301		$3,703 \cdot 10^{-4}$
E	Start	38,945	17,653	0,603	$1,264 \cdot 10^{-3}$
	Finish	39,548	18,141		$5,923 \cdot 10^{-4}$
F	Start	49,401	20,957	0,484	$6,660 \cdot 10^{-3}$
	Finish	49,885	22,047		$2,907 \cdot 10^{-3}$
G	Start	50,128	23,013	0,278	$1,230 \cdot 10^{-2}$
	Finish	50,406	23,557		$8,569 \cdot 10^{-3}$
H	Start	54,959	No effect	0,651	No effect
	Finish	55,610			

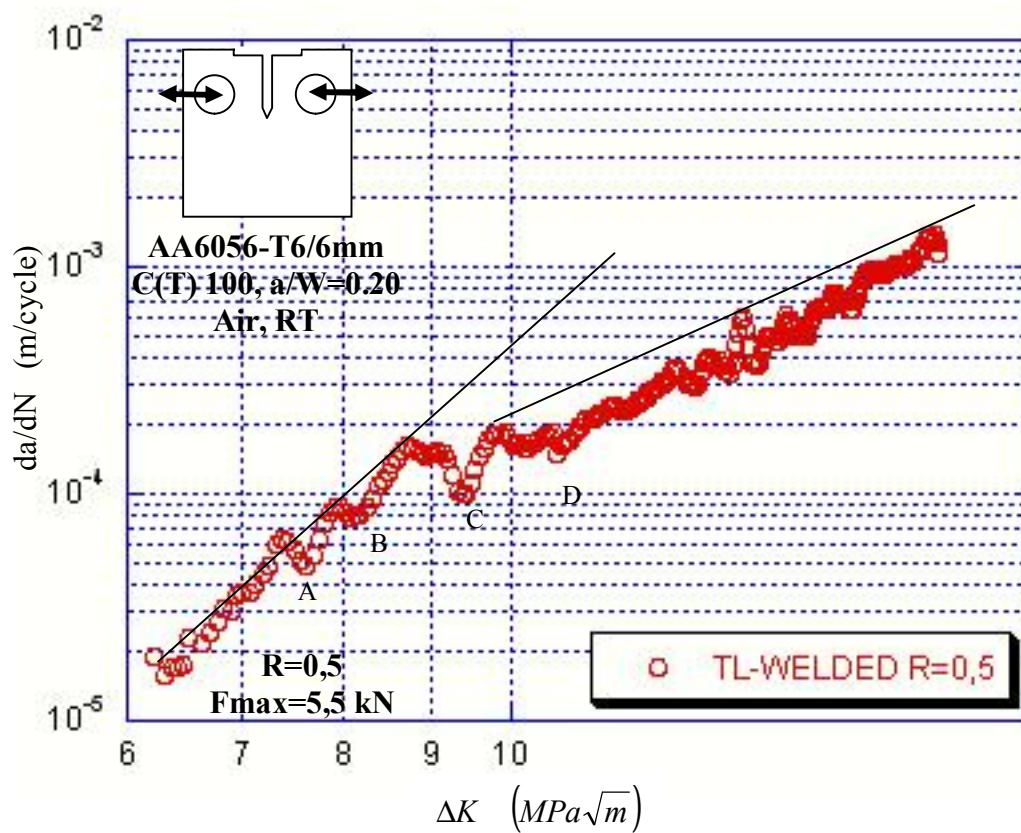


Figure 4.32 TL-welded specimens da/dN - ΔK curves and fracture surface ($R=0,5$)

It is seen in Figure 4.32 that, when $R=0.3$, the crack propagates very slowly. As a result of this, due to the effect of porosity, FCP slows down comparably and since the formation of a sharp crack tip requires some time, the crack propagation rate is slow even after the region of intense porosity. The cracks detected in fracture surface and their dimensions are given in Table 4.4. The concentration of pores in one region affects FCP even though the number of pores is not significant.

Table 4.6 Porosity effective da/dN for $R=0,5$

Porosity Name		Location (mm)	DK ($MPa\sqrt{m}$)	Size (mm)	da/dN
A	Start	29,312	7,398	0,778	$6,600 \cdot 10^{-5}$
	Finish	30,090	7,666		$4,436 \cdot 10^{-5}$
B	Start	31,669	7,943	1,033	$9,472 \cdot 10^{-5}$
	Finish	32,702	8,143		$6,843 \cdot 10^{-5}$
C	Start	38,778	9,091	0,705	$1,688 \cdot 10^{-4}$
	Finish	39,483	9,453		$9,136 \cdot 10^{-5}$
D	Start	40,294	10,113	0,596	$1,881 \cdot 10^{-4}$
	Finish	40,890	10,404		$1,359 \cdot 10^{-4}$

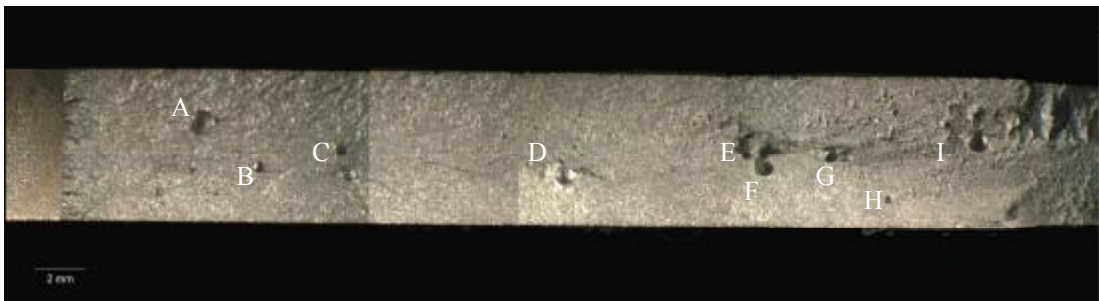
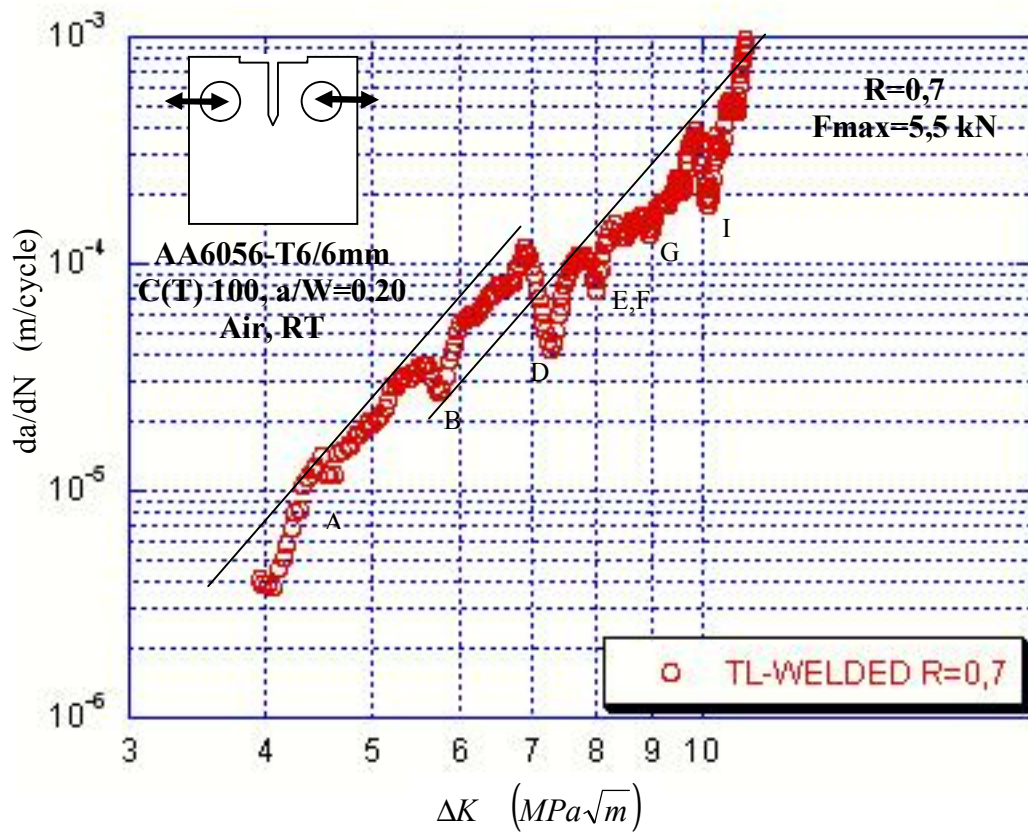


Figure 4.32 TL-welded specimens da/dN - ΔK curves and fracture surface ($R=0,7$)

In Figure 4.32, the effect of porosity distribution on FCP is shown. Similar to $R=0.5$, the presence of porosity causes FCP to slow down and eventually to stop.

In the overall results in Figure 4.17, it is seen that as R decreases the porosity slows down FCP more.

Table 4.7 Porosity effective da/dN for R=0,7

Porosity Name		Location (mm)	DK ($MPa\sqrt{m}$)	Size (mm)	da/dN
A	Start	24,985	4,364	1,011	$1,347 \cdot 10^{-5}$
	Finish	25,996	4,564		$1,055 \cdot 10^{-5}$
B	Start	27,544	5,521	0,478	$3,771 \cdot 10^{-5}$
	Finish	28,022	5,774		$2,511 \cdot 10^{-5}$
C	Start	30,789	No effect	0,388	No effect
	Finish	31,278			
D	Start	39,533	6,867	0,901	$1,145 \cdot 10^{-4}$
	Finish	40,434	7,303		$4,090 \cdot 10^{-5}$
E	Start	46,493	7,638	0,708	$1,114 \cdot 10^{-4}$
	Finish	47,201	7,388		$6,843 \cdot 10^{-5}$
F	Start	47,343	7,638	0,827	$1,114 \cdot 10^{-4}$
	Finish	48,176	7,388		$6,843 \cdot 10^{-5}$
G	Start	50,184	8,687	0,568	$1,719 \cdot 10^{-4}$
	Finish	50,752	8,984		$1,208 \cdot 10^{-4}$
H	Start	52,600	No effect	0,286	No effect
	Finish	52,886			
I	Start	55,793	9,880	0,946	$4,090 \cdot 10^{-4}$
	Finish	56,739	10,161		$1,719 \cdot 10^{-4}$

CHAPTER FIVE

CONCLUSIONS AND RECOMMENDATIONS

High quality joints were obtained with the CO₂ laser beam welding of 6056 aluminum alloys using AlSi12 filler wire.

Grain boundary liquation was detected in the FZ. It was also observed that, especially, grain boundary liquation became more pronounced as the amount of Si along the grain boundaries increased.

The formation of porosity was detected in the weld region due to the hydrogen entrapment.

Mechanical properties determined from macro- and micro-tensile specimens were found to be in accordance with each other.

As a result of the micro-hardness measurements and transverse tensile tests using micro-flat tensile specimens, a decrease in the strength of HAZ due to overaging was detected.

The mismatch ratio in 6056 aluminum, welded using AlSi12 filler wire, was 0.74. When this value is compared with the data in the literature (with those given for 6xxx series alloys with 6 mm thickness), it is seen that a successful result has been achieved.

A typical ductile crack propagation mechanism was observed in fatigue tests of LT and TL-BM specimens.

As the fatigue crack propagates in the TL-BM specimens, it constitutes river patterns in R=0.1 and 0.3 and to this end, crack propagation increases with the increase in ΔK .

It has been observed that the presence of porosity retards the crack propagation and slows down the crack propagation rate in relation with the value of R.

Intergranular crack propagation has been detected in the TL-welded specimens.

When joining two parts, if the part that may cause the crack initiation (like welding) is joined transverse to the rolling direction, fatigue crack propagation may proceed slower.

The results obtained from this study may, in the future, be used in NASGRO or AFGRO Finite Element Analysis software programs developed by NASA for modeling purposes. It may be advantageous utilizing these kinds of software for modeling specimens with various thicknesses, thus avoiding time consuming tests.

REFERENCES

- Allen, C.M. (2004) Laser welding of aluminium alloys – principles and applications. *Report, TWI, United Kingdom*
- Anderson, T. (2004a). *Trouble shooting for aluminum welding*. Retrieved March 1, 2004, from <http://www.alcotec.com>
- Anderson, T.L.(1995) Fatigue crack propagation. In *Fracture Mechanics* (2nd ed.) (513-555) London. CRC Press
- Anderson, T. (2004b). *Understanding the alloys of aluminum*. Retrieved May 11, 2004, from <http://www.alcotec.com>
- Anonymous (2004). *Undergraduate course, ASEN 4012*. Retrieved December 10, 2004, from <http://www.colorado.edu/ASEN/SrProjects/Projects/index.html>
- Anonymous. (2000). *Electron beam welding-equipment..* Retrieved November 20, 2004, from <http://www.twi.co.uk>
- Cardarelli, F. (1999). *Materials Handbook*. Springer Verlag, London.
- Costa, A.P., Quintino, L., Greitmann, M. (2003) Laser beam welding hard metals to steel. *Journal of materials processing technology, 141, 163-173*
- Çam, G., Dos Santos, J.F., Kocak, M. (1997) Laser and electron beam welding of Al-alloys: Literatur Review, *GKSS- Foschungszentrum*.
- Dif, R., Lequeu, Ph., Warner, T., Bès, B., Ribes, H., Lassince Ph. (2002a) Recent developments in aluminum sheet alloys used in aerospace. *Report, France*.

- Dif, R., Bechet, D., Warner, T., Ribes, H. (2002b) A corrosion resistant copper-rich 6xxx alloy for aerospace applications. *Report, France*.
- Dilthey, U., Wieschemann, A. (2000). Prospects by combining and coupling laser beam and arc welding processes. *Welding in the World*, 44 (3), 37-46.
- Doğan, B. (1995). Fatigue crack propagation. In *Engineering Fracture Mechanics* (1st ed.) (71-159) Hamburg: GKSS
- Dowden, J., Kapadia, P. (1996). The penetration depth in keyhole welding with pseudo-continuous Nd-YAG and CO lasers investigated mathematically. *Applied surface science* 106, 235-239.
- Fakatsu, K. (1997). Introduction to the Applied Laser Engineering Center (ALEC). *Nuclear Instruments and Methods in Physics Research B* 121, 7-9.
- Fuchs, H.O., Stephens, R.I. (1980). Fundamentals of lefm for application to fatigue crack growth and fracture and constant amplitude fatigue tests and data. In *Metal fatigue in engineering* (1st ed.) (37-105) USA: John Wiley & Sons, Inc.
- Greses, J., Hilton, P. (2004). *In the spotlight-plasma/plume effects in laser welding*. Retrieved January 4, 2005, from <http://www.co.uk/j32k/protected/band-2/b451a1.html>
- Haboudou, A., Peyre, P., Vannes, A.B., Peix, G. (2003). Reduction of porosity content generated during Nd:YAG laser welding of A356 and AA5083 aluminum alloys. *Materials science and engineering A363*, 40-52.
- Hilton, P. (2004a). *Carbon dioxide laser*. Retrieved November 17, 2005, from <http://www.co.uk/j32k/protected/band-3/kspah002.html>

- Hilton, P. (2004b). *Nd:YAG laser welding*. Retrieved September 9, 2004, from <http://www.co.uk/j32k/protected/band-3/kspah003.html>
- Horn, V., Kent, R. (1967). *Aluminum*. Volume I. Properties, Physical Metallurgy and Phase Diagrams. American Society for Metals.
- Ion, J.C. (2000). Laser beam welding of wrought aluminium alloys. *Science and Technology of Welding and Joining*, 5 (5), 265-276
- Jokinen, T., Kujanpää, V. (2003). High power Nd: YAG laser welding in manufacturing of vacuum vessel of fusion reactor. *Fusion Engineering and Design*, 69, 349-353.
- Kawano, S., Nakahigashi, S., Uesugi, K., Nakamura, H., Kono, W., Fukuya, K., et al. (1998). Weldability of helium-containing stainless using a YAG laser. *Journal of Nuclear Materials* 258-263, 2018-2022.
- Kocak, M., Çam, G., Riekehr, S., Torster, F., Dos Santos, J.F. (1998). Microtensile technique for weldments. *5th Annual report of IIW sub-comission X-F, 51st Annual Assembly, Hamburg*.
- Kusko, C.S., Dupont, J.N., Marder, A.R. (2004). Influence of stress ratio on fatigue crack propagation behavior of stainless steel welds. *Welding Research*, 59-64.
- Leigh, B.R., Poon, C., Ferguson, N. (2002). An evaluation of the physical properties of Nd:Yag laser welded high strength 6000 series aluminum alloys. *ICAS2002 Congress, Germany*
- Lenczowski, B. (2002). New Lightweight alloys for welded aircraft structure. *ICAS2002 Congress, Germany*

- Li, Y., Kuang, Y., Zhang, X. (2003). Polytetrafluoroethylene and metal structure convective-flow CO laser. *Optics & laser technology*, 35, 627-631.
- Li, Z., Fontana, G. (1998) Autogenous laser welding of stainless steel to free-cutting steel for the manufacture of hydraulic valves. *Journal of materials processing technology*, 74, 174-182
- Nightingale, K. (2004). *Reduced pressure electron beam welding*. Retrieved November 18, 2004, from <http://www.co.uk/j32k/protected/band-3/kskrn002.html>
- Marsico, T.A., Kossowsky, R. (1989) Laser beam welding of aluminum alloys plates 7039, 5083 and 2090. In *Laser material processing*, ICALEO'89, 69,(61-71). Orlando .
- Martukanitz, R.P. (1993). Selection and weldability of heat-treatable aluminum alloys. *ASM handbook, Welding, Brazing and Soldering* (528-536). USA
- Olson, D.L., Siewert, T.A., Liu, S., Edwards, G.R. (1993). Volume 6: Welding, brazing and soldering. In Henry, S.D., Hampson, S.E., Zorc, T.B., (Eds.). *ASM handbook* (254-269). USA
- Pakdil, M., Çam, G., Erim, S. (2004). 6xxx serisi alüminyum alaşımlarının kaynaklı kullanımı ve karşılaşılan problemler. *10. Denizli malzeme sempozyumu ve sergisi Bildiri kitabı* (s50). Türkiye
- Rhenalu, P. (2001) 6056-T6 /-T78 New Alloy – Sheets and thin plates a weldable corrosion resistant low density alloy. *Report, France*.
- Schellhorn, M., Eichhorn, A. (1996). Spectroscopic comparison of aluminum welding plasmas produced by high power CO and CO₂ lasers. *Optics & Laser Technology* 28(5), 405-407.

- Schijve, J. (1988). Fatigue crack closure: observation and technical significance. Newman, J.C.Jr., Elber, W., (Eds.). *Mecnanics of Fatigue Crack Closure* (5-34) Philadelphia: ASTM
- Schubert, E., Klassen, M., Zenner, I., Walz, C., Sepold, G. (2001) Light-weight structures produced by laser beam joining for future applications in automobile and aerospace industry. *Journal of material processing technology*, 115, 2-8.
- Sharp, M.L., Nordmark, G.E., Menzemer, C.C. (1996) Introduction. In *Fatigue design of aluminum components & structures* (1st ed.) (1-19). New York : McGraw- Hill
- Triantafyllidis, D., Schmidt, M.J.J., Li, L. (2003) Comparison of high power diode laser and Nd: YAG laser microwelding of k-type thermocouples. *Journal of Materials Processing Technology*, 138, 102-108.
- Vaidya, W.V., Kocak, M., Seib, E., Assler, H., Hackius, J. (2004). Mechanical behavior of laser beam and friction stir welded aluminium alloys for airframes. *International Conference on Technical Trends and Future Prospectives of Welding Technology for Transportation, Land, Sea, Air and Space, July 15-16, 2004, Osaka, Japan*